Search for New Physics Using Jets in Proton-Proton Collisions

Dissertation zur Erlangung des Grades

Doktor der Naturwissenschaften

Vorgelegt am
Fachbereich Physik, Mathematik und Informatik der
Johannes Gutenberg-Universität in Mainz

Oliver Chris Endner
geboren in Gross-Gerau

Mainz, den 14.12.2015

1. Berichterstatter:
2. Berichterstatter:
Datum der mündlichen Prüfung: 19.05.2016

KURZFASSUNG

In dieser Doktorarbeit wird die Suche nach Neuer Physik in Ereignissen mit zwei Jets vorgestellt. Diese Ereignisse wurden in Proton-Proton Kollisionen am Large Hadron Collider (LHC) am europäischen Kernforschungszentrum (CERN) in der Nähe des Genfer Sees in der Schweiz erzeugt. Diese Kollisionen wurden mit dem ATLAS Experiment, einem Vielzweckteilchendetektor, aufgenommen, der an einem vom vier Kollisionspunkten am LHC installiert ist.

Die Theorie zur Beschreibung von Teilchenphysikprozessen, das sogenannte Standard Modell, konnte bisher alle Messungen korrekt beschreiben. Trotzdem gibt das Standard Modell auf einige der grundlegenden Fragen keine Antwort. Wie kann man Schwerkraft innerhalb des Standard Modells beschreiben? Woraus besteht Dunkle Materie, welche bisher nicht direkt beobachtet wurde, aus der jedoch 26 % des Universums bestehen? Warum besitzen Neutrinos Masse?

Theorien die einige dieser Fragen beantworten, sagen die Existenz weiterer bisher nicht beobachteter Teilchen voraus. Eine Suche nach neuen Teilchen könnte die Zahl der Modelle eingrenzen, die die Natur beschreiben. Der LHC führt Kollisionen von Protonen bei hohen Energien durch, bei denen die Bausteine der Protonen, die farbgeladenen Partonen, miteinander wechselwirken. Der häufigste Endzustand bei solchen Kollisionen enthält zwei Partonen, also Quark-Quark, Quark-Gluon oder Gluon-Gluon Paare, sowie deren Antiteilchen. Wenn Partonen bei hohen Energien den Verbund im Proton verlassen, bildet sich ein Teilchenbündel, der als sogenannter *Jet* im Detektor sichtbar ist. Daher ist die Suche nach Neuer Physik in Ereignissen mit zwei Jets vielversprechend, um einen große Massenbereich zu untersuchen.

In dieser Arbeit wird die Suche nach Neuer Physik beschrieben, bei denen neue Teilchen als schmale Resonanzen im invarianten Massenspektrum zweier Jets auftauchen. Eine integrierte Luminosität von 20.3 fb^{-1} aufgenommen vom ATLAS Detektor bei einer Schwerpunktsenergie von 8 TeV wurde untersucht. Diese Energie war die höchste jemals in einem Labor erreichte Energie, zur Zeit der Messung. Das untersuchte Spektrum wurde aus Ereignisse kombiniert, die von zwölf unterschiedlichen Triggern aufgezeichnet wurden. Dies ermöglichte die Untersuchung im invarianten Massenbereich von 253 GeV bis 4.1 TeV. Die Untergrundabschätzung wurde durch Anpassung einer Funktion an das Datenspektrum gewonnen.

Der Vergleich zwischen Daten und Untergrund zeigt keine signifikanten Abweichungen. Daher wurden 95 % C.L Obergrenzen auf das Produkt von Wirkungsquerschnitt und Akzeptanz für sieben Modelle gesetzt. Die Produktion von schwarzen Löchern (QBH) konnte für Massen kleiner als 5.75 TeV ausgeschlossen werden, während angeregte Quarkzustände bis zu 3.90 TeV ausgeschlossen wurden. Zusätzlich wurden Ausschlussgrenzen für generische Signalformen gesetzt, die der Gaußfunktion und der Breit-Wigner-Formel folgen.

ABSTRACT

In this thesis a search for New Physics in events with two jets is presented. These events are produced in proton-proton collisions at the Large Hadron Collider (LHC) at the European Organization for Nuclear Research (CERN) close to the lake Geneva in Switzerland. These collisions have been recorded with the ATLAS experiment, a large multi-purpose particle detector that is placed at one of four points in the LHC where the proton beams are brought to collision.

The theory to describe the processes of particle physics, the Standard Model, was able to describe all measurements made so far. Apart from this amazing agreement, the Standard Model does not give an answer to some fundamental questions. How can gravity be described within the Standard Model? What is the mysterious form of matter that has not been seen, but 26 % of the universe are made of? Why are neutrinos massive?

Models answering some of these questions lead to the prediction of additional particles, that have not be seen before. A search for new particles might be able to narrow down the number of models, that could describe nature. The LHC collides protons at high energies, at which the underlying fundamental interaction is seen between partons and thus particles with a color charge. The simplest and most frequent final-state consists of two partons, namely a quark-quark, quark-gluon or gluon-gluon pair and their respective anti-particles. When partons at high energies leave the confined state of the proton a spray of particles is produced, which can be seen as so-called *jets* in the detector. Thus the search for New Physics in a final state with two jets is promising to probe the process with large cross-section and a very large mass range.

This thesis describes a search for new particles showing up as narrow resonances in the dijet mass spectrum. An integrated luminosity of $20.3\,\text{fb}^{-1}$ recorded at a center of mass energy of 8 TeV by the ATLAS detector has been used. This energy was the highest energy ever reached in a laboratory at this time. The data used in this analysis have been combined from events recorded by twelve different triggers. This extended the range of invariant masses probed from 253 GeV up to 4.1 TeV. The background estimation of the spectrum in this vast range was performed by fitting a functional form to data.

A comparison between data and estimated background showed no significant excesses. Hence 95 % C.L. upper limits on the cross section times acceptance have been set for seven different models. The production of a Quantum Black Hole could be excluded for dijet masses of up to 5.75 TeV, while an excited quark model was excluded up to 3.90 TeV. Additionally exclusion limits for signals of a Gaussian shape have been set. A more realistic model-independent limit was set for a Breit-Wigner shape convoluted with parton density effects, parton-shower effects and the detector resolution.

CONTENTS

1 INTRODUCTION

The question of what matter is made of accompanied humans since the beginning of time. The first modern ideas about the structure of matter are documented by Democritus about 2400 years ago. He envisioned matter as being built from a number of building blocks, that are characterized by shape and size. This picture was already close to nowadays molecules. More than two thousand years after Democritus atoms have been identified as the building blocks of matter, which can be classified as elements in a periodic system. This classification already hinted to a then unknown substructure. Within the last 120 years scientists found the constituents of atoms. In 1897 J.J. Thompson found the *electron*, which is the electrically negative charged particle that surrounds the positively charged nucleus. In 1919 Rutherford found first evidence for a positively charged particle which is part of the nucleus, the so-called *proton*. Chadwick finally found the second ingredient of the nucleus, an electrically neutral particle, called *neutron*.

In the course of forty years a large variety of particles have been discovered in experiments with accelerators. In 1974 a first description of these particles as a composition of elementary particles was presented. The Standard Model (SM) of particle physics was able to describe all the particles found so far by introducing six quarks and six leptons, with their corresponding anti-particles. Additionally the SM could explain the interactions between these particles via twelve bosons and the Higgs boson giving mass to particles. All elementary particles predicted by the SM have been found since, concluding with the Higgs boson whose discovery was announced on 4th of July 2012 by the ATLAS and CMS collaborations at the Large Hadron Collider (LHC) which is situated at the European Organization for Nuclear Research (CERN) close to Geneva.

Despite being extremely successful in describing nature, there are some shortcomings of the SM. There a several phenomena that cannot be explained by the SM, such as gravity, the asymmetry between matter and anti-matter, dark matter and dark energy. The so far also very successful theory to describe gravity, general relativity, could not be included in the SM. Additionally the theory which describes the beginning of the universe and the *Big Bang*, assumes that matter and anti-matter have been produced in equal amounts. Observations have shown, that now the amount of anti-matter in the universe is much smaller than the amount of matter. This cannot be explained by the SM. From indirect measurements it is also apparent, that only 6.8 % of the matter and energy in the universe are made of SM particles. 26.1 % of matter in the universe is of a different type. The so-called *Dark Matter* interacts only gravitationally or weakly but not electromagnetically or strongly. The remaining fraction is the mysterious *Dark Energy*, which is completely unexplained by now.

Apart from these phenomena that are not included in the SM, there are also intrinsic problems and questions that suggest that this model is only a low-energy approximation of a larger, more fundamental theory.

A new theory as an extension to the SM could lead to new particles hinting to a compositeness of the elementary particles. Those phenomena could be unraveled by searching for resonance-like structures in an invariant mass distributions. The processes with the largest cross-section at a hadron-hadron collider are the production of quark-quark, quark-gluon and gluon-gluon pairs. When leaving the confinement of a nucleon, these partons undergo a process of hadronization. Thus a parton develops a spray of particles, those are observed in the detector as so-called *jets*. The invariant mass distribution of two jets (dijet) is thus the ideal study subject to cover a large range of invariant masses, by exploiting the largest production rates.

In this thesis resonance-like features are searched in the invariant mass spectrum of two jets. The data recorded in 2012 by the ATLAS detector at the LHC in proton-proton collisions at a center of mass energy of $\sqrt{s} = 8\,\text{TeV}$ with an integrated luminosity of $\mathcal{L} = 20.3\,\text{fb}^{-1}$ is used. The background shape is estimated by fitting a functional form to the invariant dijet mass spectrum, while excluding significant deviations. This background estimation is then compared to the data spectrum. The so-called *BumpHunter* algorithm searches excesses from resonances by comparing background and data. If no significant excesses are found, limits on the cross-section times acceptance for several New Physics models can be set. Comparing this cross-section limit with the theoretical production cross-section of resonances from New Physics models gives a limit on the mass of these New Phenomena.

Apart from model specific limits, also limits using a more generic signal shape are presented. A signal with a Gaussian shape is examined for different widths. While also a signal based on a Breit-Wigner distribution, with Parton Density Function effects included, as well as parton shower effects taken into account, is used for the limit calculation.

Additionally the found limits are presented in the mass versus coupling strength plane. This makes it possible to easily compare results from experiments at different center of mass energy and different type of colliding particles.

The theoretical foundations of elementary particle physics are discussed in Chapter 2. The accelerator and the detector used to record data for this thesis are briefly summarized in Chapter 3. An overview of how the objects used in this work are obtained and calibrated is shown in Chapter 4. The search for New Physics in the invariant dijet mass spectrum and the calculation of exclusion limits for signals of several models, as well as generic model-independent signals, are discussed in detail in Chapter 5. Finally an overview of this work and an outlook on future searches is shown in Chapter 6.

2 THEORY

In this chapter the theoretical foundations of high energy physics are briefly discussed. In Sec. 2.1 the Standard Model of particle physics is introduced, which represents the best knowledge to date. The need for extensions of this model and some selected options are discussed in Sec. 2.2. The general nature of proton-proton collisions is briefly shown in Sec. 2.3. The simulation of these collisions with Monte Carlo methods is detailed in Sec. 2.4.

THE STANDARD MODEL OF PARTICLE PHYSICS

The Standard Model (SM) of particle physics is a model which concludes the experimental and theoretical work spanning hundred of years. The first questions date back to the time when humanity asked questions about what the matter around us is made of and culminated in the golden century of particle physics in the 19th century. The SM is the most successful model in describing particle physics to date and did withstand hundreds of precise measurements. Nevertheless, this theory cannot be the final theory, as several phenomena are not explained, leading to work on theories beyond the Standard Model (BSM).

This section starts with a short historical overview of particle physics in Sec. 2.1.1. In Sec. 2.1.2 the full classification of particles in the SM is shown and some group theory considerations are made in Sec. 2.1.3.

History of Particle Physics

Since the beginning of time humans are searching for an answer to the big questions. Among these the question about what the matter surrounding us is made of and if there is a common constituent of things as different as fluid water or hard iron. One of the first theoretical considerations that was close to the modern particle physics was made by Democritus around 400 B.C., who coined the idea of *atoms*. In his theory every object was made of atoms which are only differing by shape and size. Hence this idea is closely related to the modern picture of molecules.

Many hundred years later in the 17th century scientists have been studying light and its nature. On one hand physicists as Newton thought of light as a particle [1], while on the other hand scientists as Huygens preferred to think of light as a wave [2]. Experiments in 1896 by Becquerel

found the photoelectric effect [3] which got explained by Einstein in 1905 [4]. This effect showed that metal emits charged particles when irradiated by light, while the maximum energy of those particles is independent of the intensity of light. This supported the theory of light as particles with a quantized energy. Contrary to the particle theory, the wave nature of particles was shown in double slit experiments, hence a duality of wave and particle nature of light was concluded.

By the 1860s, matter was identified as built from elements, a large number of elements was known which was classified by their chemical properties. In 1869 Mendeleev proposed a classification in a periodic system [5] which predicted successfully unknown elements and their properties.

Around the 1890s, many scientists imagined atoms to be built from smaller units that should be of the size of the smallest atoms. In 1897 J.J. Thomson discovered an electrically charged particle, the electron, in cathode rays [6]. This discovery lead to an atomic model, where an atom consists of a positively charged sphere, in which electrons are embedded.

In 1909 Rutherford discovered in experiments with α-particles scattering off gold-foil that α-particles scattered under larger angles are observed [7]. This lead to his interpretation of the atomic model in 1911 [8], which states that atoms consist of a dense positively charged nucleus and electrons around it.

In 1913, Niels Bohr described the hydrogen atom in a theory [9–11] using the two then known particles, the positively charged nucleus and the electron. He also calculated the radius of the hydrogen to be of the order of 1×10^{-10} m, which sets the scale for every further experiment in this field. The nature of the nucleus was uncovered when Rutherford found first evidence for the proton in 1919 and finally Chadwick discovered the neutron in 1932 [12].

In parallel Dirac postulated the existence of anti-particles in 1931, which are a direct consequence of the Dirac equation. Already one year later in 1932, Anderson discovered the positron [13] which is the anti-particle of the electron.

More than 15 years later in 1947 the first pions have been seen in cosmic rays [14], and only one year later in 1948 the first pions have been produced in the synchro-cyclotron in Berkeley [15].

In the following years a large number of particles have been discovered in improved accelerators or cosmic ray observations. This so-called *particle zoo* was finally classified in a model with only 19 free parameters[1] that was shown for the first time summarized in a single presentation by Iliopoulos [16] in July 1974 and later called the Standard Model. The main theoretical concepts for this model have been the introduction of Quantum Electrodynamics (QED) by Dirac in 1927, the quark model introduced by Gell-Mann [17] and Zweig in 1964 [18]. As well as the color property which was introduced in 1965 by Greenberg [19], Han and Nambu [20]. In 1967 the theories of the electro-magnetic interaction and the weak interaction have been unified by Glashow, Salam and Weinberg [21]. Finally in 1973 Fritzsch and Gell-Mann proposed a theory that describes the color charged particles in a theory inspired by QED, which was called the *Quantum Chromodynamics* (QCD) [22].

1 By then neutrinos where considered massless. With massive neutrinos there are 28 free parameters.

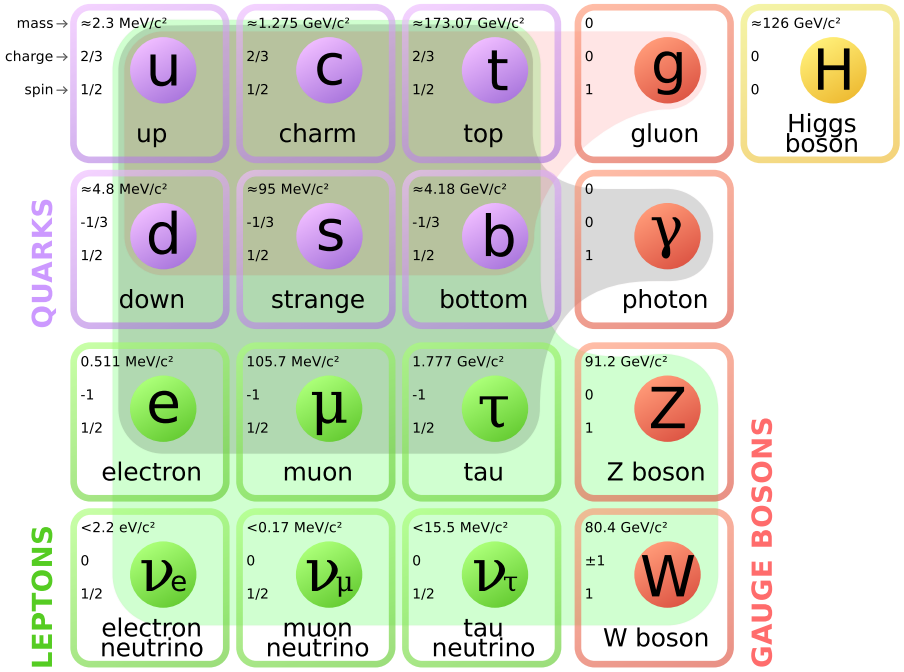

Figure 2.1: Overview of particles and properties in the SM [25].

All particles contained in the SM have been found since, concluding with the Higgs boson whose discovery was announced on 4th of July 2012 by the ATLAS [23] and CMS [24] collaborations at CERN.

Classification of Particles

The particles in the SM can be classified according to their spin, charge and mass as shown in Fig. 2.1. Particles with an integer spin are called *bosons*, while particles with half-integral spin are called *fermions*. The fermions are divided in leptons and quarks, which are each divided in three families. The 2nd and 3rd families are essentially heavier copies of the first family.

There are three up-type quarks with an electric charge of $2/3$ of the absolute electron charge and three down-type quarks with $-1/3$ charge. Each of these quarks has an anti-particle, and each of the quarks exists with three different color charges, hence there are 12 different quarks[2]. The mass of the quarks ranges from 2.3 MeV[3] for the up-quark to 173.07 GeV for the top-quark.

The leptons include three charged particles called electron, muon and tau, and three neutral particles associated to these, called neutrinos. The charged leptons have a mass from 511 keV for

2 From here on the quarks and antiquarks are not handled separately and are called quarks for simplicity
3 Using high energy physics convention of $c = 1$.

electrons up to 1.78 GeV for τ-leptons. The masses of the neutrinos have not been measured, but 95% C.L. upper limits are found for the electron neutrino mass of $m_{\nu_e} < 2.3\,\text{eV}$ [26].

The bosons can be classified by their. The spin 1 particles are the gauge bosons that are acting as force carriers. While the spin 0 boson, the Higgs boson, gives mass to the former bosons, except the gluon and photon, and couples to all massive particles including itself.

Quantum Field Theory

The Standard Model is a non-abelian gauge field theory which is based on the product of three groups $SU(3)_C \otimes SU(2)_L \otimes U(1)_Y$. The groups $SU(2)_L \otimes U(1)_Y$ describe the electro-weak sector, which is the unification of the electro-magnetic interactions and the weak forces. The group $SU(3)_C$ contains the QCD and the interactions related to the color charges.

A field theory describes the interaction between fermions and bosons by constructing a Lagrangian density $\mathcal{L}$ and introducing fermion fields Ψ and boson fields A^μ to describe the particles and forces. For a fermion of mass m the Lagrangian density, without a potential is:

$$\mathcal{L} = \bar{\Psi}(i\gamma^\mu \partial_\mu - m)\Psi \tag{2.1}$$

With Dirac's γ-matrices γ^μ and the adjunct spinor $\bar{\Psi} = \Psi^\dagger \gamma^0$.

Interactions with an external field can be added to the Lagrangian by adding a boson field A^μ. A priori the new Lagrangian obtained is not invariant under gauge transformations of the type:

$$A_\mu(x) \to A'_\mu(x) = A_\mu(x) + \partial_\mu \Lambda(x) \tag{2.2}$$

Where $\Lambda(x)$ is an arbitrary field.

A Lagrangian which is unchanged under a gauge transformation is called *gauge invariant*. To restore the invariance the fermion fields and the derivative ∂_μ are adapted simultaneously.

Each generator of a symmetry groups under which the Lagrangian is invariant, yields an additional boson, as outlined below. For a detailed description of quantum field theory see [27].

Electro-Weak Unification

The electro-magnetic and weak forces can be unified and described by the product group $SU(2)_L \otimes U(1)_Y$, with the weak hyper charge $Y = Q - I_3$ and weak isospin I. Here Q is the electric charge and I_3 is the third component of the weak isospin.

The theory includes a massless isospin triplet field $\mathbf{W}_\mu = (W_\mu^{(1)}, W_\mu^{(2)}, W_\mu^{(3)})$ from $SU(2)_L$ and a massless isospin singlet B_μ for $U(1)_Y$. The physically observed states $W_\mu^+, W_\mu^-, Z_\mu^0$ and A_μ are

linear combinations of the former mentioned massless fields introducing the weak mixing angle θ_W.

The Lagrangian describing the interaction in the electro-weak unified theory is:

$$\mathcal{L}_{\text{int}} = g \cdot \mathbf{J}^{\mu} \cdot \mathbf{W}_{\mu} + g' \cdot J^{\mu}_{Y} \cdot B_{\mu} \tag{2.3}$$

With g and g' denoting the coupling constants to $\mathbf{W}_{\mu}$ and B_{μ}. Here the currents for the weak isospin $\mathbf{J}^{\mu}$ and the weak hypercharge $J^{Y}_{\mu} = J^{\text{e.m.}}_{\mu} - J^{(3)}_{\mu}$ are used. Rewriting the Lagrangian with the physical fields and the relation of the couplings $g/g' = \tan(\theta_W)$ to the weak mixing angle θ_W gives:

$$\mathcal{L}_{\text{int}} = \frac{g}{\sqrt{2}} \left(J^{-}_{\mu} W^{\mu +} + J^{+}_{\mu} W^{\mu -} \right) + \frac{g}{\cos\theta_W} \left(J^{(3)}_{\mu} - \sin^2\theta_W \cdot J^{\text{e.m.}}_{\mu} \right) Z^{\mu} + g \cdot \sin\theta_W \cdot J^{\text{e.m.}}_{\mu} A^{\mu} \tag{2.4}$$

The first term describes the interaction via the weak charged current, while the second term describes the weak neutral current. The third term represents the interaction via the electromagnetic neutral current. Thus $W^{\mu +}$ and $W^{\mu -}$ are the charged gauge bosons, while Z^{μ} is the neutral gauge boson of the weak interaction. Similarly A^{μ} is the neutral gauge boson of the electromagnetic interaction known as the photon.

It was experimentally observed that charged weak gauge bosons only couple to left handed quarks and leptons. This nature is represented in the definitions of the currents as:

$$J^{+}_{\mu} = \bar{\nu} \gamma_{\mu} \frac{(1+\gamma_5)}{2} l \tag{2.5}$$

$$J^{-}_{\mu} = \bar{l} \gamma_{\mu} \frac{(1+\gamma_5)}{2} \nu \tag{2.6}$$

$$J^{(3)}_{\mu} = \bar{\Psi} \gamma_{\mu} \frac{(1+\gamma_5)}{2} I_3 \Psi \tag{2.7}$$

With the projection to left handed-chirality as $(1+\gamma_5)/2$ and the third component of the isospin I_3. Here the wave function $\Psi = \binom{\nu}{l}$ is used, l and ν are a lepton and the neutrino with the same flavor.

The Higgs Boson

Three of the gauge bosons introduced in the former section are experimentally found to be massive. To implement the mass in the Lagrangian a mass term of the type $-m^2/2 A^{\mu} A_{\mu}$ could be added. As this term would violate gauge invariance, a different approach is taken here. If

one defines the covariate derivative as $D^\mu = \partial^\mu - ig\frac{1}{2}\boldsymbol{\tau}\mathbf{W}_\mu - ig'\frac{1}{2}Y \cdot B_\mu$, where $\boldsymbol{\tau}$ are the Pauli matrices, then the Lagrangian for a complex field ϕ can be written as:

$$\mathcal{L}_{\text{Higgs}} = [iD^\mu\phi]^\dagger\,[iD_\mu\phi] - \mu^2\phi^\dagger\phi - \lambda\left[\phi^\dagger\phi\right]^2 \tag{2.8}$$

Different realizations of the complex field are possible. The ground state ϕ^0 of this field can be transformed via gauge transformations, such that one realization of the ground state is

$$\phi^0 = \frac{1}{\sqrt{2}}\begin{pmatrix}0\\ v\end{pmatrix} \tag{2.9}$$

with the vacuum expectation value $v^2 = -\mu^2/\lambda$. The non-zero vacuum expectation value shows that the ground-state breaks the symmetry spontaneously for this potential. This effect is well-known from superconductivity (see [28]). Expanding the non-zero component around the ground state gives an additional potential $h(x)$, which is called the Higgs field. Inserting the linear combination for the physical boson fields in the relevant part of the first term of Eqn. 2.8:

$$\left|\left(-ig\frac{1}{2}\boldsymbol{\tau}\mathbf{W}_\mu - ig'\frac{1}{2}Y \cdot B_\mu\right)\phi\right|^2 = M_W^2 W_\mu^+ W^{-\mu} + \frac{1}{2}M_Z^2 Z_\mu Z^\mu \tag{2.10}$$

Here the masses of the W boson is $M_W = 1/2vg$ and the mass of the Z boson is $M_Z = 1/2v\sqrt{g^2+g'^2}$. Thus due to the spontaneous symmetry breaking the vacuum expectation value is related to the boson masses and it follows that the masses of the weak gauge bosons are related to the weak mixing angle θ_W:

$$\cos\theta_W = \frac{M_W}{M_{Z^0}} \tag{2.11}$$

The masses of fermions can be accounted for by adding a mass term $-m\overline{\Psi}\Psi$. As this term is not invariant under $SU(2)_L$ a different approach is necessary. By pairing the field Ψ with an adjoint doublet, like the Higgs doublet ϕ introduced earlier, the invariance can be restored.

The mass term of the Lagrangian for an electron can then be written as:

$$\mathcal{L}_{\text{Yukawa elec.}} = -G^e\left((\overline{\nu}_e \quad \overline{e})_L\begin{pmatrix}\phi^+\\ \phi^0\end{pmatrix}e_R + \overline{e}_R(\overline{\phi}^+ \quad \overline{\phi}^0)\begin{pmatrix}\nu_e\\ e\end{pmatrix}_L\right) \tag{2.12}$$

Here the Yukawa coupling of the electron is $G^e = \sqrt{2}\frac{m_e}{v}$ and thus connects the vacuum expectation value of the Higgs with the mass of the fermion.

Combining these Lagrangians the full Lagrangian function for the EW sector can be written as:

$$\mathcal{L}_{EW} = \mathcal{L}_{gauge} + \mathcal{L}_{matter} + \mathcal{L}_{Higgs} + \mathcal{L}_{Yukawa} \tag{2.13}$$

Where $\mathcal{L}_{gauge}$ is the gauge term, $\mathcal{L}_{matter}$ includes the interaction of the bosons from Eqn. 2.4, $\mathcal{L}_{Higgs}$ is Eqn. 2.8 and $\mathcal{L}_{Yukawa}$ is Eqn. 2.12 generalized to all fermions. This complete Lagrangian is by construction invariant under gauge transformations from $SU(2)_L$ and $U(1)_Y$.

Quantum Chromodynamics

The Quantum Chromodynamics (QCD) is represented by $SU(3)_C$ with the color charge C. The full Lagrangian can be written as

$$\mathcal{L} = \overline{\Psi}\left(i\not{D} - m_q\right)\Psi - \frac{1}{4}F^{\mu\nu,a}F_{\mu\nu,a} \tag{2.14}$$

with the gauge covariant derivative $D^\mu = \partial^\mu + igA_a^\mu\frac{\lambda_a}{2}$ and the gauge invariant gluonic field tensor $F^{\mu\nu,a} = \partial^\mu A^{\nu,a} - \partial^\nu A^{\mu,a} - g[A^{\mu,a}, A^{\nu,a}]$. This definition includes the eight gluon potentials $A^{\mu,a}$, the coupling constant g and the generators from $SU(3)$ λ_i.

The main feature of QCD is the color-charge of quarks and gluons, with the quarks holding a single color charge and the gluons holding a color and anti-color simultaneously. As the gluons interact with color charged particles, they can interact with other gluons, which makes it possible to find three or four gluon vertices.

The coupling strength of QCD α_S is found to be a function of the squared momentum transfer q^2. It can be expressed in terms proportional to $\alpha^n[\ln(q^2/q_0^2)]^m$. In the so-called *leading log approximation* only terms with $n = m$ are kept which omits negligible terms and speeds up calculations. The coupling strength in leading log approximation can be written as:

$$\alpha_S(q^2) = \frac{\alpha_S(q_0^2)}{1 + B\alpha_S(q_0^2)\ln(q^2/q_0^2)} = \frac{1}{B\ln(q^2/\Lambda^2)} \tag{2.15}$$

Here $B = (33 - 2f)/12\pi$ is a factor depending on the number of quark flavors f and $\Lambda^2 = q_0^2\exp(-1/B\alpha_S(q_0^2))$. For less than 17 quark flavors the coupling decreases for increasing q^2, while for smaller q^2 the coupling increases. The small coupling at large q^2 and thus small distances between quarks, is called *asymptotic freedom*. Quarks in this regime act as free particles as gluons that are surrounding the quarks effectively reduce the color charge as seen by other quarks at close distances.

In the regime of large couplings for $\Lambda^2 \approx q^2$ the perturbation theory breaks down. In perturbation theory quantities can be expressed in terms of powers of the coupling. As higher orders can only be omitted when $\alpha \ll 1$, a large coupling makes this approach impracticable. For large distances and thus small q^2 the quarks observe a so-called *confinement* in a potential of the form:

$$V(r) = -\frac{4}{3}\frac{\alpha_S}{r} + k \cdot r \tag{2.16}$$

Where r is the distance of the quarks and k is a constant describing the system similar to Hooke's law. The first term resembles a Coulomb type interaction. When quarks are separated then a string of gluons holds them together similar to a spring. When the energy stored in this tube of gluons exceeds the energy needed to pair-produce a quark-antiquark pair, then the tube splits in two quark pairs. This property leads to a confinement of quarks, and makes it impossible to find single free quarks.

These remaining colorless states can consist of a quark-antiquark pair, or of three quarks with different color (red+green+blue=colorless). Those bound states are called *hadrons*, which are further divided depending on the number of quarks included. A quark-antiquark pair is called *meson*, while a state consisting of three quarks is called *baryon*.

BEYOND THE SM

The presented Standard Model of particle physics is a very successful model, that was able to explain and predict many particles and their properties within a rather simple theoretical framework. A large number of experiments have been performed to find discrepancies between nature and the Standard Model. None of these experiments was able to find a significant hint for physics beyond the SM. Nevertheless there are observations in cosmology and basic considerations about the theory that imply that the SM might be a low energy-approximation of a more basic theory.

Observations of rotational curves of the Milky Way and of galaxy clusters showed that the orbital speed as a function of the distance to the galaxies center is not compatible with the prediction by Kepler-like orbits. Thus a large fraction of matter is interacting gravitationally but is unseen by telescopes. This matter is called *Dark Matter* as it does not interact electromagnetically and thus does not emit light.

Further the effect of gravitational lensing of light around large masses is used to determine the mass of galaxies which can be compared to the mass estimated by the light emitted. A discrepancy in these values also hinted to Dark Matter.

The most striking observation was made by combining X-ray observations of the Bullet Cluster with gravitational lensing measurements [29, 30]. The center of gravity observed by these two complementary methods is not in agreement, which points also to Dark Matter.

Measurements of the cosmological microwave background [31, 32] show that the matter described by the SM accounts for only 4.8 % of the energy in the universe, while 26.1 % are Dark Matter and the remaining 69.1 % are the still unexplained so-called *Dark Energy*.

The main arguments for physics beyond the Standard Model are:

GRAVITY The theory of special relativity describes the gravitational interaction between massive particles. A unification of the SM with the special relativity would complete the description of forces within one model. One possibility would be by introducing extra spatial dimensions, in which the coupling strength of gravity is comparable to the electro-weak coupling. For large distances compared to the size of the extra-dimensions, the gravitational force would not be able to penetrate to the extra dimensions, thus obtaining the observed 4 dimensional behavior of gravity.

UNIFICATION OF FORCES The observed interactions in the SM are depending on the energy. One explanation are theories of Grand Unification (GUT). Those theories imply that at higher energies or temperatures the coupling strengths of the forces are converging and a unified force is expected to appear.

NATURALNESS The large discrepancy between the strength of the gravitational and weak interactions is called problem of *Naturalness*. It implies a highly fine-tuned mass of the Higgs boson, as radiative corrections at high energies are very close to the bare mass of the Higgs.

DARK MATTER AND DARK ENERGY The Standard Model does not have a viable candidate for Dark Matter or an explanation for Dark Energy and is thus incomplete.

There is a large variety of models trying to overcome the above mentioned shortcomings of the SM. A short overview of the models examined in this work follows.

Excited Quark

If quarks are composite particles then excitations of quarks are expected. The so-called *Excited Quark* [33, 34] would decay in 83 % of the cases to an ordinary quark and a gluon, the remaining times it would decay in quark plus $W/Z/\gamma$.

The Lagrangian showing the vector-like coupling to quarks and gluons is:

$$\mathcal{L}_{\text{gauge}} = \overline{f^*}\gamma^\mu \alpha_S(m_*)\frac{\lambda^a}{2}A_\mu^a f^* \tag{2.17}$$

With the fermion field for the excited fermions f^*, the Dirac matrices γ_μ, the strong coupling constant α_S, the generators from SU(3) λ^a and the gluon field A_μ^a, with color a.

The corresponding decay width is:

$$\Gamma(q^* \to gq) = \frac{1}{3}\alpha_S(m_*)f_s^2\frac{m_*^3}{\Lambda^2} \tag{2.18}$$

The coupling strength f_s is chosen to be unity and the scale of New Physics Λ is chosen to be equal to the mass of the excited quark m_*, hence the relative decay width is $\Gamma/m_* = \alpha_S(m_*)/3$.

Color Scalar Octet

Several models introduce a spin zero particle with an octet color structure [35–38], similar to the color of gluons. These particles arise in Technicolor models, in models with universal extra dimensions and also as sgluons in supersymmetric models.

The interaction can be written as:

$$\mathcal{L}_{gg\,S8} = \alpha_S(m_{S8})d^{ABC}\frac{\kappa_S}{\Lambda_S}S_8^A F_{\mu\nu}^B F^{C,\mu\nu} \tag{2.19}$$

With the scalar octet field S_8^A with color A, the field strength tensors of QCD $F_{\mu\nu}^B$ with color B and the structure constants from the anti-commutator rules in QCD d^{ABC}. Here the coupling constant κ_S is chosen to be unity, and the scale of New Physics $\Lambda_S = m_{S8}$ is equal to the mass of the Scalar Octet (S8).

The decay width of these particles is given as:

$$\Gamma(S8 \to gg) = \frac{5}{3}\alpha_S(m_{S8})\kappa_s^2\frac{m_{S8}^3}{\Lambda^2} \tag{2.20}$$

Using $\kappa_S = 1$ and $\Lambda_S = m_{S8}$, this gives a relative decay width of $\Gamma/m_* = \alpha_S(m_{S8}) \cdot 5/3$ and hence 5 times the width expected for an excited quark.

Heavy Gauge Bosons

A heavy partner of the charged gauge bosons with also spin-1 nature called W' is expected from a large variety of models [39–46]. A W' is predicted in Grand Unified Theories, in left-right symmetric models, in models with little Higgs, in models with the Higgs as pseudo-Goldstone boson and as excitations in Kaluza-Klein models.

All of these implementations have the same structure for the charged current interaction to quarks as:

$$\mathcal{L}_{CC}{}^{q} = W_{\mu}^{+}\overline{u^{i}}(\gamma^{\mu}v_{ij} + \gamma^{\mu}\gamma_{5}a_{ij})d^{j} + W_{\mu}'^{+}\overline{u^{i}}(\gamma^{\mu}v'_{ij} + \gamma^{\mu}\gamma_{5}a'_{ij})d^{j} + h.c. \tag{2.21}$$

Here the W_{μ}^{+} represents the SM W boson, while W'^{μ} gives the heavy partner. Further the Dirac fermions are u^{i} and d^{i}, and the coupling constants v_{ij}, a_{ij}, v'_{ij} and a'_{ij} consist of the CKM matrix plus an additional right-handed mixing matrix.

The decay width of a heavy gauge boson is dependent on the mixing angles and the coupling strength. For unity coupling and negligible mixing the relative decay width is $\Gamma/m_{W'} \approx 2.5\,\%$.

Chiral W* Boson

Another possible extension is to add a doublet of massive vector fields $V_{\mu} = (Z_{\mu}^{*}, W_{\mu}^{*})$ with similar quantum numbers as the SM Higgs boson [47–50]. This leads to an interaction that is of tensor character:

$$\mathbf{L} = \frac{1}{M}\sum_{f}(g_{LR}^{f}\overline{\Psi_{L}^{f}}\sigma^{\mu\nu}\psi_{R}^{f}D_{\mu}V_{\nu} + g_{RL}^{f}D_{\mu}^{\dagger}V_{\nu}^{\dagger}\overline{\psi_{R}^{f}}\sigma^{\mu\nu}\Psi_{L}^{f}) \tag{2.22}$$

Here f denotes the fermion family, Ψ_{L}^{f} are the left-handed doublets and ψ_{R}^{f} are the right-handed singlets. The couplings are denoted as g_{LR}^{f} and the scale of New Physics as M. The covariant derivative is D^{μ} and the Dirac tensor $\sigma^{\mu\nu}$.

This theory is interesting as it provides a different angular distribution of the decay fermions. Usual heavy gauge bosons obey a decay proportional to $1 + \cos^{2}\theta$, while W^{*} decays according to $\cos^{2}\theta$ with θ being the angle between initial parton and outgoing fermion.

Quantum Black Holes

One consequence of possible extra spatial dimensions is the existence of Black Holes. The conditions at the LHC favor the production of Quantum Black Holes [51–54], which include effects of quantum gravity. Additionally to the usual 4 dimensions of spacetime a flat spatial n-dimensional torus could exist. Depending on the radius of this torus and the number of extra dimensions, gravity becomes strong at energies observable at collider experiments.

Under the assumption that the Planck scale in 4+n dimensions is of the order of the black hole produced in a proton-proton collision, this black hole would not decay thermally via Hawking radiation but would behave similar to a particle resonance. The most probable decay channel

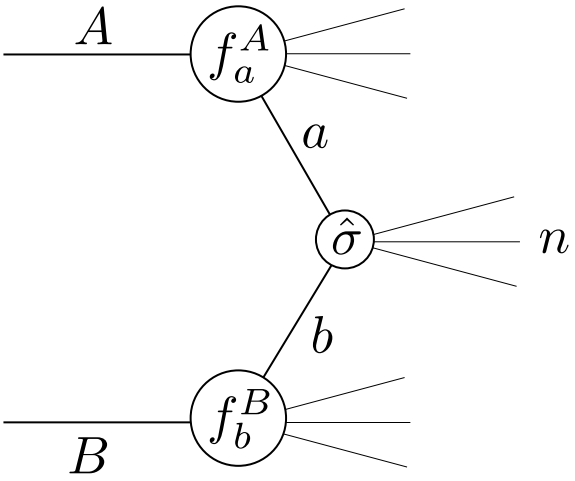

Figure 2.2: Schematic view of proton proton collision between proton with momentum A and proton with momentum B.

would be in two quarks, two gluons or a gluon and a quark. Here only black holes of ADD type [55, 56] are considered.

PROTON–PROTON COLLISIONS

The rate of processes observed in proton-proton collisions can be calculated via the cross-section (see [57]). A sketch of the situation is shown in Fig. 2.2. In the collinear factorization [58] the cross-section for a process $A + B \to X + n$ can be written as:

$$\sigma = \sum_{a,b} \int_0^1 dx_a dx_b \int f_a^A(x_a, \mu_F) f_b^B(x_b, \mu_F) d\hat{\sigma}_{a+b\to n}(\mu_F, \mu_R) \tag{2.23}$$

Here $f_a^A(x_a, \mu_F)$ and $f_b^B(x_b, \mu_F)$ are the parton distribution functions (PDF) which depend on the momentum fraction x relative to their parent hadron A,B and the factorization scale μ_F. The cross-section of the sub-process $a + b \to n$ can be written as:

$$d\hat{\sigma}_{a+b\to n}(\mu_F, \mu_R) = d\Phi_n \frac{1}{2\hat{s}} |M_{a+b\to n}|^2 (\Phi_n; \mu_F, \mu_R) \tag{2.24}$$

With the renormalization scale μ_R, the differential phase space element for the n final-state particles $d\Phi_n$ and the matrix element squared $|M_{a+b\to n}|^2$.

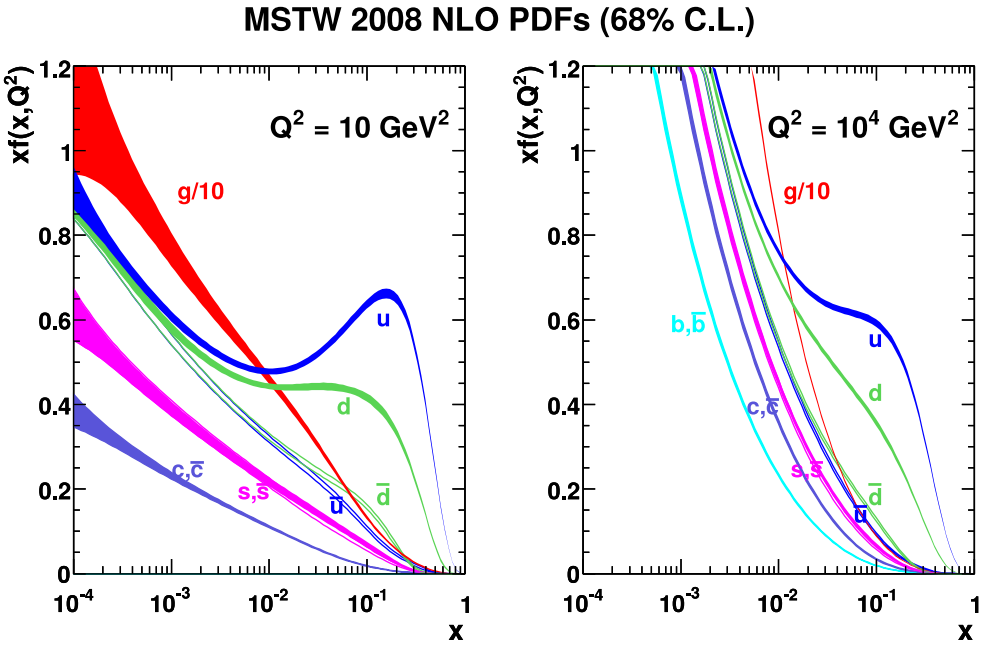

Figure 2.3: Parton Density Function from CTEQ collaboration [62].

For this calculation two arbitrary scales have to be chosen, the factorization scale roughly separates the regime of long and short-distance physics while the renormalization scale affects the evaluation of the running coupling constant (see q^2 in Eqn. 2.15). A common choice is to set both parameters $\mu_F = \mu_R$ equal to the energy scale of the involved process, e.g. the mass of the resonance. The dependence of the physical cross-section on these unphysical parameters vanishes for the full result of the matrix element and the sub-process cross-section. As only approximate solutions of these results are available expressed in orders of the strong coupling, the uncertainty on the resulting calculation can be estimated by varying the unphysical parameters.

The dependence of PDFs on the factorization scale can be obtained from the Dokshitzer-Gribov-Lipatov-Altarelli-Parisi (DGLAP) evolution equations [59–61]:

$$\frac{\partial q_i(x,\mu_F^2)}{\partial \log \mu_F^2} = \frac{\alpha_S}{2\pi}\int_x^1 \frac{dz}{z}\left(P_{q_i,q_j}(z,\alpha_S)q_j(\frac{x}{z},\mu_F^2) + P_{q_i,g}(z,\alpha_S)g(\frac{x}{z},\mu_F^2)\right) \tag{2.25}$$

$$\frac{\partial g(x,\mu_F^2)}{\partial \log \mu_F^2} = \frac{\alpha_S}{2\pi}\int_x^1 \frac{dz}{z}\left(P_{g,q_j}(z,\alpha_S)q_j(\frac{x}{z},\mu_F^2) + P_{g,g}(z,\alpha_S)g(\frac{x}{z},\mu_F^2)\right) \tag{2.26}$$

With the PDFs for quarks $q_i(x,\mu_F^2)$ and gluons $g(x,\mu_F^2)$ and the Altarelli-Parisi splitting functions $P_{ab}(x,\alpha_S)$ [61] which can be calculated in a perturbative expansion.

The dependence of the quark and gluon PDFs on the momentum fraction x have to be extracted from measurements from deep-inelastic scattering, Drell-Yan processes and jet production. A global fit to a selected subset of these measurements is performed by several groups. The main PDFs used at the LHC are calculated from the CTEQ [62], MSTW [63], NNPDF [64] and HERAPDF [65] groups.

The result from the CTEQ collaboration for two different values of the momentum transfer Q^2 is shown in Fig. 2.3. The proton consists of two up-quarks and one down-quark, the so-called *valence quarks*. At low Q^2 the proton is dominated by its valence quarks, which carry each roughly 1/3 of the momentum. Thus the u-quark and d-quark distributions both show a maximum close to $x = 1/3$. The quark-antiquark pairs produced dynamically from the vacuum, the so-called *sea quarks* and the gluons only carry small momentum fractions. For larger Q^2 the distribution of the valence quarks is shifted to smaller momentum fractions, while the sea-quarks carry larger fractions of x. This can be explained by the increased transferred momentum, which increases the number of produced quark-antiquark pairs, and thus the sea quark distributions carry larger fractions of the protons momentum.

The matrix elements $|M_{a+b\to n}|^2$ are also calculated perturbatively by including additional parton radiation or loop processes. For estimating a cross-section the orders kept for the matrix element calculation and the splitting functions in the PDFs have to be matched.

MONTE CARLO SIMULATION

To simulate the outcome of a proton-proton collision many different aspects have to be taken into account [67]. The full proton-proton collision is shown in Fig. 2.4. Starting from the hard-scatter process (red circle) described in Sec. 2.4.1 a more detailed description is necessary. Additional radiation before and after the hard-scatter occurs and has to be taken into account, and modeled correctly as explained in Sec. 2.4.2. Apart from the hard scatter process, other interactions from the remaining proton debris have to be accounted for, the so-called *underlying event* (violet ellipse). As protons are collided in bunches of protons, apart from the interesting hard scatter process additional interactions between protons are found, this has to be simulated as described in Sec. 2.4.3. Finally as partons cannot be found freely, the building of hadrons is simulated (green ellipse) as outlined in Sec. 2.4.4.

Hard Scatter Process

As an input to calculating the hard scatter process at a fixed-order as shown in Sec. 2.3 only two ingredients are necessary, the PDF and the matrix element of the process under consideration. The PDFs are obtained from the fit to measurements and provided by various groups. The matrix

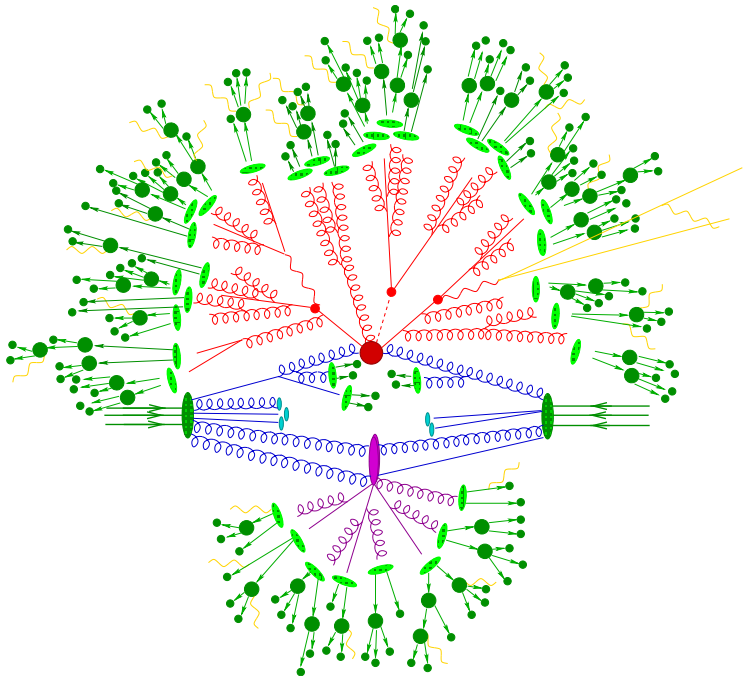

Figure 2.4: Pictorial representation of full proton-proton collision [66].

elements have been calculated to several orders by theorists, by including Feynman diagrams with additional loops or additional outgoing partons. For a large variety of processes these matrix elements are available reaching up to next-to-next-to-next-to-leading order (N^3LO). In the computation of these higher order contributions divergencies show up which require more sophisticated theoretical treatments [68–70].

Parton Shower

Gluons and quarks emerging from the hard scatter vertex can also undergo gluon radiation, gluon splitting or quark-antiquark production. To model these effects correctly the Altarelli-Parisi splitting functions P_{ji} are used. The probability to see no branching between the scales Q^2 and Q_0^2 is then given by the Sudakov form factor:

$$\Delta_i(Q^2, Q_0^2) = \exp\left(-\int_{Q_0^2}^{Q^2} \frac{dk^2}{k} \frac{\alpha_S}{2\pi} \int_{Q_0^2/k^2}^{1-Q_0^2/k^2} dz P_{ji}(z)\right) \tag{2.27}$$

By iteratively adding partons to the hard scatter partons, these evolve towards lower scales, until they reach the energies around 1 GeV where they are confined in hadrons. Adding these

partons can approximate the effect of higher-order corrections and thus predict a rough *all-order* approximation.

The same procedure is followed for the initial state partons. Here the two scales two consider are given by the hard scatter at high Q^2 and low momentum fraction x on one hand, and the low Q^2 and high x values from the initial parton on the other hand. These emissions are calculated backwards, starting from the hard scatter, and stopping the evolution as soon as an infrared cutoff value is reached, at which the regime of the hadron is reached. Depending on the generator used, this evolution is ordered in transverse momentum (Pythia [71]) or in angular separation (Herwig [72]).

Underlying Event and Pileup

In addition to the partons originating directly from the hard scattering, there are more interactions to take into account. Additional collisions are occurring between remnants of the colliding protons (multi-parton interaction) as well as collisions of diffractive and non-diffractive nature between other protons in the collision (pileup).

Those processes also undergo the parton shower procedure as outlined above. Another subtlety to consider, is the non-negligible Fermi momentum of partons in the proton which can lead to an initial transverse momentum. The nature of this has to be described non-perturbatively by a model. This model covers the initial Fermi momentum, as well as the evolution of the parton shower beyond the infrared cutoff.

Hadronization

The final step in the simulation, the so-called *hadronization*, models the transition from color-charged partons to colorless hadrons. This regime cannot be calculated perturbatively and could be covered in the future by lattice QCD calculations. For the time being phenomenological models that use the properties of QCD in the regime of the confinement are used.

One of these models is the Lund *string* model [71] which uses the fact that the potential between quarks can be described by Hooke's law, while omitting the Coulomb term. The model describes the outgoing partons as confined in a string where they are arranged in color, with one quark at each end of the string. These strings produce hadrons by quark-antiquark pair-production in the intense color field between the two quarks.

An alternative model is the *cluster* model [72] which groups two partons to a colorless cluster. These clusters have an universal mass distribution, independent of the momentum transfer. These clusters then undergo isotropic decays into pairs of hadrons.

The simulation then also calculates the decay of these hadrons, according to measured decay properties.

3 THE LHC AND THE ATLAS DETECTOR

The dataset analyzed in this work was recorded by the ATLAS detector which detects the products of proton-proton collisions. The protons have been accelerate and brought to collision by the Large Hadron Collider. In Sec. 3.1 the Large Hadron Collider is discussed. The ATLAS detector is presented in Sec. 3.2.

THE LARGE HADRON COLLIDER

The Large Hadron Collider (LHC) [73] is a hadron-hadron collider situated at the French-Swiss border close to the lake Geneva at the European Organization for Nuclear Research (CERN). It has been approved in 1994, and started its first operation in 2009. The collider is housed in the tunnel which was formerly used by the electron-positron collider LEP [74] until it got dismantled in 2000. Also some of the accelerators that have been operating at CERN in the last 60 years are used as successive pre-accelerators to reach the highest energies obtained in collider experiments to date.

Protons are obtained from a bottle of hydrogen by stripping the electrons. The ionized hydrogen is then transfered to the first accelerator step, which is the Alvarez-type linear accelerator LINAC2. The accelerator has a radio-frequency structure of 33 m in length and accelerates protons up to an energy of 50 MeV. The protons are subsequently injected into the Proton Synchrotron Booster (BOOSTER), which is a synchrotron machine with four stacked rings with a circumference of 152 m each, which accelerates the protons to 1.4 GeV. The next step is the Proton Synchrotron (PS). The PS is a synchrotron 628 m in length and is one of the first ones to exploit strong focusing of beams by using alternating gradients. The PS injects protons with an energy of up to 26 GeV in the Super Proton Synchrotron (SPS). The SPS accelerates the protons in a ring of 7 km length up to an energy of 450 GeV. The final step in this cascade is the LHC ring, in which the protons are injected in one evacuated beam pipe clock-wise and another beam pipe counter-clockwise. Here the protons are accelerated to an energy of up to 7 TeV, and brought to collision in four interaction points. These collisions can reach a center of mass energy of up to $\sqrt{s} = 14$ TeV. The full chain of accelerators and the points of collisions are shown in Fig. 3.1. Each of these points is surrounded by a large detector. Two of these detectors are the multi-purpose detectors ATLAS at the south side and CMS [75] at the north side of the LHC. These detectors cover almost 4π of solid angle, and are built to measure momentum, energy

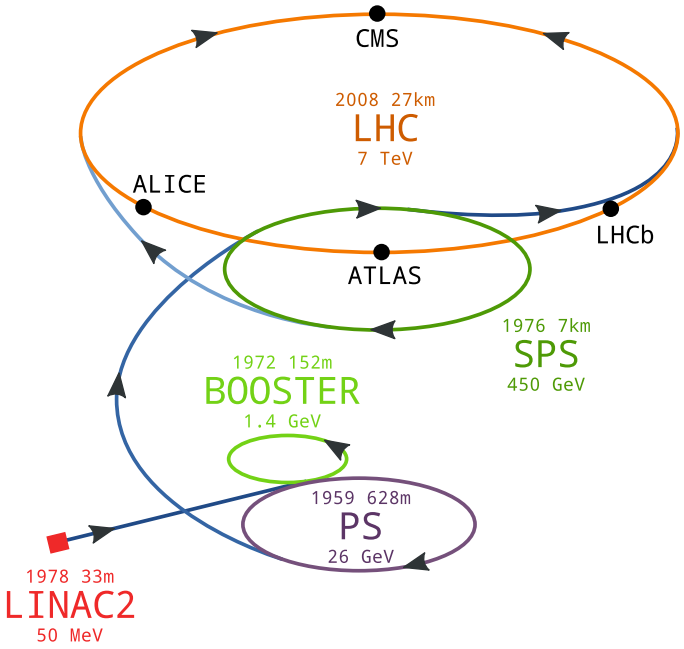

Figure 3.1: Schematic view of accelerators and locations of experiments at LHC. Date of construction, circumference of rings or length of linear accelerator and maximum energy per beam are given.

and charge of the decay products to identify particles and perform a large variety of analyses. The third large detector is the LHCb experiment [76], which probes CP violation in B-physics, it is instrumented in only one hemisphere from the interaction point as it studies very boosted events.

The LHC can also accelerate lead ions, for which another source is used. The ions are accelerated by LINAC3 into the Low Energy Ion Ring (LEIR) and further to the PS from which the same cascade is used as for the proton operation. Lead-lead, proton-lead and proton-proton collisions are thus available in all four collision points. Lead-lead collisions can be performed at a center of mass energy of up to $\sqrt{s} = 1150\,\text{TeV}$, while a maximum of $\sqrt{s} = 571\,\text{TeV}$ was reached in 2012.

The fourth large detector is the ALICE experiment [77] which studies lead-lead and proton-lead type collisions, where very high densities and thus conditions similar to just after the Big Bang are obtained.

Apart from the four big detectors, there are two very forward detectors, and one small detector searching for exotic matter. The LHCf detector [78] is situated 140 m away from the collision point around ATLAS and measures energy and multiplicity of neutral pions under a very small angle to the beam direction. TOTEM [79] is another very forward detector, which is situated close to CMS and consists of roman pots and tracking telescopes to measure the total elastic proton-proton cross-section and diffractive processes.

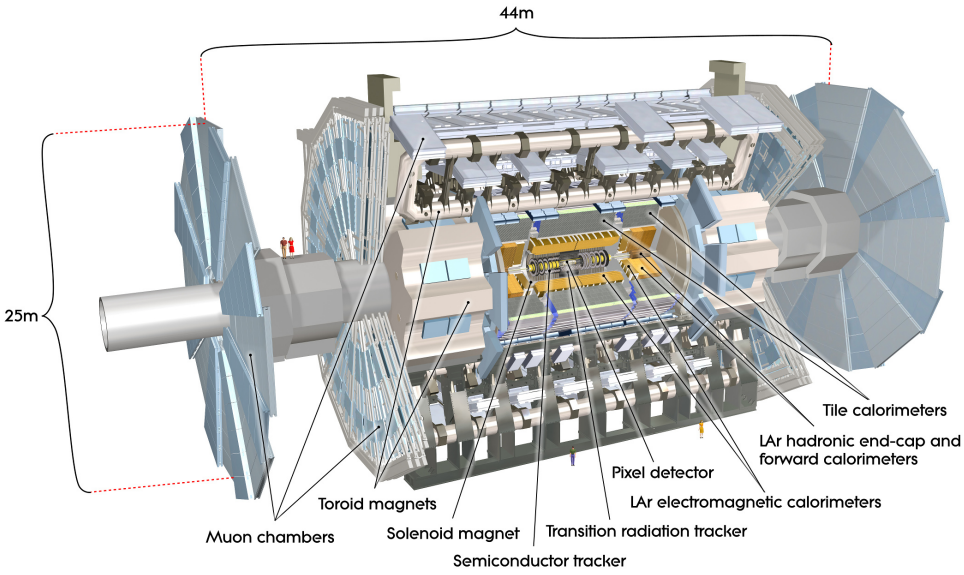

Figure 3.2: Computer generated image of the ATLAS detector in cutaway view [81]. Showing from innermost layer to outermost layer: Inner Detector, electromagnetic calorimeter, hadronic calorimeter and muon spectrometer.

The MoEDAL experiment [80] is a small detector, which is situated in the empty hemisphere close to LHCb. It uses nuclear track detectors to search for magnetic monopoles and other exotic types of matter.

In this thesis events produced in proton-proton collisions are analyzed that have been detected and reconstructed with the ATLAS detector. For proton-proton collisions a nominal center of mass energy of $\sqrt{s} = 14\,\text{TeV}$ is planned, the data shown in this thesis have been recorded with $\sqrt{s} = 8\,\text{TeV}$. Nominally the LHC contains 2808 bunches of protons, with each bunch containing 1.15×10^{11} protons, separated by 25 ns of bunch spacing. This would give an instantaneous luminosity of $\mathcal{L} = 1 \times 10^{34}\,\text{cm}^{-2}\,\text{s}^{-1}$. In 2012 operation 1380 bunches have been used with a bunch spacing of 50 ns, resulting in a maximum instantaneous luminosity of $\mathcal{L} = 7.4 \times 10^{33}\,\text{cm}^{-2}\,\text{s}^{-1}$.

THE ATLAS DETECTOR

The ATLAS (**A** **T**oroidal **L**HC **A**pparatu**S**) detector [81], shown in Fig. 3.2, is a multi-purpose particle detector that was designed to be able to investigate a large variety of New Physics models, while also increasing knowledge in precision measurements of the Standard model. New Physics models of interest include new heavy gauge bosons W′ and Z′, compositeness of quarks, flavor changing neutral currents, lepton flavor violation, anomalous triple and quartic

couplings, extra dimensions and supersymmetry. To search for one of those models that give rise to additional particle production with a very low cross-section, it is necessary to identify particle properties reliably and suppress large backgrounds, especially QCD jet production. Apart from these New Physics motivation, the ATLAS detector is also designed for measuring QCD, electro-weak and flavor processes in the Standard Model with highest precision, to find possible deviations from the predictions. The main priority at the time of building the detector was to find an evidence for a Standard Model Higgs boson. Hence the search for the Higgs boson was an important benchmark in setting the requirements for the detector in terms of acceptance, resolution and identification of leptons and jets.

The high intensity, high energy proton beam delivered by the LHC to the experiments, sets additional requirements on the detector design in terms of radiation hardness, identification of additional inelastic collisions and high rate processing.

To fulfill these requirements ATLAS has been designed as a multi-layer detector. The Inner Detector is used to record the tracks of charged particles, two layers of calorimeters to measure the energy of electromagnetically and hadronically interacting particles and finally a muon system to measure the momentum of muons. The curvature of charged particles in a magnetic field is exploited to measure the momentum of charged particles. For this two magnetic field systems are used in ATLAS. The Inner Detector is surrounded by a solenoid, which generates a magnetic field parallel to the beam-axis and thus does not influence the beam. An additional toroidal magnet generates a magnetic field in the muon system, with field lines in the plane transverse to the beam.

Coordinate System

ATLAS uses a right-handed Cartesian coordinate system. The beam direction is aligned along the z-axis. The x-y plane is transverse to the beam axis, with the x-axis pointing to the center of the LHC and the y-axis pointing upwards.

From this Cartesian system spherical coordinates can be defined. The azimuthal angle ϕ is defined in the x-y plane, the polar angle θ is defined with respect to the beam axis. This polar angle can be expressed in terms of pseudo-rapidity as:

$$\eta = -\ln \tan \theta/2 \tag{3.1}$$

A visualization of different pseudo-rapidities is shown in Fig. 3.3. The ATLAS detector is instrumented up to $|\eta| = 4.83$, which corresponds to less then $\theta = 1^\circ$ from the beam-axis.

The rapidity of a particle can be defined as:

$$y = \frac{1}{2} \ln \left(\frac{E + p_z}{E - p_z} \right) \tag{3.2}$$

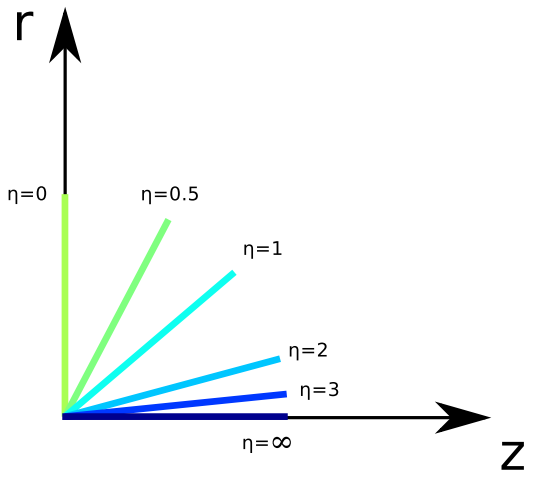

Figure 3.3: Lines of different pseudo-rapidity in r-z plane, where r is the projection of the direction vector on the x-y plane.

Here E is the energy of a particle and p_z is the momentum along the beam axis. For massless particles the rapidity is equal to the pseudo-rapidity. The rapidity is used for massive particles as differences of rapidities are invariant under Lorentz transformations.

Inner Detector

The Inner Detector, which is shown in Fig. 3.4, is the innermost part of the ATLAS detector. It is 6.2 m in length and 2.1 m in diameter and surrounds the evacuated beam pipe that passes through ATLAS. The main goal of the Inner Detector is to measure the momentum of charged particles precisely, while also reconstructing the position of the decay vertex from which these particles emerge. The required resolution of the momentum measurement is determined to be $\sigma_{p_T}/p_T = 0.05\,\% \cdot p_T/\text{GeV} \oplus 1\,\%$ to achieve the desired precision. The coverage in pseudo-rapidity is required to be $-2.5 < \eta < 2.5$. This is achieved by three different detector types.

The innermost layer of the Inner Detector consists of three layers of silicon pixels in the barrel region, which are read out by approximately 80.4 million channels. The end caps are covered by two times three disks. The next layer consists of silicon micro strip detectors (SCT), which form four layers in the barrel region and two times four disks as end caps. These two layers are using semi-conductors, where a traversing particle will produce electron-hole pairs, that are extracted in an electric field and thus measured.

The last layer consists of a transition radiation tracker (TRT) build from straw tubes, here 73 straw planes are used in the barrel region and 160 straw tubes in the end caps. The TRT serves as a tracking detector by using gas-filled straws, where a passing particle produces electron-ion

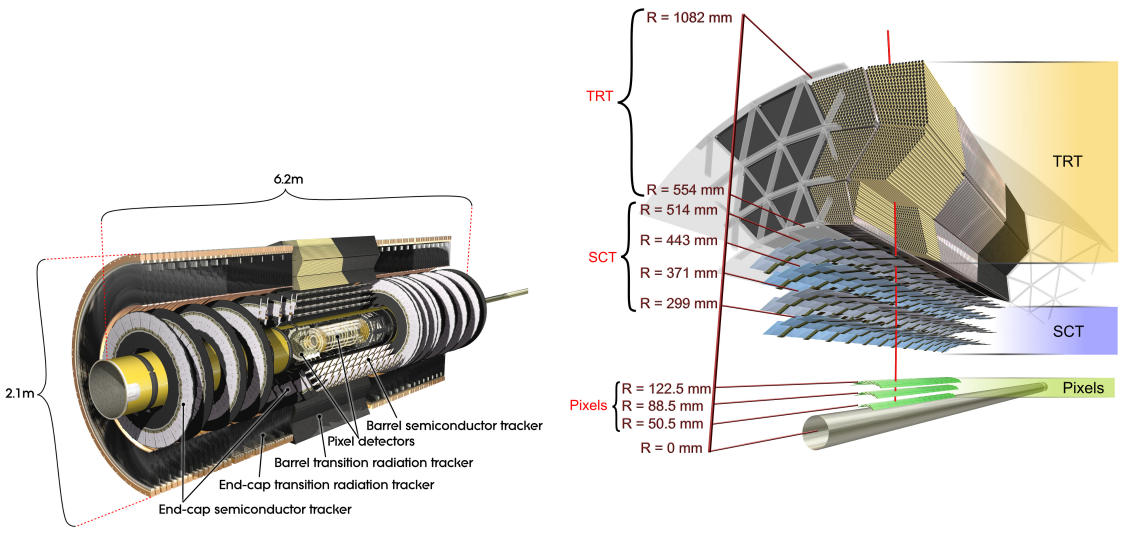

(a) Full view **(b)** Barrel region

Figure 3.4: Computer generated image of the ATLAS Inner Detector in cutaway view [81].

pairs that are measured. Additionally the TRT can identify electrons, which emit X-ray photons when passing a radiator material. These photons are also detected in the gas-filled straws.

The whole Inner detector lies within a magnetic field of $B = 2\,T$, to be able to extract the momentum from the curvature and the charge of the bending particles.

By using this design the Inner Detector is able to cope with the approximately 1000 particles that are expected to penetrate the detector in $|\eta| < 2.5$ every 25 ns.

Calorimeter

The calorimetry in ATLAS measures the energy of particles passing through the detector, except neutrinos and muons. The system is divided in two parts, an electromagnetic calorimeter which stops almost all leptons and a hadronic calorimeter which stops hadrons and the remaining leptons (except muons and neutrinos). The detectors cover a pseudo-rapidity of $|\eta| < 4.9$ with a coarse granularity. To obtain precise measurements of electrons, positrons and photons a finer granularity is used in the pseudo-rapidity region, that is also covered by the Inner Detector. The full calorimeter is shown in Fig. 3.5, in the center of the detector are the electromagnetic and hadronic barrels. The forward region is covered by a liquid argon (LAr) forward calorimeter (FCal), that is surrounded by two end cap wheels and an extended barrel.

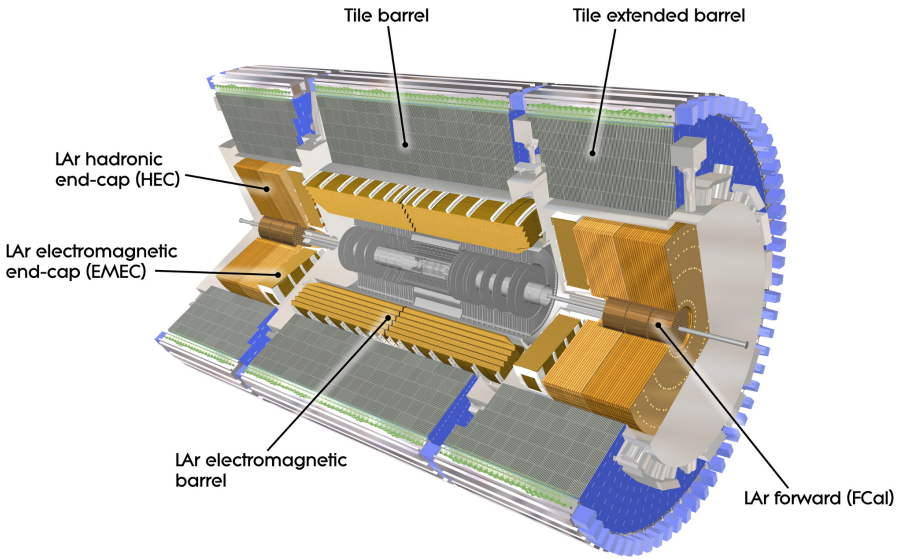

Figure 3.5: Computer generated image of the ATLAS detector calorimeter system in cutaway view [81].

For stopping particles in a detector the thickness in radiation lengths X_0 and interaction lengths λ are important (see also [82]). These two quantities are necessary due to the different nature of hadronically and electromagnetically interacting particles.

An electromagnetically interacting particle that enters matter emits photons. If the energy of one of these photons is above twice the electron rest mass, then a pair of electron and positron is produced. This process develops a so-called *shower* in the calorimeter, with a characteristic length and width.

The mean energy $\langle E \rangle$ after a distance x with an initial energy of E_0 is given as:

$$\langle E \rangle = E_0 e^{-\frac{x}{X_0}} \tag{3.3}$$

The radiation length X_0 gives the distance at which the energy of the particle is lowered to $1/e$.

A hadronically interacting particle also develops a shower when passing through matter. Mainly pions are produced. If neutral pions are produced, they decay to two photons, which can develop an electromagnetically shower as described before. Charged pions can decay in muons, which are not contained in the calorimeter or neutrons which can transfer parts of their energy in nuclear excitation to the detector material. Thus the energy in a hadronically shower is not fully measurable in the calorimeter, and the shape of the shower follows a different characteristics than for the electromagnetic case.

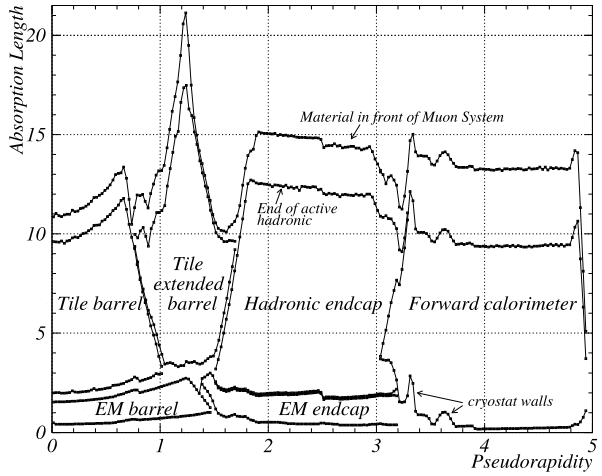

Figure 3.6: Material in ATLAS calorimeter in absorptions lengths [83].

The interaction length λ characterizes the mean distance a hadronic particle travels until it interacts in an inelastic nuclear reaction. It is dependent on the inelastic cross-section σ_i and element specific properties as the molar mass A and the density ρ.

Typical values of the radiation length X_0 for the materials used in the calorimeter are 0.56 cm (lead) or 1.76 cm (iron). The interaction length λ is much larger for these and found to be 17.59 cm (lead) and 16.78 cm (iron) [84].

In ATLAS the electromagnetic calorimeter has $> 22\,X_0$ in the barrel region and $> 24\,X_0$ in the end caps region. An overview of the absorption length in a quarter of the calorimeter is shown in Fig. 3.6. The calorimeter provides at least 11 λ up to a rapidity of $|\eta| = 4.9$ including non-active parts, like support structures or cables. This large number of interaction lengths guarantees a minimal number of particles not being stopped completely by the calorimeters, and thus lost for the calculation of energy and missing transverse energy.

Electromagnetic Calorimeter

The electromagnetic calorimeter is shown in Fig. 3.7. It is the innermost part of the calorimetry and is divided in a barrel region that spans $|\eta| < 1.475$ and two end cap wheels that cover $1.375 < |\eta| < 3.2$. The calorimeter is built as a sampling detector, with liquid argon (LAr) as active material and lead plates as absorbers. The kapton electrodes are accordion-shaped, thus providing full ϕ-symmetry without a crack.

The barrel consists of two half-barrels that are separated by a 4 mm gap at $z = 0$. The end cap is divided in an inner wheel at $1.375 < |\eta| < 2.5$ and an outer wheel at $2.5 < |\eta| < 3.2$. The barrel and end caps each use their own cryostat, while sharing one vacuum vessel, together with the solenoid. This decreases the amount of inactive material passed by particles before entering the calorimeter. To estimate the inevitable energy loss due to inactive material accurately the

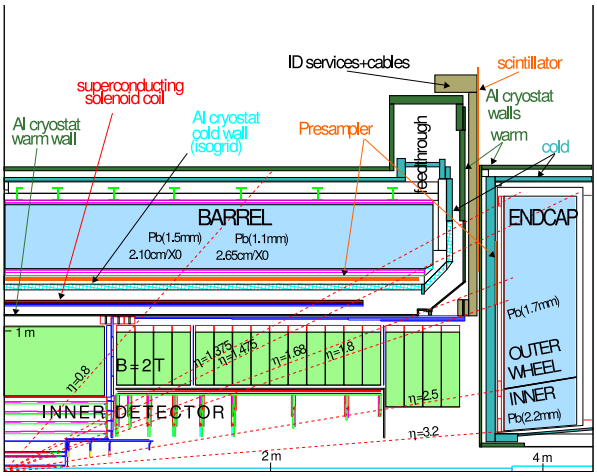

Figure 3.7: Quadrant of electromagnetic calorimeter and Inner detector [83].

so-called *presampler*, an active LAr layer, is placed in front of the calorimeter covering $|\eta| < 1.8$. In the barrel the presampler is 1.1 cm thick, in the end caps it is 0.5 cm thick.

In the barrel and end cap region, the calorimeter consists of three layers of cells with decreasing granularity. The segmentation of the barrel calorimeter cells is shown in Fig. 3.8, in the barrel region the cell size varies from $\Delta\eta$ x $\Delta\phi = 0.025$ x 0.025 to 0.05 x 0.025. In the end cap the granularity ranges from 0.025 x 0.025 to 0.1 x 0.1. This design leads to an energy resolution of better than 2 % for medium and high energy electrons.

Hadronic Calorimeter

The hadronic calorimeter is divided in tile calorimeter, LAr hadronic end cap and LAr forward calorimeter. The tile calorimeter consists of a barrel region at $|\eta| < 1.0$ and an extended barrel at $0.8 < |\eta| < 1.7$. Both barrels are divided in 64 modules in the azimuthal coordinate and in three layers in radial component. The modules contain the sampling calorimeter, that is built from steel absorbers and scintillating tiles. The tiles are read out on two sides by wavelength shifting fibers, that feed light in photomultipliers.

The LAr hadronic end caps consist of two wheels on each side which cover $1.5 < |\eta| < 3.2$, thus overlapping with the coverage of the tile and the forward calorimeter. Each wheel is segmented in two segments in depth. The end caps are built from 32 identical wedge-shaped modules, which are made from copper plates with a 8.5 mm gap that is filled with LAr as active material.

The LAr forward calorimeter covers $3.1 < |\eta| < 4.9$ and is placed 1.2 m shifted from the front face of the electromagnetic calorimeter, to reduce the neutron flux in the calorimeter. Thus the calorimeter is required to be of high-density, which is obtained with an interaction length of more than $10\,\lambda$. The calorimeter is divided in three modules. The first module is made from copper, which is optimal for measuring electromagnetic interactions. The second and third layer

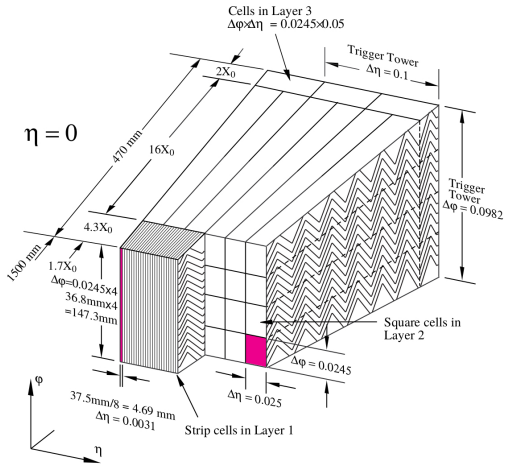

Figure 3.8: Sketch of a barrel module, showing the granularity of the three layers [81].

are build from tungsten, and hence optimized for measuring hadronic interactions. All modules are formed as metal matrices with electrodes in evenly distributed channels, with LAr in a gap between electrode and channel surface.

The energy resolution obtained in test beams with pions is shown in Fig. 3.9. Here a measurement combining the tile and LAr parts of the detector is used. The energy resolution is estimated from a fit to be:

$$\frac{\sigma_E}{E} = \frac{52.05\,\%/\sqrt{\text{GeV}}}{\sqrt{E}} \oplus 3.02\,\% \oplus \frac{1.59\,\text{GeV}}{E} \tag{3.4}$$

Each of these three parameters is estimated with a relative accuracy of about 10 %. Results from using the forward calorimeter give an energy resolution that is up to a factor of 2 worse than for the central part of the calorimeter.

Muon System

The muon system consists of four types of detectors that are in a magnetic field of up to $B = 4\,T$ generated by a barrel toroid magnet and two end cap toroids. It is the outermost layer of the ATLAS detector and thus it is 44 m in length and 25 m in height. The momentum of muons is measured by observing bent tracks in a magnetic field. The detector components used are three layers of chambers that are installed in the barrel region. In the end cap region three disks of chambers are used. One detector type used for the precision tracking are monitored drift tubes, which cover $|\eta| < 2.7$ and consist of 1088 chambers with a total of 339 000 channels. Also used for the tracking are cathode strip chambers that cover $2.0 < |\eta| < 2.7$ and consist of 32 chambers with 31 000 channels. For triggering and to obtain a second coordinate resistive plate chambers are

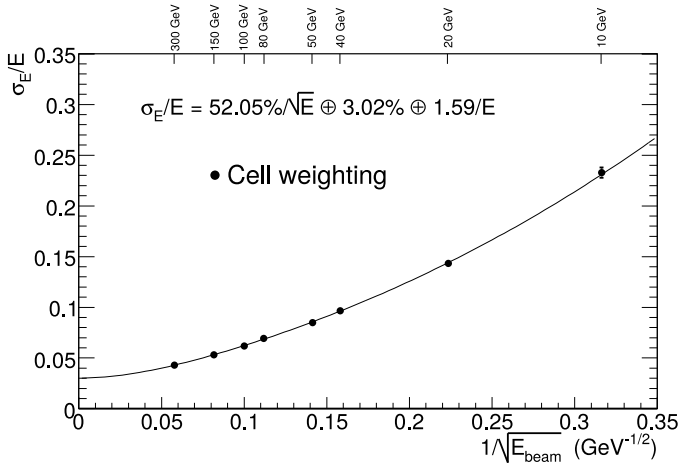

Figure 3.9: Relative energy resolution for pions measured with combined LAr and tile calorimetry at $|\eta| = 0.25$ [81].

used. These cover a region of $|\eta| < 1.05$ and consist of 544 chambers with 359 000 channels. For the same reason thin gap chambers that cover $1.05 < |\eta| < 2.7$ which consist of 3588 chambers and 318 000 channels, are used.

The full muon system is shown in Fig. 3.10.

From Particles to Signals

Particles passing through one of the former mentioned detector parts, interact with matter and depending on the detector component an energy or only the position of the particles trajectory is registered.

In the pixel and SCT part of the Inner Detector [85, 86] a charged particle produces electron-hole pairs in a semiconductor, which are separated by an electric field. The resulting current is amplified by electronics and if exceeding a threshold the passing is recorded. In the TRT part of the Inner Detector the radiation obtained from relativistic particles passing through the border between two materials is exploited to identify particles. In the straws of TRT also electron-ion pairs are produced in a gas. Thus the number of produced electrons is registered.

In the tile calorimeters [87] a current pulse from a photomultiplier is amplified and shaped. The incoming signal is a charge signal with a full-width at half-maximum (FWHM) of 15 ns, that is shaped into a unipolar voltage signal with 50 ns FWHM and an amplitude that is proportional to the input charge. The output signal is then read by a fast digitizer module.

In the LAr calorimeters [88] particles passing through the detector ionize the liquid argon. The produced electrons and ions drift to the electrodes and thus the charge signal consists of a fast rise of a few ns due to the electron drift time, followed by a slow linear decay for the duration

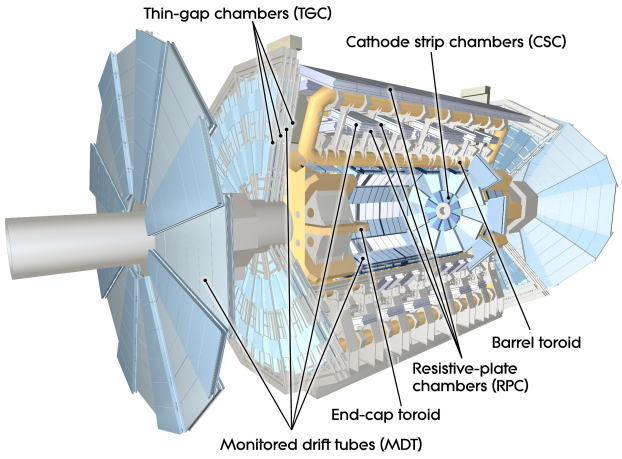

Figure 3.10: Computer generated image of the ATLAS detector muon system in cutaway view [81].

of the ion drift time. Here the peak current measured I_0 is proportional to the energy registered in the calorimeter. This charge signal is then formed into a voltage signal with a narrow positive peak and broad negative peak as shown in Fig. 3.11. The area between the positive peak and the x-axis and the negative peak and the x-axis are identically, this ensures a base line subtraction that is optimized for $\mathcal{L} = 1 \times 10^{34}\,\mathrm{cm}^{-2}\,\mathrm{s}^{-1}$. This shape and the shaping time constant are optimized to reduce the influence of pile-up noise, which increases with longer signal response. While contrary to this the thermal electronic noise increases with shorter shaping time.

In the muon system [89] muons that are passing the chambers leave pairs of electrons and ions in the chamber gas. Those pairs are separated by an electric field and the charges are collected, amplified and shaped.

Trigger System

To be able to record interesting physics events a trigger system has be used. The main goal of the trigger is to reduce the data rate observed in 2012 of up to $32\,\mathrm{TB\,s}^{-1}$ to a rate of up to $1.6\,\mathrm{GB\,s}^{-1}$, which can be recorded within the capabilities of the data acquisition system. To achieve this the ATLAS trigger system [90] is divided in three steps, which are summarized in Fig. 3.12.

In the first level (L1) an initial selection of events is performed, which reduces the data rate to 0.3 % of the initial rate. For this selection information of a subset of detectors is available, thus for example tracking information are not accessible. The level of detail is also reduced, which is achieved by processing only lower granularity information from the calorimeters and ignoring parts of the muon system. In L1 events are selected based on transverse momentum of muons, electrons/positrons, photons, jets or hadronically decaying tau-leptons. Additionally missing transverse momentum or the sum of transverse energy is available. Any of these properties or a

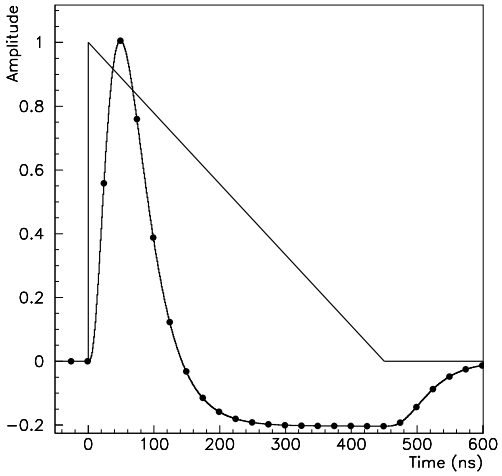

Figure 3.11: Triangle shaped pulse in current from LAr barrel electromagnetic cell and corresponding output after bipolar shaping [81].

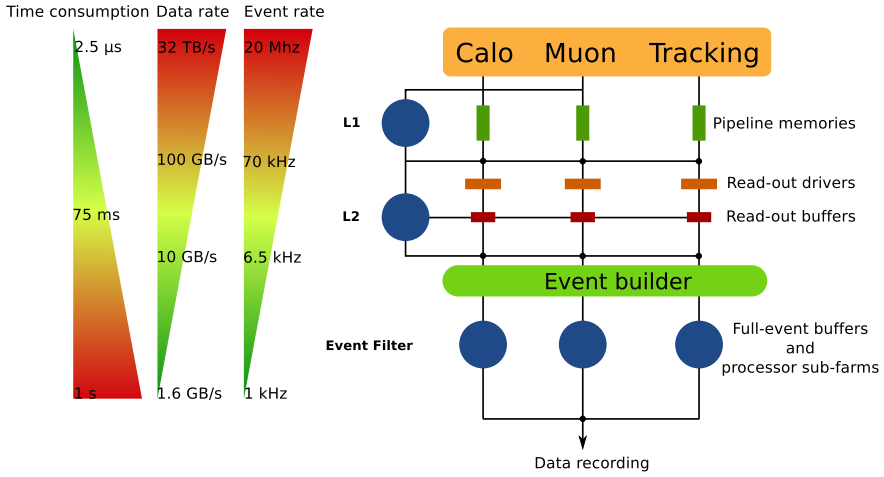

Figure 3.12: Schematic view of the three step ATLAS trigger system. Numbers are maximum values reached in 2012 data taking [91].

combination of several of those is exploited to make a decision about an event. At L1 a technique called prescaling is employed. To be able to achieve the former mentioned reduction while still preserving interesting low transverse momentum events, only a fraction $1/p$ of events passing a low threshold trigger are kept, where p is the so-called *prescale factor*. Another important task of the L1 system is to define a region of interest (RoI) which describes where in the detector (η,ϕ) an interesting event was recorded, of which nature (type of trigger fired) it was and which threshold was surpassed. This information is then passed on to the level 2 (L2) system.

The L2 trigger uses the RoI information of the L1 trigger to refine a trigger decision, while using the full granularity information and additionally the tracking information. This selection reduces the data rate from L1 down to 10 %. The full granularity is only available for the full detector, if the algorithm is less complex. If it is more complex than the trigger decision is obtained from detailed information available within a RoI only.

The last step in a trigger decision is called the Event Filter (EF), which reduces the data rate to 16 % of the output of L2. This is a total reduction from the detector output to the Event Filter output of $5 \cdot 10^{-5}$. The EF trigger uses the full detector coverage and granularity, which makes it possible to consider the full event for a trigger decision, instead of separated information from the sub-systems. Additionally the algorithms used in this last step are using calibrations that are as close to the ones used in the final analysis as possible.

The L1 system has to decide if an event is kept within 2.5 µs and is thus implemented close to the detector in ASIC (application-specific integrated circuits) or FPGA (field-programmable gate array) hardware. The decision in L2 has to be taken within 40 ms, while the EF decision is taken within 1 s, thus these two levels are implemented in computer farms with about 7500 CPU cores each.

The events passing the EF stage are then processed further in a so-called *reconstruction* step as shown in Sec. 3.2.6. Due to constraints on the computing power, the reconstruction is partly delayed to when the data taking is finished and hence the computing farm at L2 and EF could be used for delayed reconstruction. The rate of events reconstructed divided in categories depending on the objects triggered on is shown in Fig. 3.13. About 400 Hz have been reconstructed promptly, while additionally 200 Hz are reconstructed delayed.

Reconstruction

To obtain a data format that is analyzable by an end-user starting from the raw detector information, the multi-step procedure shown in Fig. 3.14 is implemented [93].

In a first step the data obtained from the Event Filter are stored in byte-stream (BS). This BS data is then transformed to a C++ representation, the so-called *raw data object* data (RDO).

These samples are then reconstructed into *event summary data* (ESD). This includes assigning 4-vectors to all particles exploiting the full momentum and rapidity range of ATLAS. For the

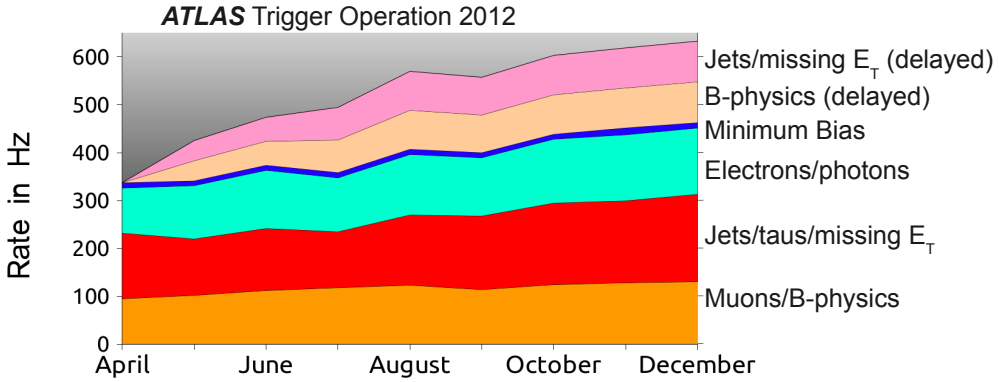

Figure 3.13: Rates recorded by the last step of trigger system in 2012 [92].

tracking all suitable detectors are used, which are the muon chambers, the drift tubes, the TRT and the silicon detectors. Here multiple pattern recognition algorithms are used.

From the calorimeter cell information clusters are formed and clusters are combined to jets (see Chap. 4).

In this step also the identification of objects like photons, electrons, positrons, muons and τ-leptons is performed. The reconstruction of jets and missing transverse momentum is refined here.

In a second step the ESD data are prepared for user analysis in the *analysis object data* (AOD) format. For this loose selection criteria are applied on the identified objects and object specific tags, for example b-tagging, are added. These tags are also available separately in the TAG format.

As those AOD files are still very large, a further step to reduce the level of detail, is performed. In this step *derived physics data* (DPD) are extracted [94]. This format exists in three levels of detail. The first two iterations D1PD and D2PD are AODs with reduced information tailored to physics analysis needs. To ease the handling of these files a third version D3PD was employed, which uses a flat structure of float numbers or vectors of floats. These samples are thus entirely interactively readable in ROOT [95]. These are even closer to the needs of a specific analysis group, by keeping only variables, objects and events, that are used in an analysis.

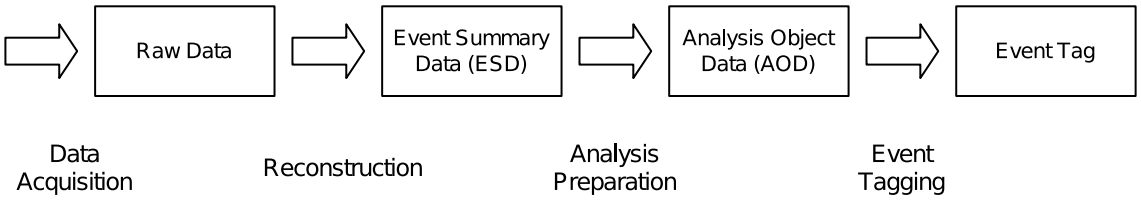

Figure 3.14: Reconstruction steps in ATLAS data model [93].

Luminosity

One important figure in particle physics is the luminosity (see [96] for an extensive summary). It is a measure for the performance of an accelerator and gives an estimate of the expected rate R seen for a process with cross-section σ:

$$\mathcal{L} = \frac{R}{\sigma} \tag{3.5}$$

Absolute Luminosity Determination

To obtain an absolute measurement of the luminosity several options are available. The most popular is the so-called *van der Meer* scan [97], which varies the separation of beams and calculates the convolved beam sizes Σ_i from such a measurement by calculating:

$$\Sigma_i = \frac{1}{\sqrt{2\pi}} \frac{\int R_i(\delta_i)\, d\delta_i}{R_i(0)} \tag{3.6}$$

For the two directions $i \in (x, y)$ and where δ_i is the transverse distance between the beams and $R_i(\delta_i)$ is the rate of events measured.

This can be transformed in a per bunch luminosity by:

$$\mathcal{L}_b = f_r \cdot n_1 \cdot n_2 \cdot \cos\alpha \cdot \frac{e^{-\frac{\Delta_x^2}{2\Sigma_x^2} - \frac{\Delta_y^2}{2\Sigma_y^2}}}{2\pi \cdot \Sigma_x \cdot \Sigma_y} \tag{3.7}$$

Where f_r is the revolution frequency of the accelerator, n_i are the number of protons per bunch, α is the crossing angle between the beams and Δ_i are the relative beam offsets.

Relative Luminosity Measurements

The results obtained in the former section can be used to determine absolute luminosity values for specific conditions. To measure the luminosity continuously different methods have been

developed. Those relative methods have to be calibrated regularly by the absolute methods, to obtain a reliable measurement.

Two methods to measure a relative luminosity are based on detectors which are placed close to the beam axis and thus measuring scattering under small angles. One detector is placed in the forward region and one in the backward. If hits in one or the other detector is observed in a bunch crossing, this crossing is counted in N_{OR}. If both detectors are hit this is counted in N_{AND}. The average number of visible inelastic interactions per bunch crossing μ_{vis} can be calculated as:

$$\mu_{vis} = -\ln(1 - \frac{N_{OR}}{N_{BC}}) \tag{3.8}$$

With the number of bunch crossings N_{BC}. To obtain the total number of inelastic collision $\mu = \mu_{vis}/\epsilon$, the efficiency ϵ is needed, which is process- and detector-specific.

If the efficiencies for the forward detector and the combination of both is similar and high enough, then the second method uses the coincidence of both detectors registering a particle as:

$$\mu_{vis} \approx -\ln(1 - \frac{N_{AND}}{N_{BC}}) \tag{3.9}$$

These two methods are usually referred to as *Event_OR* and *Event_AND*.

To calibrate the relative luminosity to the absolute scale the maximum interaction rate per bunch crossing has to be measured by one of the algorithms mentioned above. Thus the visible cross-section can be calculated as:

$$\sigma_{vis} = \mu_{vis}^{MAX} \frac{2\pi \cdot \Sigma_x \cdot \Sigma_y}{n_1 n_2} \tag{3.10}$$

Which is a characteristic number per algorithm and detector. This leads to the absolute luminosity of

$$\mathcal{L} = \frac{\mu_{vis} n_b f_r}{\sigma_{vis}} \tag{3.11}$$

Here n_b is the number of bunches in the accelerator.

Measurement in ATLAS

The luminosity measurement in ATLAS [98] is relying mainly on the results of two independent measurement methods performed with two detectors each.

At a distance of $z = 184\,\text{cm}$ from the interaction point the Beam Conditions Monitor (BCM) is situated [99]. The BCM consists of four diamond sensors on each side of the interaction

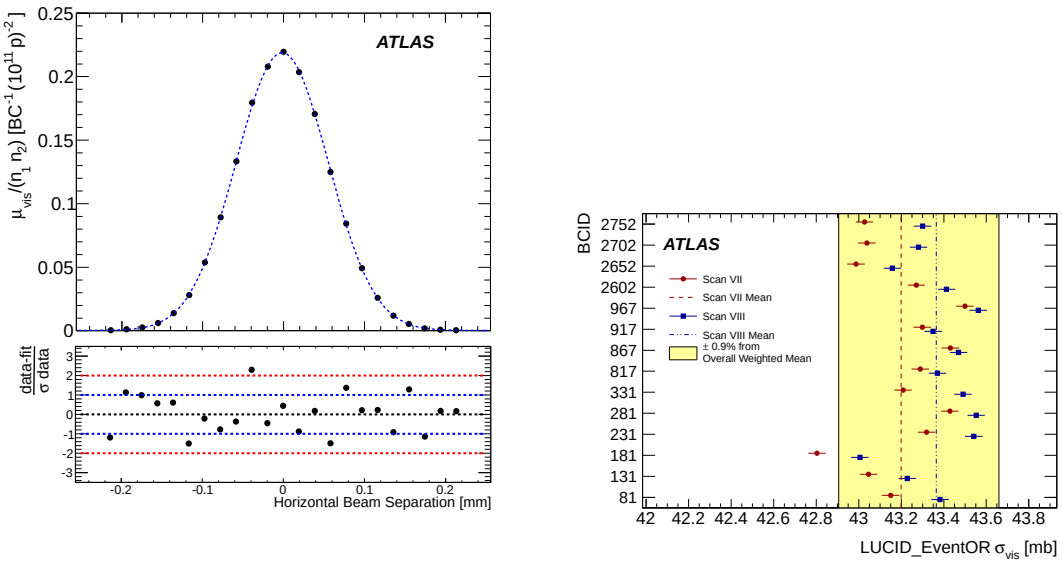

(a) Van der Meer

(b) Visible cross-section

Figure 3.15: Van der Meer scan recorded by BCMH using the Event_OR algorithm in 2011 (left). Extracted visible cross-section from LUCID in different scans in 2011 (right) [98].

point, with approximately 1 cm^2 in cross-section. The sensors are placed at a pseudo rapidity of $|\eta| = 4.2$ and can be grouped in two horizontal and two vertical sensors, named BCMV (vertical) and BCMH (horizontal).

The second detector used is LUCID [100], which is a Čerenkov-type detector with C_4F_{10} filled aluminum tubes. It is situated at a distance of 17 m from the interaction point which translates to $5.6 < |\eta| < 6.0$. Particles entering the tubes produce Čerenkov photons, which are internally reflected and guided to photomultiplier tubes. If more photons than given by a threshold are registered, this event is marked as a hit.

Both detectors use the Event_OR and Event_AND methods described in Sec. 3.2.7 to obtain a luminosity measurement.

An exemplary result of one van der Meer scan is shown in Fig. 3.15(a), recorded by the Event_OR algorithm by the BCMH detector part. The blue dotted line shows a fit to the data points by a Gaussian plus a constant term. The resulting visible cross-sections recorded by LUCID with the Event_OR algorithm are shown in Fig. 3.15(b).

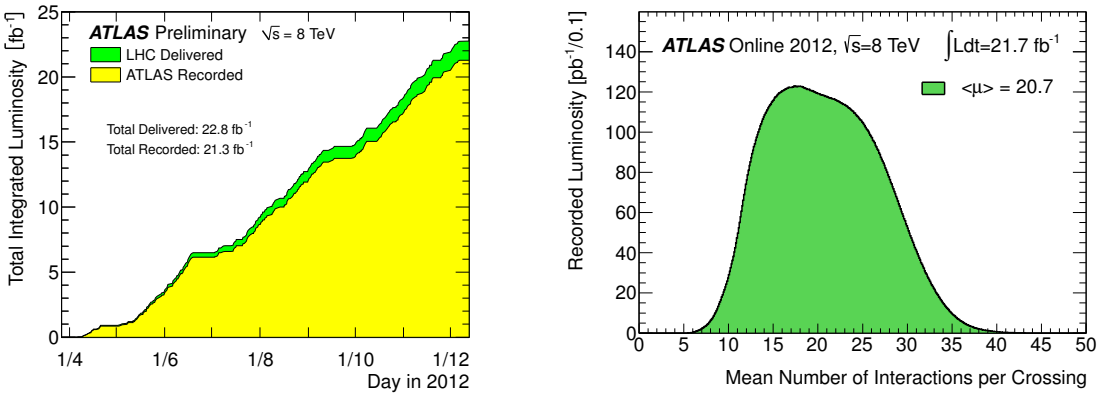

(a) Luminosity vs. time.

(b) Luminosity vs. $< \mu >$.

Figure 3.16: Integrated luminosity delivered from the LHC to ATLAS and luminosity successfully recorded by ATLAS [101] (left). Recorded luminosity as a function of average number of interactions per bunch crossing [101] (right).

To minimize systematic uncertainties the van der Meer scan has to be performed under special beam conditions, with a smaller number of colliding bunches and lower bunch intensities of the order of $\mathcal{L} = 1 \times 10^{29}\,\mathrm{cm}^{-2}\,\mathrm{s}^{-1}$.

The luminosity measurements for the data recorded in 2012 used the same methodology as explained in [98]. The total integrated luminosity over time is shown in Fig. 3.16(a). A total of $22.8\,\mathrm{fb}^{-1}$ have been delivered by the LHC, while the detector recorded $21.3\,\mathrm{fb}^{-1}$ of which $20.3\,\mathrm{fb}^{-1}$ have been found to be usable for physics analysis. The measurements of the luminosity are given with an uncertainty of 2.8 %, which take into account multiple sources of uncertainties. The largest uncertainties are assigned to the calibration of the van der Meer scan, smaller uncertainties are accounted for the long-term stability, the dependence on μ, the bunch population product, the stability of BCM and afterglow corrections. Where the afterglow takes into account, that due to nuclear de-excitations in bunch crossings after a collision, a remaining activity is measured by the luminosity detectors.

The average number of interactions per crossing is obtained by solving Eqn. 3.11 for μ and using the per bunch luminosity measured above. The result for the 2012 data taking is shown in Fig. 3.16(b).

4 JETS

As quarks and gluons hadronize within a short distance, they cannot be observed as partons in the detector. A good approximation to reconstruct the kinematic properties of the outgoing partons produced in a collision, are jets. These are a combination of several objects depending on their properties. In ATLAS jets are constructed from topological calorimeter clusters. In this section the full chain from initial cell energies to fully calibrated jets is discussed. In Sec. 4.1 the clustering of calorimeter cells to topological clusters is shown. The clustering of topological clusters to jets is discussed in Sec. 4.2. In Sec. 4.3 the rejection of jets that are not originating from the hard scatter and the treatment of jets in poorly instrumented regions is discussed. The calibration procedure used in ATLAS to obtain the correct energies for these jets is outlined in Sec. 4.4. The method to obtain systematic uncertainty on the estimation of the jet energy is summarized in Sec. 4.5. Finally the jet energy resolution is discussed in Sec. 4.6. The full procedure from calorimeter cells to fully calibrated jets, which is detailed in this chapter, is shown in Fig. 4.1. The following sections are summarizing the efforts made by the ATLAS community, and do not include own contributions of the author.

TOPOLOGICAL CLUSTERS FROM CALORIMETERS CELLS

To reconstruct the energy of a particle in the calorimeter a sophisticated algorithm to cluster cells is mandatory. This procedure has to be able to suppress noise from the electronics and from multiple proton-proton collisions, as well as separate the energy deposits from close-by particles. Due to the nature of the calorimeter system in ATLAS it also has to cope with very different

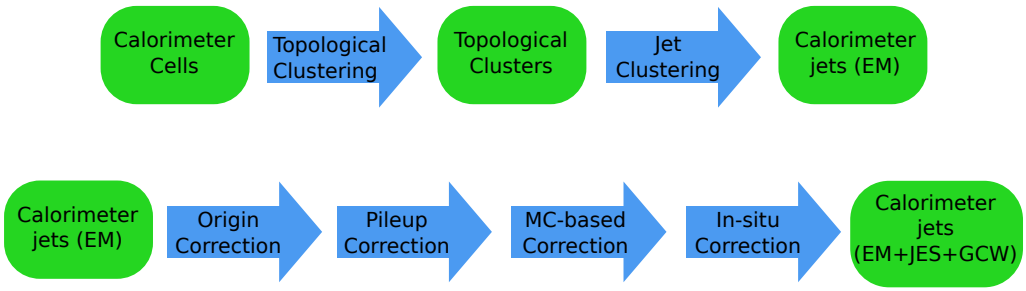

Figure 4.1: Steps from calorimeter cells to fully calibrated jets in EM+JES+GCW scheme.

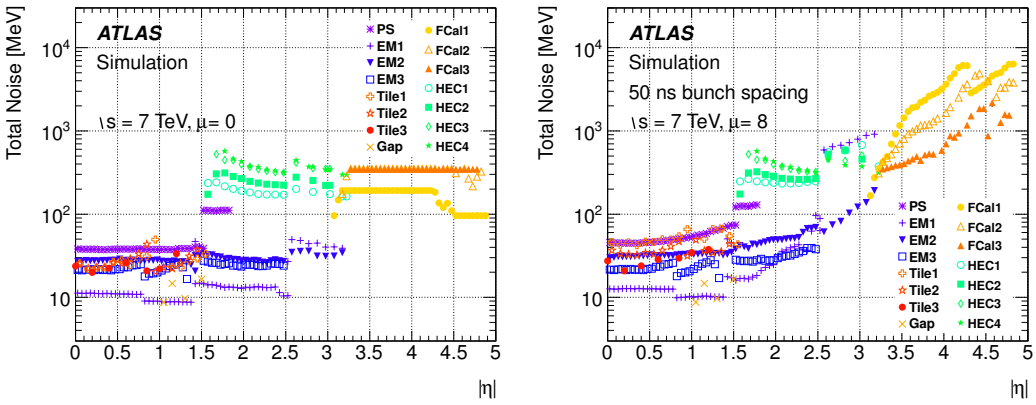

(a) At $L = 0$ **(b)** At $L = 1 \times 10^{34}\,\mathrm{cm}^{-2}\,\mathrm{s}^{-1}$

Figure 4.2: Noise at cell level in different calorimeter components [102] simulated for a center of mass energy of $\sqrt{s} = 7\,\mathrm{TeV}$.

granularities and detector geometries. All of these requirements are met by the topological cluster algorithm [102].

A topological cluster consists of a number of adjacent calorimeter cells that are selected according to a given algorithm. The criteria to select cells in ATLAS is based on the signal-over-noise ratio t. The signal strength is the absolute value of the energy in a calorimeter cell. The noise per cell is calculated as the expected electronic noise added in quadrature with the expected noise from pileup events. The contribution of electronic noise for $\sqrt{s} = 7\,\mathrm{TeV}$ in different calorimeter types and rapidity regions is shown in Fig. 4.2(a). In the rapidity region used in this analysis, the electronic noise is always below 500 MeV per cell. The effect of additional noise from pileup events is shown in Fig. 4.2(b) for pileup conditions similar to the ones in the $\sqrt{s} = 7\,\mathrm{TeV}$ data taking, where a luminosity of $L = 1 \times 10^{34}\,\mathrm{cm}^{-2}\,\mathrm{s}^{-1}$ and an average number of interactions per bunch crossing $\langle\mu\rangle = 8$ increases the noise level in the region of interest up to 2 GeV. For the conditions of the 2012 data taking at $\sqrt{s} = 8\,\mathrm{TeV}$ and $\langle\mu\rangle = 30$ those noise levels are increased by a factor of 2. The clustering then follows these steps:

1. Select all cells with $t > t_{seed}$ as seeds for the clustering. Those seeds are now called proto-clusters. Sort the list of proto-clusters in descending order according to the energy per cell.

2. Add all adjacent cells to the initial seed that fulfill $t > t_{neighbor}$. All cells added act as an additional seed. Repeat this step until the proto-cluster stops growing.

3. Iterate again through the list of the now larger proto-clusters. Add all adjacent cells to the proto-cluster if $t > t_{cell}$.

If during this procedure a cell is adjacent to two clusters then there are two possibilities. If $t > t_{neighbor}$, then the two proto-clusters are merged. If $t < t_{neighbor}$, then the cell is merged with the more energetic proto-cluster.

It was shown, that in ATLAS a scheme with $t_{seed} = 4$, $t_{neighbor} = 2$ and $t_{cell} = 0$ works best to suppress noise while efficiently finding low-energy clusters.

After these clustering steps there might be large clusters which are produced by more than one particle. To recover as much information as possible, several steps are followed to split clusters. For this procedure only cells that have been part of a proto-cluster are considered:

1. Find a cell that is a local maximum with $E_{cell} > 500\,\text{MeV}$ and has at least 4 neighboring cells.

2. Use local maxima as seeds for clustering:

   - This clustering does not obey any thresholds.
   - Only cells that have been in a proto-cluster are considered.
   - No merging of proto-clusters is performed.

If after the last step a cell adjoins two proto-clusters, the cell is shared between the two and the proto-clusters get a fraction of the cells energy assigned. This fraction of energy is determined by the following weight:

$$w^{geo}_{all,1} = \frac{E^{EM}_{clus,1}}{E^{EM}_{clus,1} + r \cdot E^{EM}_{clus,2}} \qquad w^{geo}_{all,2} = 1 - w^{geo}_{all,1} \tag{4.1}$$

Here $w^{geo}_{all,i}$ is the weight assigned to the cell with respect to proto-cluster i and $E^{EM}_{clus,i}$ is the energy of proto-cluster i. The weight depends on the relative energy of the two proto-clusters considered, and a geometrical factor r :

$$r = e^{d_1 - d_2} \tag{4.2}$$

With d_i, the distance of the cell to the geometric center of proto-cluster i. This factor r is unity if the distances d_i are equal. In this case the energy of the cell is assigned to proto-cluster 1 and proto-cluster 2 according to the energy of the proto-clusters. For equal energies, the cell is assigned to both proto-clusters equally. For the case that the cell is closer to one proto-cluster, this cluster will receive a larger fraction of the cell energy.

After merging and splitting all proto-clusters with negative energy are removed, and the remaining ones are called clusters. To obtain the cluster kinematics (η_{clus}, ϕ_{clus}), the already introduced geometrical weights are used, to estimate a weighted sum:

$$\eta_{clus} = \frac{\sum_{i=1}^{N_{cell}} w_{all,i}^{geo} \cdot \left|E_{cell,i}^{EM}\right| \cdot \eta_{cell,i}}{\sum_{i=1}^{N_{cell}} w_{all,i}^{geo} \cdot \left|E_{cell,i}^{EM}\right|} \tag{4.3}$$

$$\phi_{clus} = \frac{\sum_{i=1}^{N_{cell}} w_{all,i}^{geo} \cdot \left|E_{cell,i}^{EM}\right| \cdot \phi_{cell,i}}{\sum_{i=1}^{N_{cell}} w_{all,i}^{geo} \cdot \left|E_{cell,i}^{EM}\right|} \tag{4.4}$$

The total energy of a cluster E_{clus}^{EM} is calculate as:

$$E_{clus}^{EM} = \sum_{i=1}^{N_{cell}} w_{all,i}^{geo} \cdot E_{cell,i}^{EM} \tag{4.5}$$

To assign a mass to a cluster a hypothesis about the particle measured in the cluster would be needed. To avoid additional assumptions, clusters are considered as massless pseudo-particles, with a four-momentum:

$$\mathbf{P} = E_{clus}^{EM} \cdot (1, \sin\theta_{clus} \cdot \cos\phi_{clus}, \sin\theta_{clus} \cdot \sin\phi_{clus}, \cos\theta_{clus}) \tag{4.6}$$

Here θ_{clus} is calculated from the pseudo-rapidity as $\theta_{clus} = 2 \arctan e^{-\eta_{clus}}$

JET CLUSTERING ALGORITHMS

The clustering method shown in Sec. 4.1 performs well in clustering all remnants from pion decays in up to 10 cluster. To reconstruct the initial parton, all hadronization products have to be clustered. For this a more sophisticated method is necessary. The presented algorithm [103] can be used with input pseudo-particles at various levels. Here topological clusters are used as an input, which are clustered to represent the spray of particles originating from the hadronization of a single parton.

To give a representation of the underlying physics and be able to compare data with theoretical calculations, the resulting jets have to fulfill two requirements:

- Infrared safety: Any additional soft radiation must not change the properties of the jet

- Collinear safety: Splitting of a hard pseudo-particle in two softer collinear particles must not change the properties of the jet

Those two properties are important to give a reliable result independent of details of the hadronization, that might introduce additional splitting of final state particles. Also additional particles originating from soft radiations or pileup should not influence the jet.

Several algorithms to cluster jets have been developed and used in the past. The algorithm used for this analysis is called *anti*-k_t. It uses a sequential procedure for clustering, depending on the distance $\Delta_{ij} = \sqrt{(y_i - y_j)^2 + (\phi_i - \phi_j)^2}$ between pseudo-particles i and j, as well as the transverse momenta $p_{t,i}$ and $p_{t,i}$.

1. Calculate the distance measure between particle i and all other possible particles j as:

$$d_{i,j} = \min\left(p_{t,i}^{2p}, p_{t,j}^{2p}\right)\frac{\Delta_{ij}^2}{R^2} \tag{4.7}$$

2. Calculate the distance measure between particle i and the beam as:

$$d_{i,B} = p_{t,i}^{2p} \tag{4.8}$$

3. Combine pseudo-particles i and j if there is one $d_{i,j}$ that is smaller than $d_{i,B}$. If all $d_{i,j}$ are larger than $d_{i,B}$, remove object i from the list of particles and call it a jet.

4. Repeat the above procedure until the list of pseudo-particles is empty and all jets are found.

Different values of p change the behavior of the clustering fundamentally. For $p = 1$ the algorithm is called the k_t-algorithm, which clusters particles with small transverse momentum first. This leads to jets of irregular shape, which makes it hard to subtract contributions from additional interactions.

The algorithm is called Cambridge/Aachen for $p = 0$, here the clustering is independent from kinematical properties of the particles and takes only the geometrical distance into account. This also gives an irregular shape, which is dependent on soft radiation.

The algorithm used in this analysis is called anti-k_t using $p = -1$. The variable R gives a measure of the size of the resulting jet. For a scenario with some hard particles and several soft particles, there are three different cases. If no hard particle is found within a distance of $2R$ around a hard particle, then a perfectly conical jet is produced with a radius of $r = R$. If a second hard particle is found in a distance Δ_{ij} between R and $2R$, then two jets are produced. Soft particles in the overlapping region between the two hard jets are assigned to one or the other jet depending on the distance and transverse momentum configuration. If a second hard particle is found within R of the first hard particle, then both are clustered in the same jet, which shape differs from a cone, depending on the transverse momenta.

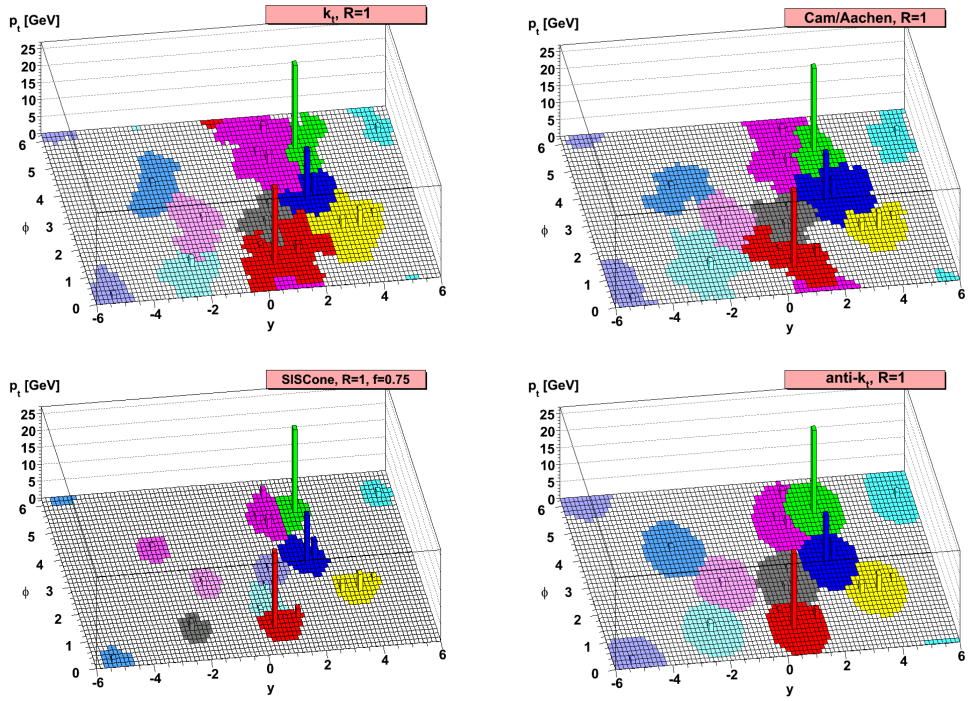

Figure 4.3: Active area for different jet algorithms [103].

To illustrate different jet algorithms the active area of a jet was defined [104]. To calculate the active area of a jet, a large amount of very soft particles is added to an event. Those so-called *ghost-particles* are taking part in the usual clustering. In Fig. 4.3 this active area is illustrated as colored area, for different jet algorithms. One can easily see, that jets clustered with the anti-k_t algorithm tend to give conical jets centered around the highest p_T particle, as expected.

JET QUALITY CRITERIA

When working with jets from topoclusters, there are two types of jets that should be excluded. One type of reconstructed jets originates from sources different than the hard scatter e.g. cosmic radiation. In Sec. 4.3.1 the methods to identify such jets is shown, and the criteria to remove them from data are discussed. The second type of jets that should be ignored in data analysis, are those jets with a poorly measured energy. This is the case if a jets direction coincides with a non-functional part of the detector, or a transition region with non-optimal instrumentation. In Sec. 4.3.2 the impact of these jets and the selection criteria to exclude these is shown. The following sections outline the work presented in detail in [105].

Jets from Other Sources

Partons produced in an hard scatter event will eventually be measured in the calorimeter and will be reconstructed as a jet. Apart from those jets, that a physics analysis is interested in, there are several other sources of jets:

- Beam-gas events: If a proton collides with the residual gas in the beam-pipe, this can lead to a collimated bunch of particles and be misinterpreted as jet.
- Beam-halo events: If the halo of the beam interacts with the collimators in the accelerator, sprays of particles are produced, that can reach the detector.
- Cosmic rays: If a cosmic ray gets measured in the detector, while a proton-proton collision occurs, this can be misinterpreted as originating from the hard scatter.
- Calorimeter noise: Electronic noise in the calorimeter can be reconstructed as a jet.

The solution is to find a suitable set of selection criteria to reject jets that are not originating from the hard scatter, while retaining jets that are from the hard scatter. This is performed on data and MC simulation, by selecting two samples. One sample that is enriched with non-collision jets by selecting events with only one jet and a large missing transverse momentum E_T^{miss}. Also the direction of the jet and the E_T^{miss} should be in opposite direction in the plane transversal to the beam axis by selecting $\Delta\Phi(\text{jet}, E_T^{miss}) > 2.8\,\text{rad}$. Additionally the missing transverse momentum significance $E_T^{miss}/\sqrt{\sum E_T}$ needs to be larger than $3\,\text{GeV}^{1/2}$. The second sample is selected to be originating from the hard scatter and two jets are selected that are back-to-back, by selecting $\Delta\Phi(\text{jet},\text{jet}) > 2.8\,\text{rad}$. The E_T^{miss} significance has to be lower than $2\,\text{GeV}^{1/2}$.

Selection Criteria

To suppress the effect of jets originating from other sources than the hard scatter, a variety of variables can be used. To handle jets originating from calorimeter noise the jet quality is used, which is defined as:

$$Q_{\text{cell}}^{\text{LAr}} = \sum_{j=1}^{5} \left(s_j - A g_j^{\text{phys}} \right)^2 \tag{4.9}$$

This quantity compares the expected pulse shape from an ionization event, with shape g_j^{phys} normalized to unity and measured amplitude A, with the measured pulse shape s_j. This comparison is performed for the five sampling points used in the energy calculation.

A quantity that is useful for jets is the normalized average quality factor $\langle Q \rangle$, which is the energy squared weighted quality factor for all cells within a jet. Also useful is the differentiation

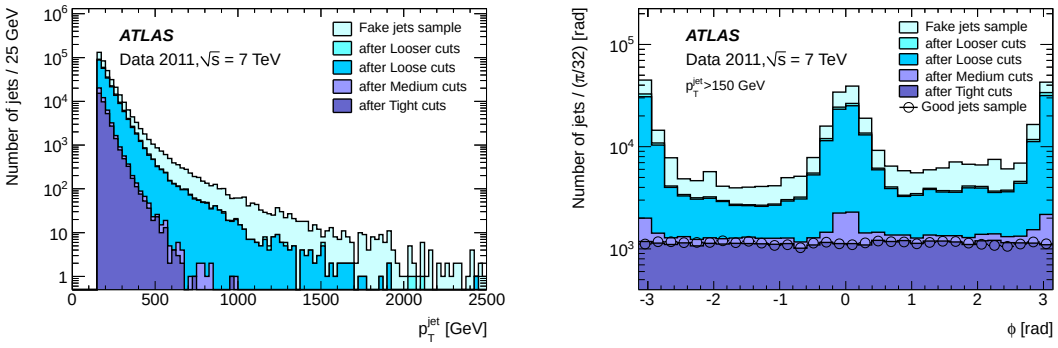

(a) p_T dependence

(b) ϕ dependence

Figure 4.4: Jet distributions for different selection levels in data recorded at $\sqrt{s} = 7\,\text{TeV}$, the impact of the center of mass energy change on the cleaning is negligible. Shown is the impact of fake jet selection and hard scatter selection [105].

between calorimeter regions, for this the fraction of energy in a calorimeter region f_Q^{LAr} or f_Q^{HEC} with a poor quality factor ($Q_{cell}^{LAr} > 4000$) is calculated.

A selection according to these three variables is able to reject the two main components of calorimeter noise. One source are noise bursts which occur in the hadronic end cap calorimeter, and manifest itself as single cells with a large fraction of a jets energy, while also having large $\langle Q \rangle$. Another source is coherent noise in the electromagnetic calorimeter, which is characterized by large fractions of a jets energy in this part of the calorimeter, while having a large $\langle Q \rangle$ and large f_Q^{LAr}.

To select jets originating from cosmic rays or beam-induced backgrounds, useful variables are sensitive to the shapes of the electromagnetic shower, as the fraction of energy in the electromagnetic calorimeter f_{EM} or the layer with the maximum energy fraction f_{max}. As jets are usually also measured by tracks, which are produced by charged particles, the fraction of transverse momentum calculated from tracks relative to the jets calorimeter transverse momentum f_{ch} is used.

Another useful variable is the jet time, which is the squared energy weighted cell time. Where the cell time is the time between collision and impact of a particle in a calorimeter cell.

In [105] four different levels of jet cleaning have been defined. The levels are called *looser*, *loose*, *medium* and *tight* with decreasing contribution of fake jets in the selection. The levels *looser* and *loose* are defined to be almost 100 % efficient in keeping hard scatter events, while rejecting 99.5 % of fake jets. In Tab. A.1 and Tab. A.2 the selection criteria for those levels are summarized.

In Fig. 4.4(a) the impact of these selections is shown for the transverse momentum of a jet. Fig. 4.4(b) shows the same for the ϕ distribution. This distribution shows clearly the additional contribution at $\phi = 0$ and $\phi = \pi$, which is characteristic for beam-induced backgrounds, originating from the collimators of the LHC.

Selection Efficiency

A tag and probe method is used to estimate the efficiency of these selection criteria. By selecting dijet events in which the tag jet has to pass tight selection criteria, the probe jet can be assumed to be from the hard scatter event. Thus applying the selection criteria on this probe jet, gives an estimate on the efficiency of the selection. The measured selection efficiency is above 99.8 % for the *looser* level for $p_T > 30\,\text{GeV}$ and $|\eta| < 4.5$, and only slightly worse for the *loose* selection. For the other levels jets with a transverse momentum of $p_T < 50\,\text{GeV}$, have a selection inefficiency of up to 15 %, while for higher transverse momenta the efficiencies are above 99 % for *medium* and above 98 % for *tight*.

Inaccurate Measured Jets

During the operation of ATLAS some modules of the Tile Calorimeter were not operational. If a fraction of particles in a jet hits these modules, then the reconstructed jet energy estimate is inaccurate. To correct for this, two methods are used. On a cell level the average of two working cells can be used, to estimate the energy lost to the measurement. The second option is to estimate the jet shape based on MC simulations depending on the exact position in the calorimeter. The effect of non-working modules is estimated as:

$$\text{BCH}_{\text{cor,jet}} = \frac{1}{E_{\text{jet}}} \sum_{i \in \text{bad cells}} E_{\text{cell,i}} \tag{4.10}$$

With the total energy per jet E_{jet} and the energy per cell $E_{\text{cell,i}}$ where i denotes the cell. The jet energy is thus corrected as:

$$E_{\text{jet}} = \frac{E_{\text{jet,uncorr}}}{1 - \text{BCH}_{\text{cor,jet}}} \tag{4.11}$$

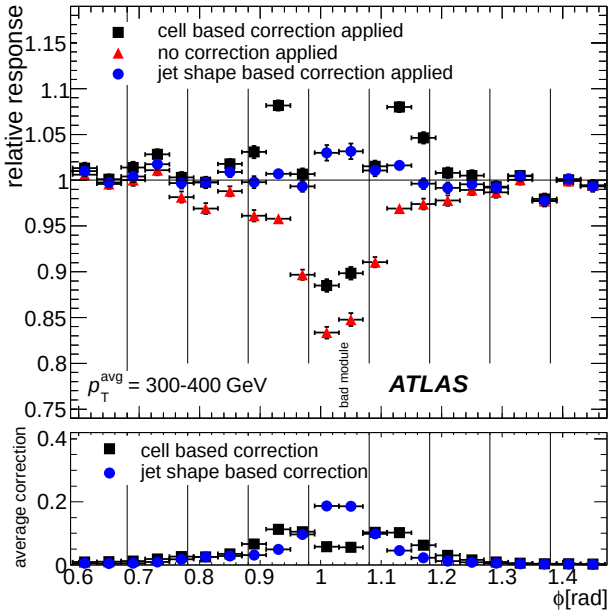

Figure 4.5: Relative response of probe jet in region with non-functional tile module [106] measure in data recorded at $\sqrt{s} = 7$ TeV. The impact in $\sqrt{s} = 8$ TeV is similar.

In Fig. 4.5 the response of jets corrected with these two methods is shown, studied via tag-and-probe. The jet based correction performs better than the cell based, thus the jet level correction is used. This correction performs well if small fractions of a jet are affected. If large fractions of a jet are within non-operational regions of the detector, the jet energy cannot be calculated reliably, thus jets with a correction bigger than 50 % are flagged as *ugly*.

As there is a transition region between barrel and end cap calorimeters, which is not instrumented well for measuring jets, any jets falling in this region are also excluded from the analyses. These events are selected by using the energy fraction in the TileGap3 scintillator, which separates these two detector regions. If the energy fraction of a jet measured in this scintillator exceeds 50 %, the jet is flagged as *ugly*.

JET CALIBRATION

The jets found according to the procedure in Sec. 4.2 give only a rough estimate of the energy of the parton they originated from. The calibration of the calorimeters are designed to measure energies of particles interacting mainly electromagnetically like electrons or photons, and thus producing electromagnetic showers. A jet consists mainly of pions. Neutral pions dominantly decay to two photons, while charged pions decay to a muon and a neutrino. The neutrinos

produced in these decays usually pass through the detector without detection, and are thus lost for the determination of the energy (effect of $\mathcal{O}(1\,\%)$). A much larger fraction of energy of up to 50−60 % is not visible to the detector due to inelastic collisions between particles from the shower and the detector material. Those collisions produce low-energy photons or nuclear fragments which travel only a small distance and are lost in the absorber part of the calorimeter.

To assign the correct energy to a jet, additional calibration steps are necessary. In Fig. 4.1 the full chain of calibration is shown. The first row corresponds to the procedure discussed in Sec. 4.1 and Sec. 4.2, which produces calorimeter jets from calorimeter cells via clustering to topological clusters. The second row shows the four additional corrections applied to recover the energy lost in the measurement. The full calibration procedure as used for $\sqrt{s} = 7\,\text{TeV}$ is presented in [106]. For the data recorded at $\sqrt{s} = 8\,\text{TeV}$ the order of corrections has been altered, the pileup correction has been improved [107] and an additional step in the MC-based correction has been added [108].

Origin Correction

As shown in Eqn. 4.6, the kinematic variables assigned to a cluster are dependent on the individual cell variables. Given that a jets kinematic variables are calculated as the sum of four-vectors of the corresponding topological clusters, it is important that the spatial coordinates of cells are calculated correctly. The spatial coordinates have been calculated with respect to an origin, which is set to be the detector center. As the position of the hard scatter interaction point can be different from the detector center, a correction is needed. As the displacement is along the z-axis of the detector, the pseudo-rapidity η is influenced, while ϕ is unaffected. A correction to the pseudo-rapidity is applied to topological clusters. The vector pointing from the origin to the centroid of the cluster is adapted to originate in the real hard scatter vertex. This correction is then propagated to the jet level. The correction improves the angular resolution and the jet p_T response by up to 1 %.

Pileup Correction

Pileup impacts a jet measurement in two ways. On the one hand particles originating from pileup vertices can end up in jets assigned to the hard scatter process. This has an effect on the energy of the jet. On the other hand jets originating from pileup vertices can be reconstructed and thus lead to additional jets in an event. The latter can be corrected for by using a tagger [109] to identify those jets, and remove them from the analysis. To correct for the former effect a two step procedure is applied. In a first step the jet energy is corrected for pileup on an event-by-event basis depending on the jet area and median p_T density (which is a measure of pileup activity). In a second step any residual pileup dependence is removed in a MC based

approach, where the response is binned in number of primary vertices N_{PV} and average number of interactions per bunch crossing $\langle\mu\rangle$.

These two variables are sensitive to the two origins of pile up. Additional interactions in the proton-proton collision can occur and show up as supplementary vertices. This kind of pile up is called *in time pileup*, and can be characterized by the number of primary vertices N_{PV}.

The second type of pile up is the so-called *out of time pileup*, which occurs when particles emerging from a previous collision are detected in a later collision. This kind of pileup is influenced by the average number of interactions per bunch crossing $\langle\mu\rangle$.

Jet Area Based Subtraction

The jet area method uses the area covered by a jet and the measured p_T density from pileup to correct the jet energy. The property used to estimate the pileup contribution is the median of the p_T density as defined by:

$$\rho = \text{median}\left\{\frac{p_{T,i}^{jet}}{A_{t,i}^{jet}}\right\} \tag{4.12}$$

Here ρ is calculated by clustering the topological clusters for each event with the k_t-algorithm. The transverse momentum of jet i clustered in this way is $p_{T,i}^{jet}$, while $A_{t,i}^{jet}$ is the transverse component of the four-vector of the jet area A_i^ν. The four-vector version of the jet area is defined as an extension to the area introduced in [104]:

$$A_j^\nu = \frac{1}{\nu_g \langle g_t\rangle} \sum_{g_i^\nu \in j} g_i^\nu \tag{4.13}$$

To estimate the area of a jet, a large amount of ghost particles with very small p_T is added uniformly to an event. The four momentum of a ghost particle g_i^ν is summed for all particles within a jet j. Additionally this sum is normalized by the transverse momentum density of the ghost particles $\nu_g \langle g_t\rangle$, where ν_g is the number of ghost particles per unit area.

The resulting ρ distribution is shown exemplarily for $20 \leqslant \langle\mu\rangle < 21$ and different values of N_{PV} in Fig. 4.6(a). Here a calibration scheme different from the one used in this work is shown. The so-called *local calibration weights* (LCW) method accounts for the non-compensating nature of hadronic interaction by weighting at cell level. The plots shown here are similar for both schemes. For a fixed $\langle\mu\rangle$ the number of primary vertices is clearly correlated to the measured event p_T density. The dependence of $\langle\rho\rangle$ as a function of pseudo-rapidity η for different values of $\langle\mu\rangle$ is shown in Fig. 4.6(b). For the region with $|\eta| < 2.5$, where the granularity of the calorimeter is large, a large $\langle\rho\rangle$ is observed, which is decreasing with decreasing $\langle\mu\rangle$.

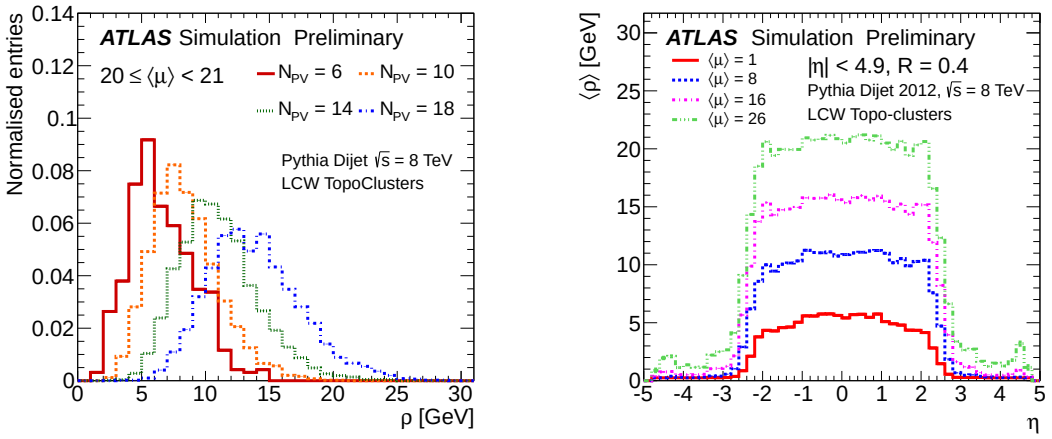

(a) Different N_{PV} for $20 \leqslant \langle\mu\rangle < 21$.

(b) Different values of $\langle\mu_{avg}\rangle$.

Figure 4.6: Dependence of median event p_T density for different pileup conditions [107].

The corrected transverse momentum of a jet is finally calculated as:

$$p_T^{jet,corr} = p_T^{jet} - \rho \cdot A_T \tag{4.14}$$

Where p_T^{jet} is the transverse momentum of the jet after origin correction, ρ the event p_T density and A_T the transverse component of the jet area.

Residual Pileup Correction

After subtracting the pileup component according to $\rho \cdot A_T$ there is still a residual dependence of the reconstructed p_T on N_{PV} and $\langle\mu\rangle$ as shown in Fig. 4.7. The notable change of behavior around $|\eta| = 2.5$ is because of the different granularities of the forward calorimeter, which starts there. The pileup subtraction removes the dependency on in-time pileup almost completely as shown in Fig. 4.7(a). The dependence on out-of-time pileup is not changed as shown in Fig. 4.7(b). To remove the remaining pileup dependence a correction is applied which is calculated from simulated dijet events. By comparison to jets clustered from truth particles, a correction proportional to $N_{PV} - 1$ and $\langle\mu\rangle$ is obtained. This correction improves the performance with in-time pileup further, while greatly decreasing the out-of-time pileup effect.

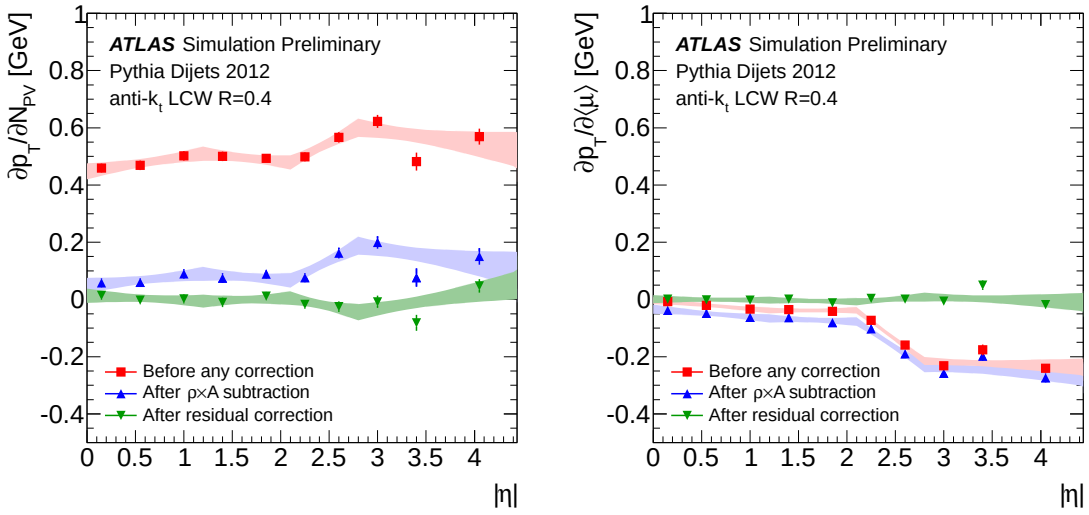

(a) Dependence on N_{PV}.

(b) Dependence on $\langle\mu\rangle$.

Figure 4.7: Dependence of p_T on pileup variables for different stages of the pileup correction [107]. The bands shown give the statistical uncertainty from the fit.

MC-Based Jet Energy Scale

To obtain the true jet energy, an additional correction is applied which uses simulated data. As the pileup dependence is already subtracted, this MC sample is produced without additional pileup effects. The correction uses jets at truth level that are geometrically assigned to reconstructed jets, that are within $\Delta R = \sqrt{(\Delta\eta)^2 + (\Delta\phi)^2} = 0.3$, where $\Delta\eta$ and $\Delta\phi$ are the differences in spatial dimensions between truth and reconstructed jet. Also the jets at both levels have to be isolated, so that within a distance of $\Delta R = 2.5\,R$ no jet at the same level is found with a transverse momentum of $p_T > 7\,\text{GeV}$. These jets are divided in bins of truth energy E^{jet}_{truth} and pseudo rapidity at detector level η_{det}. For each $(E^{jet}_{truth}, \eta_{det})$-bin the jet energy response $\mathcal{R}^{jet}_{EM} = \frac{E^{jet}_{EM}}{E^{jet}_{truth}}$ is calculated and the mean is found by fitting a Gaussian distribution to $\mathcal{R}^{jet}_{EM}$. In the same bins the mean of E^{jet}_{EM} is calculated. Those values are then fitted for each bin, with a function according to:

$$\mathcal{F}_{calib,k}(E^{jet}_{EM}) = \sum_{i=0}^{N_{max}} a_i \left(\ln E^{jet}_{EM}\right)^i \tag{4.15}$$

Here a_i are free parameters in the fit, and N_{max} is chosen according to the fit quality.

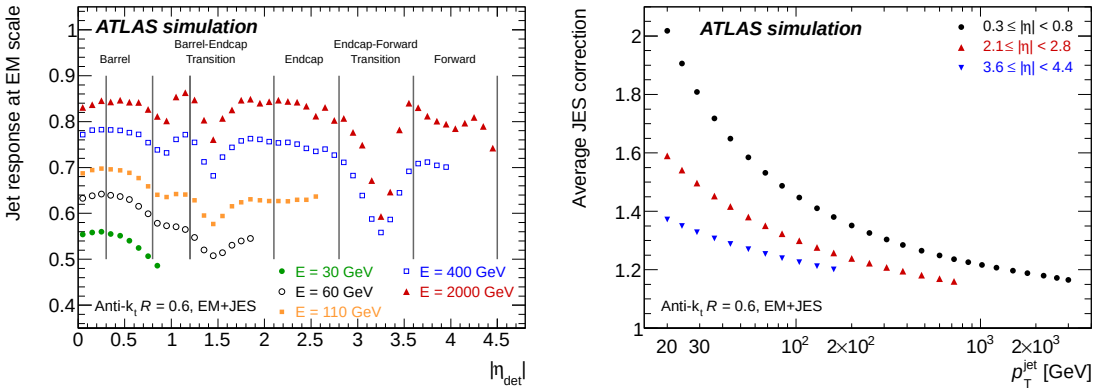

(a) Dependence on $|\eta_{det}|$

(b) Dependence on p_T^{jet}

Figure 4.8: Jet response (left) and average JES correction (right) in simulated data as a function of $|\eta_{det}|$ for different jet energies for a center of mass energy of $\sqrt{s} = 7\,\text{TeV}$ [110].

The final jet energy correction factor is then calculated as

$$E^{jet}_{EM+JES} = \frac{E^{jet}_{EM}}{\mathcal{F}_{calib,k}(E^{jet}_{EM})|_{\eta_{det}}} \tag{4.16}$$

and the effect on p_T for different detector regions can be seen in Fig. 4.8(b) for a center of mass energy of $\sqrt{s} = 7\,\text{TeV}$. The inverse correction as a function of absolute pseudo-rapidity for different jet energies is shown in Fig. 4.8(a). As the description of the detector has been improved, by for example a better description of the inactive material or dead material in the simulation, the jet responses have changed slightly in the low energy bins. As not enough dead material was included, the jet response in this old description was too large, in the 2012 simulated data, the response for the lowest energies is up to 10 % lower than shown here. In addition the response for large pseudo-rapidities of $|\eta_{det}| > 3.0$ also decreased by up to 10 % due to a change in the calibration constants in the FCAL region which compensates for pileup and noise effects.

Global Sequential Calibration

The last step of the MC-based calibration uses calorimeter, tracking and muon chamber information to improve the energy resolution [108]. By characterizing fluctuations in the particle content of shower developments, the sensitivity to jet flavors is decreased.

The calibration used keeps the mean jet energy from the previous calibration steps unchanged, while improving the resolution of the jet energy. The corrections C are applied in bins of (p_T^{jet}, x)

denoted as j, where x is a variable found to be useful in improving the resolution or to reduce the flavor dependency, as:

$$C = \frac{p_T^{truth}}{p_T^{jet}} \tag{4.17}$$

Where the correction is calculated for every bin j and every variable x.

The correction is applied sequentially to the calibrated p_T^{i-1} of the former calibration step, for each variable x, to obtain the calibrated momentum after step i, p_T^i.

Variables used to calibrate are exploiting the fact, that energy in a specific layer gives a hint to the response to expect. As the response is lowered due to the non-compensating nature of the calorimeter. Other variables are sensitive to the composition of a jet, which is sensitive to the initial parton (light-quark or gluon).

The variables used are the fraction of energy per layer, to quantify where energy is deposited in the calorimeter. Also the number of tracks as well as the jet width are used to characterize the jets content. The jet width is defined as:

$$\text{width}_{trk} = \frac{\sum_i p_T^i \Delta R(i, jet)}{\sum_i p_T^i} \tag{4.18}$$

Here i denotes the tracks and $\Delta R(i, jet)$ is the spatial distance between track and jet.

This method is also used to recover energy of so-called *punch through*. If the particles of a jet are not contained in the electromagnetic and hadronic calorimeter, the jets energy reconstructed from using the calorimeter information only is underestimated. A correction based on the activity in the muon chamber behind a jet is used to correct for this lowered calorimeter response.

For the punch through correction a different definition of the response in Eqn. 4.17 is used, which uses energies instead of transverse momenta, as the energy was found to have higher sensitivity to the effect studied.

In Situ Calibration

The final step in the calibration uses so-called *in situ* techniques to correct the jet transverse momentum by exploiting balancing particles in data. Particles that are well measured are used in a tag and probe method, to correct the energy of a recoiling jet. Several options for a tagging object are exploited, to extend the reach in transverse momentum and rapidity. Objects like a Z-boson or a photon that can be measured in the electromagnetic calorimeter are used, avoiding the worse energy resolution in the hadronic calorimeter. As well as a recoiling jet, that is measured in the central region of the detector, thus probing the jet energy in non-central regions. To calibrate jets with high transverse momentum, several jets with lower p_T are used as a recoil, for which the calibration is well known.

The balance between a jet and a reference object is used to calibrate different transverse momentum regimes. The recoil of a Z-boson is used for the lowest transverse momentum, a recoil photon for the medium regime and the recoil of multiple jets for the high p_T region. Those methods use the scale from a simulation or are using reference objects that have an absolute scale, thus those are called absolute in situ methods.

The balance between two jets is used to calibrate different pseudo-rapidity regions in the detector, by comparing to the response in the well measured central region. This is a relative in situ technique as it depends on the reference calibration of the central region.

Z+jet Balance

To exploit the electromagnetic calorimeter, and calibrate also low p_T jets, a recoil Z-boson is used. The decay of a Z in an electron-positron pair is used to measure a p_T balance.

The events used are required to have exactly one electron and one positron with $E_T^e > 20\,\text{GeV}$ that are within $|\eta| < 2.47$, excluding a non-optimal instrumented region $1.37 < |\eta| < 1.52$. Additionally those electrons have to fulfill the *medium* quality requirements [111], which are defined, based on the shower shapes, the track quality and track-cluster matching criteria. If the two electrons have an opposite signed charge, and the invariant mass of the two electron system M_{ee} is close to the Z mass $66\,\text{GeV} < M_{ee} < 116\,\text{GeV}$, the event is kept.

The jet used in the analysis is required to have $p_T > 12\,\text{GeV}$ and be within $|\eta| < 1.2$. Also the jet has to be geometrically isolated from the electrons with $\Delta R(\text{jet}, e) > 0.5$. Any additional jets are required to have less than 20 % of the transverse momentum of the leading jet.

To reduce additional radiation perpendicular to the jet axis, a different definition for the reference p_T^{ref} is used. Instead of the transverse momentum of the Z-boson, the projection of the momentum on the jet axis is used:

$$p_T^{\text{ref}} = p_T^Z \cdot |\cos(\Delta\phi(\text{jet}, Z))| \tag{4.19}$$

The response $\frac{p_T^{\text{jet}}}{p_T^{\text{ref}}}$ is calculated in bins of $(p_T^{\text{ref}}, \Delta\phi(\text{jet}, Z))$. To estimate the mean of this distribution two methods are used. In the low p_T-regime with $p_T < 35\,\text{GeV}$ a fit taking into account the Poissonian nature of the process and the bias in the shape due to the p_T^{jet} selection is used. For the higher p_T-regime there is no such bias, and a regular mean is calculated.

The obtained mean values are also extrapolated to $\Delta\phi(\text{jet}, Z) = \pi$ with a linear fit function, to obtain an estimate for the region which is affected most by additional transverse radiation.

The response measurement is additionally influenced by underlying event, that adds energy to the measured recoil jet and out of cone effects, that decreases the energy of the measured jet. These two contributions are estimated using tracks.

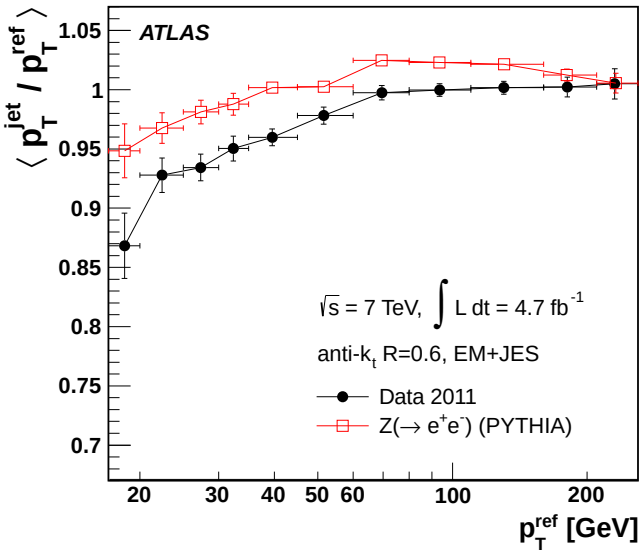

Figure 4.9: Transverse momentum response obtained from Z+jet balance for $\sqrt{s} = 7\,\text{TeV}$ [106].

The response compared between data and simulation is shown in Fig. 4.9 for $\sqrt{s} = 7\,\text{TeV}$. In the analysis of $\sqrt{s} = 8\,\text{TeV}$ data this response shows an improved agreement between simulation and data. The size of the correction for all regions in p_T is always smaller than 2 %.

γ+jet Balance

The response of the γ+jet balance method is calculated with two methods, that have different sensitivities to soft radiation and additional pileup contributions. The first method is the direct balance (DB) between the transverse momenta of jet and photon, thus defining the response as $\frac{p_T^{jet}}{p_T^{\gamma}}$. The second method is insensitive to the jet algorithm used, by exploiting the calculation of the missing transverse momentum E_T^{miss}. When projecting the transverse momentum of the photon on the direction of the missing transverse momentum, one obtains the response in the missing transverse momentum projection fraction (MPF) method:

$$\mathcal{R}_{MPF} = 1 + \frac{\vec{p}_T^{\gamma} \cdot \vec{E}_T^{miss}}{|p_T^{\gamma}|^2} \tag{4.20}$$

Here the missing energy is calculated from topological clusters.

Only events with one photon with transverse momentum $p_T^{\gamma} > 25\,\text{GeV}$ within $|\eta| < 1.37$ are considered for the calibration. This photon has to pass identification criteria based on photon shower properties. To reduce the influence of additional jets, the photon has to be isolated, such that in a cone of $R = 0.4$ around the photon, the pileup subtracted energy is smaller than 3 GeV.

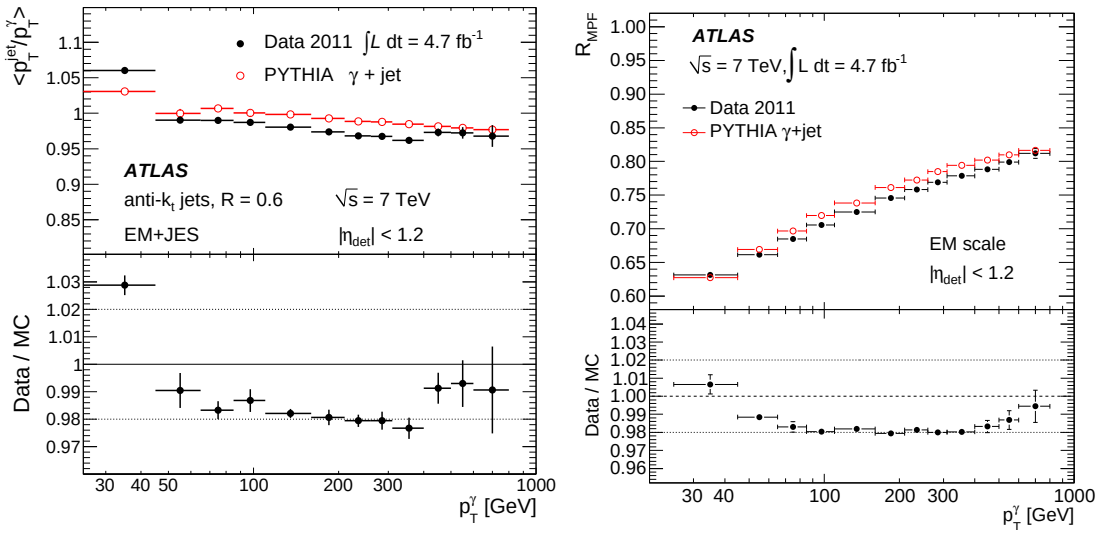

(a) Direct balance

(b) E_T^{miss} projection fraction (MPF)

Figure 4.10: Response for γ+jet using two different techniques [106] for $\sqrt{s} = 7\,\text{TeV}$.

As photons can undergo conversion to electrons and vice-versa, photons are classified according to tracks that are matched to the electromagnetic clusters. If there are no matched tracks, the photon is considered as unconverted. If there are one or two matched tracks originating from the conversion vertex, the photon is considered converted. To further suppress jets that might imitate a photon, only events with

$$0 < \frac{E_T^{\gamma,\text{cluster}}}{\sum p_T^{\text{track}}} < 2 \tag{4.21}$$

are kept for photons with one matched track. While for two matched tracks this fraction has to be between 0.5 and 2.0. Here $E_T^{\gamma,\text{cluster}}$ is the energy of the electromagnetic cluster identified as a photon candidate and p_T^{track} the transverse momentum of the matched tracks.

The jets considered in this calibration need a transverse momentum of $p_T > 12\,\text{GeV}$ and lay within $|\eta| < 1.2$. To suppress soft radiation an additional requirement on the geometrical distance $\Delta R(\text{jet}, \gamma) > 2.9$ is demanded. To suppress additional jets the transverse momentum has to be smaller than 20 % (30 %) of the leading jet transverse momentum for the DP (MPF) method.

The calibration is performed in bins of p_T^{γ}. The resulting responses for $\sqrt{s} = 7\,\text{TeV}$ are shown in Fig. 4.10(a) for the direct balance method, and in Fig. 4.10(b) for the MPF method. The agreement between data and simulation is always within 2 % for both methods. The same level of agreement is seen in the corresponding $\sqrt{s} = 8\,\text{TeV}$ analysis.

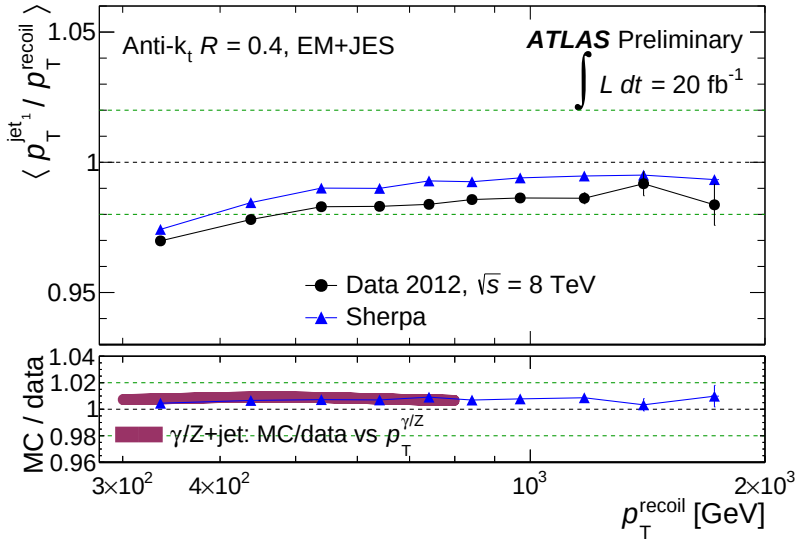

Figure 4.11: Transverse momentum balance in multijet events in data and MC [112].

Multijet Balance

For the calibration according to multiple jets balancing one jet, events with a minimum of three jets are selected, where the first jet has to be within $|\eta_1| < 1.2$ and the additional jets have to fulfill $|\eta_j| < 2.8$. Additionally the first jet is required to have $p_T > 300\,\text{GeV}$. The distribution used to calculate the correction is the response:

$$\mathcal{R}_{\text{MJB}} = \frac{p_T^{\text{leading}}}{p_T^{\text{recoil}}} \tag{4.22}$$

With the transverse momentum of the leading jet p_T^{leading} and the vectorial sum of the recoiling jets transverse momenta p_T^{recoil}. This quantity is not expected to be unity, as for low transverse momenta there are radiations of gluons and quarks, that are not contained in the selected jets but lost, which lowers the response. Instead the mismodeling in MC is corrected for by using a double ratio:

$$r = \frac{\mathcal{R}_{\text{MJB}}^{\text{data}}}{\mathcal{R}_{\text{MJB}}^{\text{MC}}} \tag{4.23}$$

The result of this analysis is shown in Fig. 4.11. In the upper panel the ratio $\mathcal{R}_{\text{MJB}}$ is shown for events from data and from simulation. In the lower panel the inverse of the double ratio $1/r$ is shown and compared to the result obtained in the γ+jet and Z+jet determination indicated with the purple band.

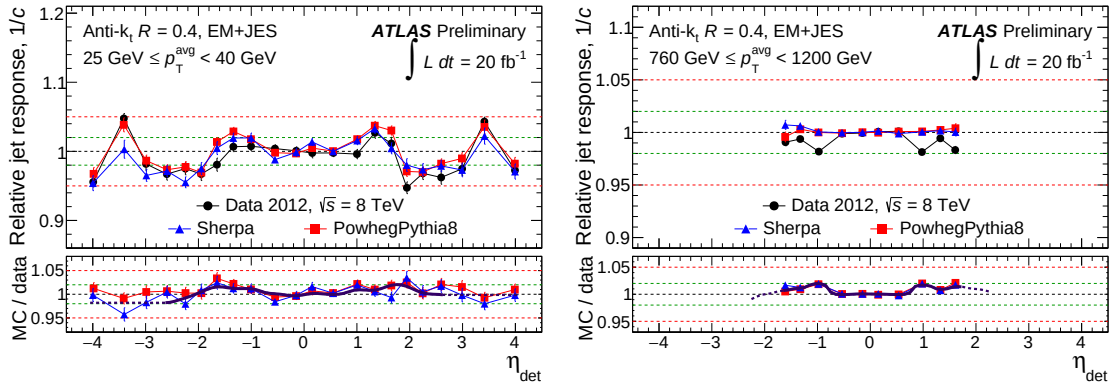

(a) For 25 GeV $\leqslant p_T^{avg} <$ 40 GeV

(b) For 85 GeV $\leqslant p_T^{avg} <$ 115 GeV

Figure 4.12: Calibration factors from dijet asymmetry from data and two different simulations for jets clustered with radius parameter R = 0.4 [112].

Dijet Asymmetry

For the measurement with one recoiling jet it is exploited that two jets have the same transverse momentum, at leading order. The transverse momentum asymmetry is studied as:

$$\mathcal{A} = \frac{p_T^{probe} - p_T^{ref}}{p_T^{avg}} \tag{4.24}$$

Where $p_T^{avg} = 0.5 \cdot (p_T^{probe} + p_T^{ref})$ is the average transverse momentum. For this correction only jets with $p_T > 25\,\text{GeV}$ that are within $|\eta| < 4.5$ are used. The final correction C is derived in bins of (p_T^{avg}, η_{det}) and defined as follows:

$$\frac{1}{C} = \frac{p_T^{probe}}{p_T^{ref}} = \frac{2+ < \mathcal{A} >}{2- < \mathcal{A} >} \tag{4.25}$$

To use the full statistics and thus minimize the statistical uncertainties, a matrix method is used which measures the response for a given detector region η_{probe} with respect to all possible reference regions η_{ref}, with the requirement that $|\eta_{ref}| < |\eta_{probe}|$. The result of this procedure for some exemplary regions in p_T^{avg} is shown in Fig. 4.12. The size of the correction is below 6 % in the low transverse momentum and large rapidity regions. For high transverse momentum and for low absolute rapidity the correction is well below 2 %.

Summary

All methods presented before use a reference object to balance against a jet, to calibrate the energy of jets. For jets with $p_T < 100\,\text{GeV}$ a Z-boson is used as a reference object. The correction obtained in this regime is always below 2 %. For a medium transverse momentum of $100\,\text{GeV} < p_T < 700\,\text{GeV}$ the recoil of a photon dominates the correction, resulting also in a correction of about 2 %. For the highest p_T region above 700 GeV the recoil of several low p_T jets is used. Here the calibration factor is also around 2 %. Comparing the calibration factor obtained in the multijet method for transverse momenta comparable to the ones used in Z or photon balance, shows a good agreement between those methods.

The method of relative calibration of different pseudo-rapidity regions gives calibration factors of up to 5 %. For high transverse momenta of $p_T > 85\,\%$ this correction is always below 2 %.

JET ENERGY SCALE UNCERTAINTY

Pileup Components

To estimate the systematic uncertainty from applying the pileup calibration, two methods are used. One method uses track jets, as a pileup independent probe to estimate the remaining pileup dependence. For this study track jets within $|\eta| < 2.1$ are used with a transverse momentum of $15\,\text{GeV} < p_T^{\text{track}} < 30\,\text{GeV}$. The dependence of the calorimeter jet p_T on pileup variables is studied for data and simulated events. In Fig. 4.13(a) and Fig. 4.13(b) the results of this study are shown. Data and MC show no remaining dependence on $\langle\mu\rangle$. While an overcorrection in N_{PV} is found, and used as a systematic uncertainty.

A second method to estimate the pileup systematic uncertainty uses the balance between Z-boson and a jet. The difference between jet transverse momentum and reference transverse momentum $\Delta p_T = p_T^{\text{jet}} - p_T^{\text{ref}}$ is supposed to be pileup independent. As a reference the transverse momentum of the Z-boson projected on the jet axis is used. To estimate a systematic uncertainty the dependence of Δp_T on $\langle\mu\rangle$ is studied as a function of p_T^{ref}. The result for two detector regions is shown in Fig. 4.14(a) and in Fig. 4.14(b). The difference of this slope to zero is used as a systematic uncertainty.

These two results are combined to extract systematic uncertainties on the transverse momentum of a jet according to the number of primary vertices and the average number of interactions. Additionally a systematic uncertainty covering the uncertainty on the knowledge of the slope between ρ and $\langle\mu\rangle$ is assigned. Also a systematic uncertainty on the knowledge of ρ is used.

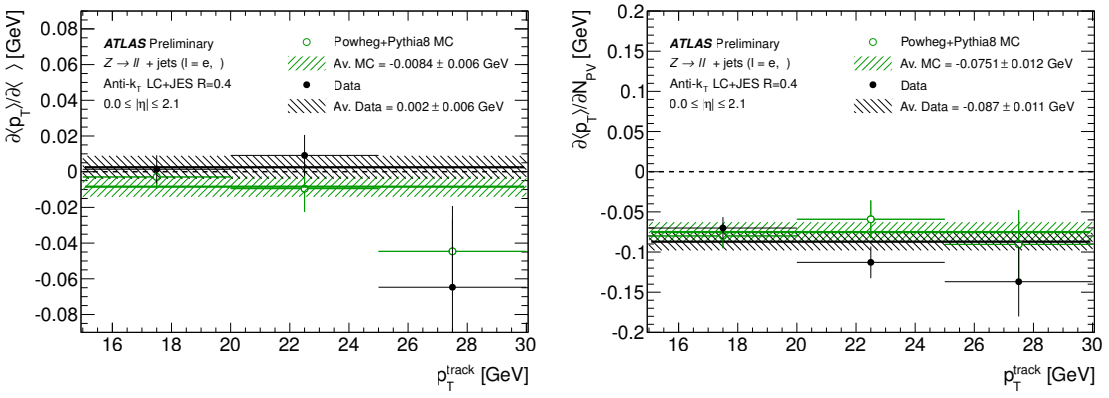

(a) Dependence on $\langle\mu\rangle$ **(b)** Dependence on N_{PV}

Figure 4.13: Dependence of calorimeter jet transverse momentum on pileup contributions as a function of track transverse momentum [107].

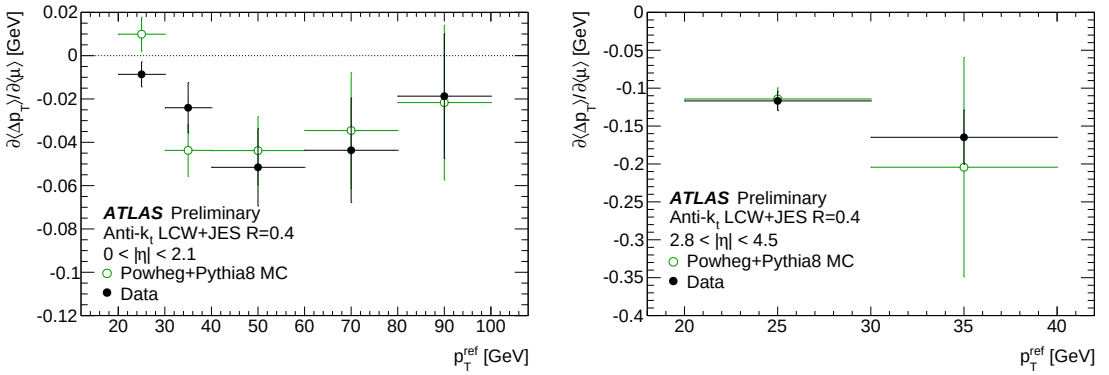

(a) Central detector region **(b)** Forward region

Figure 4.14: Dependence of transverse momentum difference between reference and jet on $\langle\mu\rangle$ as a function of reference transverse momentum [107].

In Situ Components

Dijet Asymmetry

The largest uncertainty in the dijet asymmetry calibration is given by the modeling. This uncertainty is estimated from a comparison between SHERPA and POWHEG+PYTHIA8. Those two generators give an accuracy in the variables sensitive to third jet modeling up to leading order. Additional uncertainties due to the choice of renormalization and factorization scale are evaluated by changing the scales by 0.5 to 2, and are found to have a small impact. A third MC related uncertainty is probing the influence of the shower description, by comparing the generated POWHEG events showered with PYTHIA8 or HERWIG. The difference between those shower simulations is also small.

The selection of $\Delta\phi > 2.5\,\text{rad}$ was altered by $\pm 0.3\,\text{rad}$ to estimate the impact on the final calibration. Additionally to estimate the impact from pileup, the sample to derive the calibration was split up in low and high $\langle\mu\rangle$ and the difference in calibration was used as systematic uncertainty. The selection according to jet vertex fraction, was altered to estimate the systematic uncertainty by this selection step.

Also the jet energy resolution (JER) was examined, by smearing the MC with a Gaussian, the systematic uncertainty due to JER was estimated.

All systematic and statistical uncertainty components are shown in Fig. 4.15(a) for jets with $p_T = 35\,\text{GeV}$. For a central pseudo-rapidity the main systematic uncertainty is from statistics, while for pseudo-rapidity $|\eta| > 1$ the simulation modeling uncertainty dominates. In Fig. 4.15(b) the uncertainty for a higher momentum of $p_T = 300\,\text{GeV}$ is shown, the dominating uncertainties are similar to the low p_T scenario, except for the jet energy resolution uncertainty which dominates for $0.7 < |\eta| < 1.4$. For high p_T jets this uncertainty stays always well below 1 % in the central region $|\eta| < 3.0$.

Multijet Balance

As the multijet balance (MJB) uses jets that are already calibrated by the other in situ methods, the systematic uncertainties from those methods have to be propagated into the MJB method. Varying every single component by $\pm 1\sigma$, calculating the MJB response for these variations, and finally comparing those variations, gives an estimate of the propagated systematic uncertainty.

To estimate the impact of specific choices in the kinematic selection, the p_T threshold, the asymmetry and the two angles used α and β are varied.

The impact of modeling is estimated by comparing MJB responses for different generators. The response is calculated with SHERPA, POWHEG+PYTHIA8, PYTHIA8 and HERWIG++. The symmetrized envelope of those corrections is used as an uncertainty.

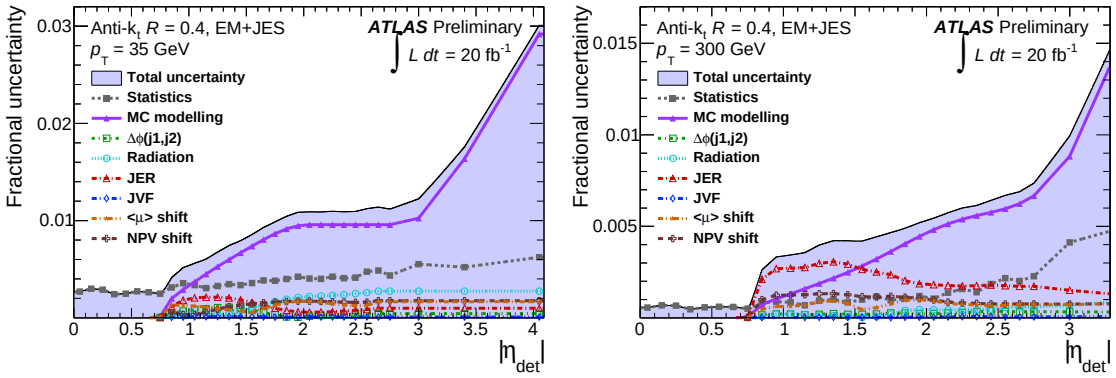

(a) For jets with $p_T = 35\,GeV$ **(b)** For jets with $p_T = 300\,GeV$

Figure 4.15: Systematic uncertainty components from dijet asymmetry method [112].

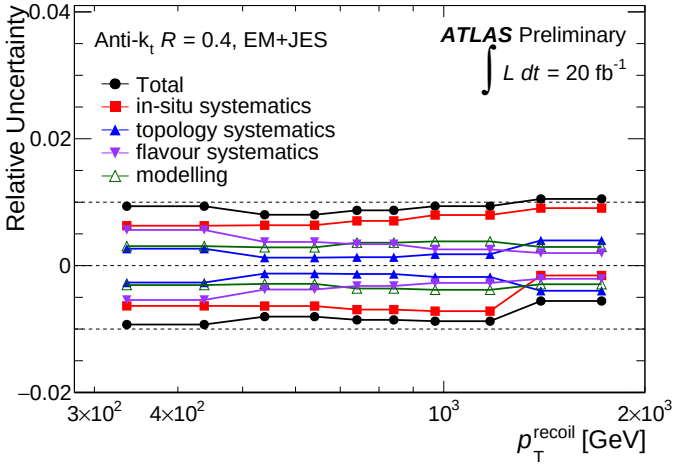

Figure 4.16: Systematic uncertainty components in multijet balance method [112].

Additionally a systematic uncertainty on the parton flavor is calculated. The uncertainty from the flavor response is propagated by shifting all jets simultaneously, while for the flavor composition the jets are shifted independently.

All systematic uncertainties used are summarized in Fig. 4.16. The total uncertainty is always below 1 %, while for higher transverse momenta the dominating uncertainty is the in situ systematics.

Z+jet Balance

In the Z+jet balance method a wide variety of systematic uncertainties was considered. The uncertainty on the width parametrization was propagated. The fit range for the $\Delta\phi$ extrapolation was varied. Also the selection of the subleading jet p_T was varied. The calculation of the effects

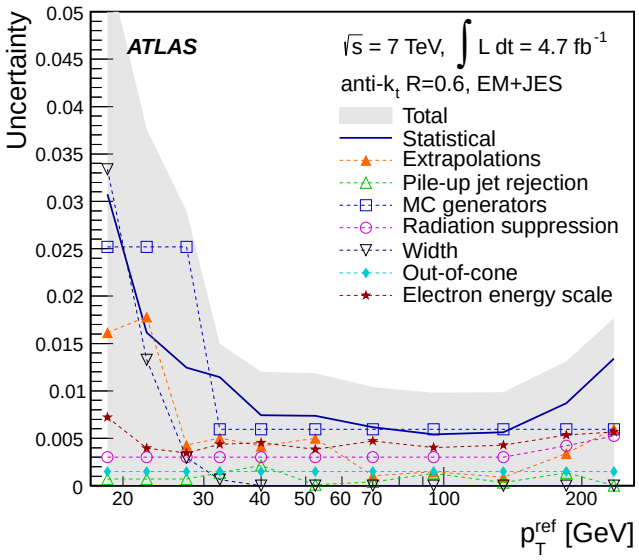

Figure 4.17: Systematic uncertainty components in Z+jet balance method [106].

of underlying event and out-of-cone was compared between data and simulation, to estimate the uncertainty on this method. The effect of pileup on the calibration was also studied. Additionally the electron energy scale was propagated to the final response.

To estimate the modeling uncertainty, the correction for PYTHIA and ALPGEN+HERWIG was compared.

A summary of all systematic uncertainties in the Z+jet balance method is shown in Fig. 4.17. For jets with $p_T > 30\,\text{GeV}$, the systematic uncertainty is always below 2 %.

γ+jet Balance

To estimate the influence of pileup on the γ-jet balance method, the sample used to derive the correction, is divided twice in two parts. For all values of $\langle\mu\rangle$ the sample is divided in low and high N_{PV}. Similarly for all values of N_{PV}, the sample is divided in low and high $\langle\mu\rangle$. The difference in the results between those samples is always smaller than 0.5 %.

The selection criteria on p_T^{sublead} and $\Delta\phi(\text{jet},\gamma)$ to suppress soft radiation are varied independently. This gives an additional systematic uncertainty of about 0.5 %.

The fraction of jets that are misidentified as photons is estimated. This included the variation in response by comparing the nominal result with a small jets enriched sample. The purity of the γ-jet samples used is estimated by a side-band technique. Additionally the influence of pileup on the purity measurement is taken into account. The total effect is estimated as 2.5 % at low photon transverse momentum, and 0.1 % for high p_T.

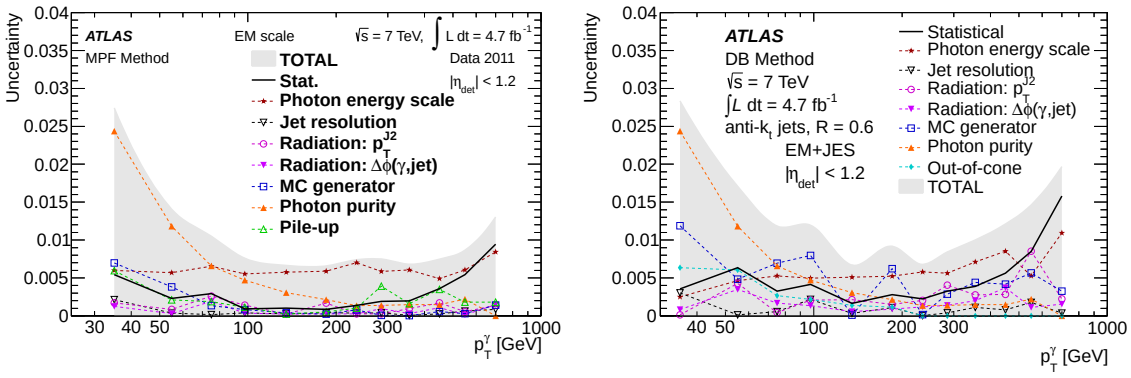

(a) From MPF method

(b) From DB method

Figure 4.18: Systematic uncertainty components from γ-jet method [106].

The influence of the γ energy scale is propagated to the result and found to be smaller than 0.8 %.

The jet energy resolution is also propagated to the final response, and used as a systematic uncertainty.

To estimate the model dependence, the calibration is performed with PYTHIA and HERWIG.

Additionally out-of-cone effects are taken into account, by varying constants used in the derivation of the out-of-cone effect. Also the disagreement between simulation and data is used to cover the model uncertainties.

In Fig. 4.18(a) the uncertainty components for the MPF method are summarized. The components for the DB method are shown in Fig. 4.18(b). The total uncertainty is similar for both methods and always below 1.5 % for photons with $p_T > 50\,\text{GeV}$.

Summary of In Situ Components

The total impact of the different systematic uncertainty components originating from the in situ methods is shown in Fig. 4.19. Low jet transverse momenta are calibrated by the Z+jet method, while the high p_T regime is only determined by the multijet balance method. In the overlapping region between those two extremes, the γ-jet balance is used. The total uncertainty of those methods is always below 3 %.

Single Hadron Response

To estimate an uncertainty in the highest measured p_T regime a single hadron measurement is used. Single isolated hadrons are measured in minimum bias data for momenta up to 20 GeV. For the momentum range between 20 GeV and 350 GeV, pions have been measured in a test

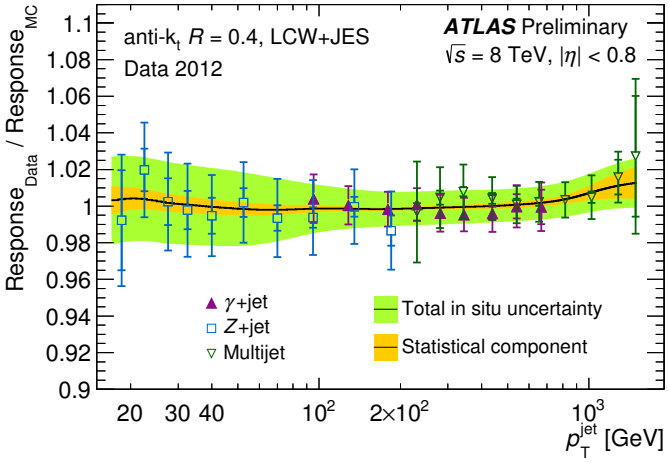

Figure 4.19: Systematic uncertainty components from in situ components [113].

beam setup. Hadrons have been selected by calculating the energy in a narrow cone around an isolated track. The variable studied is the ratio between the energy in this cone and the track momentum.

The systematic uncertainties considered include the choice of the noise threshold, which is estimated together with the calorimeter acceptance by comparing the measurement in cells with the one in topological clusters. Additionally the response to different hadrons is studied, by comparing three different hadronic shower models in simulated data.

An additional systematic uncertainty covers the difference in response between the final setup of ATLAS and the setup of detectors used in the combined test beam (CTP), which used only parts of ATLAS.

Also an uncertainty on the absolute electromagnetic energy scale is taken into account. As for momenta above 400 GeV no data is available, an additional uncertainty of 10 % is added.

A summary of all uncertainty components is shown in Fig. 4.20. The total uncertainty is 4 % for low p_T and decreases to about 2 % for jets with $p_T = 1$ TeV. The uncertainty is only used above the upper threshold for multijet balance, where the extrapolation uncertainty dominates.

Monte Carlo Non-Closure

The here presented jet calibration uses events, that have been simulated taking into account a detector description from early 2012, before data taking started. During data taking this description was optimized and changes in the geometry improved the agreement between the description and the detector. Additionally the samples used a full simulation of the detector. For practical reasons, many steps for example the shower development, have not been simulated on an event-by-event basis in large samples used by the physics analysis. To save time and

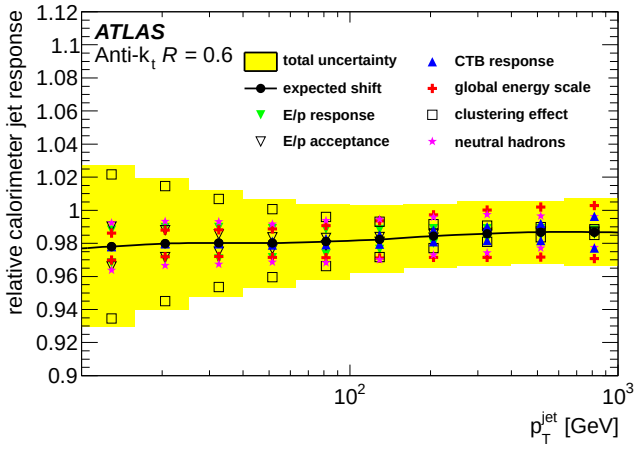

Figure 4.20: Systematic uncertainty components from single hadron response [106].

computing resources libraries of templates have been generated, and for example the shower shapes have been selected from those. This fast type of a simulation does not describe all variables as good as the full type. Thus an uncertainty is added to jets, if the simulated sample used is not of the same detector geometry or not a full simulation sample.

Summary

The jet energy scale uncertainty for data recorded in 2012 at $\sqrt{s} = 8\,\text{TeV}$ was presented. In total there are four components describing the pileup dependence, 58 components are describing the uncertainties in the in situ methods, one component the high-p_T single hadron method and one component the difference due to different detector descriptions used.

In practice many of those components are negligible for a given selection. To speed up analysis a reduction of the number of components is provided, which keeps the correlation between components, while combining uncertainty components, according to their source. In this thesis one of these reduced sets is used, where the 58 in situ components are merged into 23 categories. To further decrease the needed computing time, only in phase space regions where there is an impact by using separate components, those are used. Else the sum in quadrature of all components is sufficient.

The final summary of all systematic uncertainty components is shown in Fig. 4.21. For the low p_T region the uncertainty is around 4 %, dominated by the absolute in situ uncertainty and the pileup component. In the medium and high p_T regime the uncertainty is dominated by the absolute in situ component and varies between less than 2 % in the medium region up to 3 % in the highest p_T region. The total uncertainty in the central region is always below 4 %, increasing in regions with $|\eta > |3$ up to 7 %.

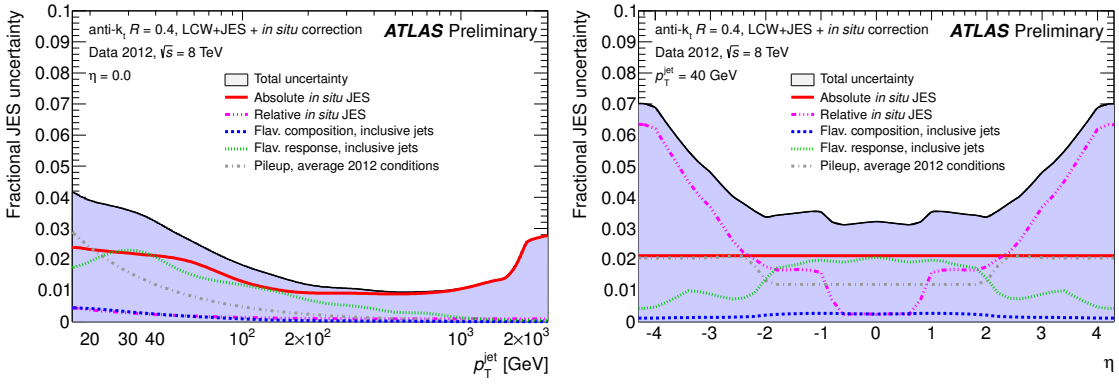

(a) p_T dependence **(b)** η dependence

Figure 4.21: Systematic uncertainty components in jet energy scale determination in LCW+JES calibration scheme [113].

JET ENERGY RESOLUTION

The jet energy resolution (JER) is determined in in situ measurements as well as in simulated events [112]. The transverse momentum balance between two jets is exploited to measure the energy resolution with two different methods.

One method examines the asymmetry between the transverse momenta:

$$A(p_{T,1}, p_{T,2}) = \frac{p_{T,1} - p_{T,2}}{p_{T,1} + p_{T,2}} \tag{4.26}$$

For a perfectly balanced dijet system this asymmetry is expected to be zero, the width of this distribution can then be related to the jet energy resolution. As additional radiation would spoil this behavior, an extrapolation of the third jets transverse momentum to zero is performed.

The second method uses a clever chosen coordinate system ($\psi - \Psi$). This coordinate system is chosen in a plane perpendicular to the beam axis, with the ψ-axis being the bisector of the two jets transverse momentum vectors. The Ψ-axis lies in the same plane, but perpendicular to the ψ-axis. This choice minimizes additional soft radiation and underlying event, as those will contribute isotropically.

The fractional jet energy resolution obtained in the central region $|\eta| < 0.8$ from these methods give 15 % for an average dijet transverse momentum of 30 GeV, and 7 % at a transverse momentum of 500 GeV.

Systematic Uncertainties

Three sources of systematic uncertainties are taken into account in this analysis. The experimental uncertainties from varying the selection criteria, the difference between the results obtained from the two different methods and the difference in modeling obtained when comparing to simulated events from different generators.

The total uncertainties are always smaller than 20 %, while being around 10 % in the central region of $0 < |\eta| < 0.8$.

5 DIJET RESONANCE SEARCH

In this chapter the search for New Physics in the dijet invariant mass spectrum using events recorded at the ATLAS detector is shown. The following sections summarize the own work of the author, and are a refined version of the work the author was also contributing to the ATLAS publication [114].

In Sec. 5.1 the main idea of the analysis is shown. The improvement in trigger combinations is detailed in Sec. 5.2. An extensive overview of the selection criteria imposed on the events is shown in Sec. 5.3. In Sec. 5.4 the method to estimate the background is discussed and finally in Sec. 5.5 the search is presented with the results of the limit setting.

ANALYSIS STRATEGY

The search for dijet resonances focuses on the fact, that the dijet mass spectrum obtained from Standard Model (SM) processes is expected to be smoothly falling for masses above the resonances from W and Z boson. New Physics (NP) could manifest in this spectrum as an additional resonance as can be seen in Fig. 5.1.

The high rates of dijet events from SM processes give rise to a small sensitivity to NP signals. To increase this sensitivity the different kinematic configurations of SM and New Physics processes are exploited. In Fig. 5.2(a) the events from SM processes are shown, which are mainly of a t-channel nature, and thus are concentrated at large absolute values of the rapidity separation $|y^*|$. In contrast the same distribution has a different shape for NP signals. In Fig. 5.2(b) this is shown for an excited quark of mass $m_{q^*} = 3\,\text{TeV}$. The production of an s-channel resonance leads to a rapidity distribution of the decay products close to zero. Selecting events with a small rapidity separation $|y^*|$ is used to increase the sensitivity. To search in a fairly model independent way, this is the only kinematical selection criterion. According to ATLAS policy the analysis published in [114] used a quarter of the dataset to define the final selection criteria before analyzing the full dataset. As the selection criteria did not change between this work and the published analysis, this procedure was not followed again for this work. Instead the full dataset with $\mathcal{L} = 20.3\,\text{fb}^{-1}$ is shown in this section, except for the simple kinematic distributions where a reduced dataset of $\mathcal{L} = 18.4\,\text{fb}^{-1}$ is shown, due to data availability issues. The small amount of data missing for these kinematical comparisons does not introduce a bias, as it is randomly distributed time.

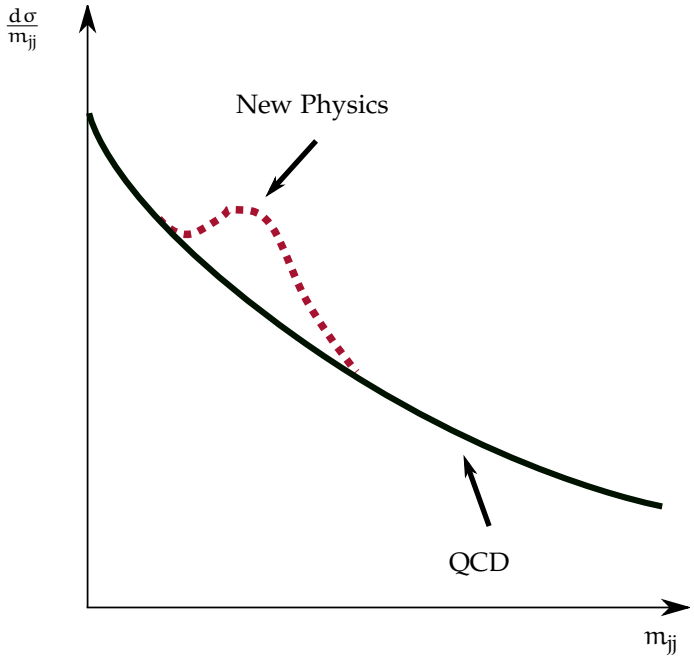

Figure 5.1: Sketch of a resonance from New Physics on top of a smooth background from QCD shown in dijet mass.

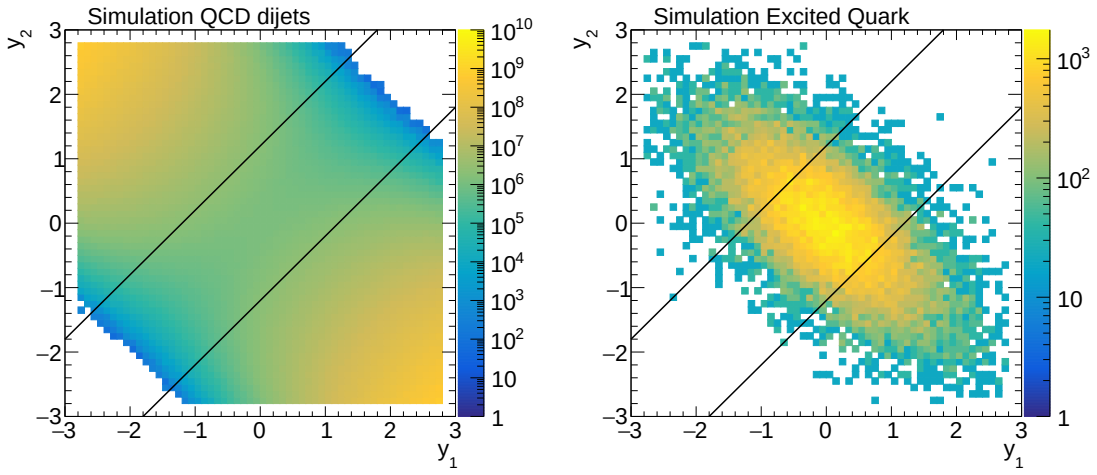

(a) SM QCD processes

(b) Excited Quark decay

Figure 5.2: Rapidity of leading jet vs. rapidity of subleading jet.

TRIGGER

The main improvement of this analysis over most of the former analyses is the reach in dijet mass. With increasing center of mass energy and luminosity higher masses are probed. Due to rate limitations low mass events with a huge cross section are ignored successively in the course of the last decades of dijet searches. However, New Physics might show up at those low masses that are omitted nowadays, due to a smaller coupling than expected (see also [115]). To overcome this shortcoming events from a combination of different triggers are used in this analysis.

Within ATLAS a large variety of triggers have been selecting events. For jets the natural choice is the single jet trigger. This trigger selects events where one jet exceeds a certain threshold in transverse momentum p_T. Another possible choice is a trigger that sums up the p_T of all jets above a certain p_T and selects events, if this sum exceeds a given threshold. In this analysis 11 single jet triggers and one trigger which selects based on the sum of p_T are used. The nomenclature for triggers within ATLAS includes details about the thresholds used and the calibration level of the jet at trigger level. Single jet triggers are named in the form EF_jXXX_a4tchad. Here XXX gives the threshold in p_T. In this analysis XXX ranges from 15 GeV to 280 GeV. The suffix a4tchad gives the used jet clustering algorithm (**a**nti-k_T with radius parameter $R = 0.4$) and the calibration scheme (**t**opo**c**lusters calibrated to **had**ronic scale). The trigger using the sum of momenta has an additional suffix _ht700_L2FS, where 700 gives the threshold in GeV for the sum of p_T for all jets with $p_T > 45$ GeV.

To keep the recorded rate at a reasonable level, triggers with lower thresholds use a so-called *prescale factor* p. This means that from those triggers only every p-th event that fulfills the trigger requirement gets recorded. This leads to a recorded luminosity per trigger which is dependent on the prescale factor. In Tab. 5.1 the luminosity per trigger is shown. Several options exist to combine events recorded selected by triggers with different prescales, to assemble one complete spectrum from the lowest dijet masses to the highest.

Delayed Trigger Stream

During the 2012 data taking a fraction of the recorded data has not been reconstructed immediately. This so-called *delayed* data stream was written to tape and reconstructed in early 2013 after the data taking ended. The triggers from this stream have an additional suffix _delayed. For this analysis the trigger EF_j220_a10tcem_delayed was used. Here the jets used are reconstructed with the **a**nti-k_T algorithm with a radius parameter of $R = 1.0$ using **t**opo-**c**lusters calibrated at the **e**lectro **m**agnetic scale. As this trigger stream was not activated during the whole 2012 data taking, the final spectrum has to be assembled from the two disjunct sets of data, one dataset for when the delayed trigger stream was active and one dataset for the remaining time. The

Jet Trigger Name	Luminosity/fb
EF_j145_a4tchad_ht700_L2FS	20.3
EF_j220_a10tcem_delayed	17.3
EF_j280_a4tchad	1.17
EF_j220_a4tchad	0.26
EF_j180_a4tchad	7.90×10^{-2}
EF_j145_a4tchad	3.64×10^{-2}
EF_j110_a4tchad	9.84×10^{-3}
EF_j80_a4tchad	2.32×10^{-3}
EF_j55_a4tchad	4.43×10^{-4}
EF_j35_a4tchad	4.54×10^{-4}
EF_j25_a4tchad	7.87×10^{-5}
EF_j15_a4tchad	1.48×10^{-5}

Table 5.1: Integrated luminosity per jet trigger, for triggers used in this analysis.

integrated luminosity recorded while the delayed stream was active accounts for $L = 17.3\,\text{fb}^{-1}$, while the stream was deactivated when $L = 3.0\,\text{fb}^{-1}$ was recorded by the regular stream. The following steps of trigger combination are thus performed on both streams separately.

Trigger Efficiency

The single jet triggers of ATLAS select events if the energy of a jet in this event exceeds a certain threshold. Those energies have to be available during data taking, to reduce the amount of data that is written to disk or tape. At this time not all information about a jet are available or already calculated. This leads to a preliminary calibrated energy (see Sec. 4.4 for full jet calibration) used by the trigger, which lacks the origin correction, and the global sequential correction, due to missing tracking information. For the calculation of the energy at trigger level a specific calibration scheme and jet algorithm has to be chosen. The final variables used in an analysis have been calibrated with more sophisticated methods and for a large variety of jet algorithms and radius parameters, not necessarily identical to the ones at trigger level.

To account for this difference in jet algorithm and calibration an efficiency for the trigger is calculated as a function of the variables used in the analysis. For establishing a well known distribution it is paramount to have a trigger efficiency close to 1. In this analysis events were used when the trigger efficiency was in a plateau above 99.5 %. The trigger efficiency for a trigger as a function of the calibrated p_T can be estimated from data as:

$$\epsilon(p_T) = \frac{N_{t\&p}(p_T)}{N_t(p_T)} \tag{5.1}$$

Jet Trigger Name	99.5% p_T efficient/GeV
EF_j145_a4tchad_ht700_L2FS	460
EF_j280_a4tchad	411
EF_j220_a4tchad	341
EF_j180_a4tchad	273
EF_j145_a4tchad	241
EF_j110_a4tchad	185
EF_j80_a4tchad	135
EF_j55_a4tchad	99
EF_j35_a4tchad	59
EF_j25_a4tchad	47
EF_j15_a4tchad	27
EF_j220_a10tcem_delayed	333

Table 5.2: Triggers used in the analysis and corresponding lowest transverse momenta with $\epsilon > 99.5\,\%$.

Here N_t is the number of events passing a *tag trigger*, which is a trigger known to be efficient in the region to probe. $N_{t\&p}$ is the number of events passing the tag trigger and the *probe trigger*, which is the trigger to examine.

The difference in the variables used on the trigger level and those in the analysis lead to a smeared energy resolution. Thus the efficiency deviates from the expected unit-step-like function.

To select a probe trigger that is fully efficient in the region of interest, a successive technique was used. For estimating the efficiency of the triggers with the lowest thresholds, a random trigger was used as probe. This kind of trigger randomly selects events from collision data. Those low threshold triggers were then used as tag triggers for the higher threshold ones, if the region of interest was well above the formerly extracted full efficiency point in p_T. This procedure is applied successively, until an efficiency estimation for every trigger under consideration is obtained. From those the lowest p_T for which the efficiency is always above 99.5% is extracted and thus the region of phase space for which a trigger is suited is determined. An example of this trigger efficiency for two different triggers that have been used in this analysis is shown in Fig. 5.3. The results for all jet triggers used can be found in Tab. 5.2, while all plots are shown in Appx. B.

One Trigger per Phase Space Region

The simplest option to use several triggers in one analysis, is to divide the phase space in exclusive regions [116]. To each of those regions exactly one single trigger is assigned. A weight factor w has to be used, to obtain a spectrum as seen by the detector before applying prescales, which is equal to the prescale of the corresponding trigger.

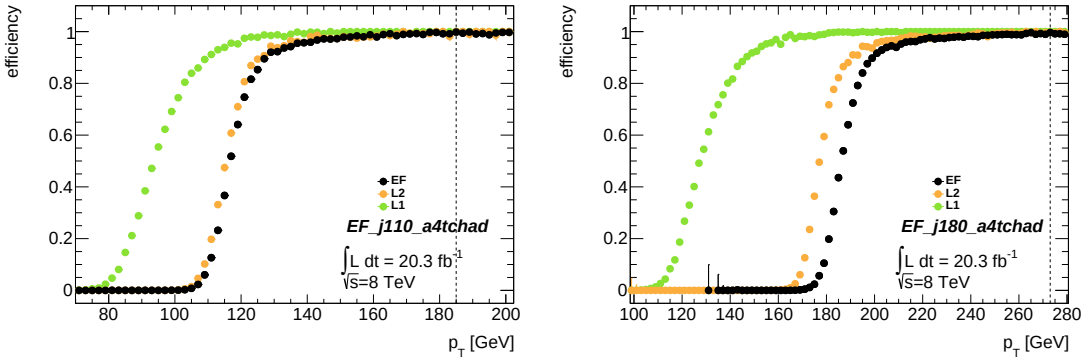

(a) Efficiency for j110

(b) Efficiency for j180

Figure 5.3: Example single jet trigger efficiencies for all three trigger levels, with the point of 99.5 % marked with a dashed line.

During data taking the conditions within an accelerator can change significantly. I.e. the instantaneous luminosity decreases exponentially with time. To keep the recorded rate of events constant, the prescale values are adjusted simultaneously. In ATLAS the data taking is divided into so-called *lumiblocks* of 60 s length, in which the conditions are assumed to stay constant. Prescale values are constant within a lumiblock. The total number of expected events N_{exp} in one region of the phase space is then calculated as:

$$N_{exp} = \sum_i N_{obs,i} w_i \tag{5.2}$$

Here w_i gives the prescale of an event at the time of recording the event, i denotes a lumiblock and $N_{obs,i}$ is the number of observed events in a lumiblock. As this prescale may vary strongly, the expected number of events will be strongly influenced by single events with a large prescale factor. This is a purely statistical effect, that does not originate from the physics of the observed process, and thus could be avoided. This can be done by averaging the weight that is associated to an event with specific properties over the whole data taking period:

$$w_i^{avg} = \frac{\sum_j \mathcal{L}_j}{\sum_j \frac{\mathcal{L}_j}{p_{ji}}} \tag{5.3}$$

Where p_{ji} gives the prescale for a given trigger i in a given period of time denoted by j. The integrated luminosity in that period of time is $\mathcal{L}_j$.

This averaging of the weight decreases statistical fluctuations and leads to smaller statistical uncertainties.

Combination of Triggers per Phase Space Region

To further increase the collected number of events, a combination of several triggers can be used. This is a simple expansion of the former mentioned method. Instead of assigning one trigger per phase space region, a combination of single jet triggers can be used. This uses the nature of the single jet triggers. Every event that is accepted by a trigger with a specific threshold will also be accepted by a trigger with a lower threshold. To each region of phase space a combination of all single jet triggers is assigned, that are fully efficient in this region.

The weight to upscale the events taken by this combination can be calculated by a simple probability consideration. The probability to miss an event, that is triggered by a fully efficient single trigger with prescale p is:

$$P_{\text{miss}} = 1 - \frac{1}{p} \tag{5.4}$$

Thus the probability to miss an event considering all triggers with corresponding prescales p_k is:

$$P_{\text{miss, all}} = \prod_k \left(1 - \frac{1}{p_k}\right) \tag{5.5}$$

This product only contains factors from triggers, that are fully efficient in the particular phase space region. The resulting weight is as follows:

$$w_{ij} = \frac{1}{1 - P_{\text{miss, all,ij}}} \tag{5.6}$$

This weight is dependent on the region of phase space denoted with i and the prescales which change with time, denoted as j. Analog to the former method, an averaging is performed:

$$w_i = \frac{\sum_j \mathcal{L}_j}{\sum_j \frac{\mathcal{L}_j}{w_{ji}}} \tag{5.7}$$

The results of this procedure, the weights per phase space region, can be seen in Tab. 5.3 and Tab. 5.4 for the two parts of data used in this analysis.

The result of this combination, shown in Fig. 5.4, is a full dijet mass spectrum, which is corrected for the prescales. The figure on the left shows the combination representing $\mathcal{L} = 3.0\,\text{fb}^{-1}$ taken from the jet stream data, while on the right side the combination of the delayed stream data is shown equivalent to $\mathcal{L} = 17.3\,\text{fb}^{-1}$.

Highest efficient Jet Trigger	Effective prescales	Number of Entries
EF_j145_a4tchad_ht700_L2FS	1.0	463 997
EF_j280_a4tchad	9.4	86 532
EF_j220_a4tchad	40.7	65 466
EF_j180_a4tchad	130.0	62 838
EF_j145_a4tchad	297.2	43 409
EF_j110_a4tchad	1137.4	64 400
EF_j80_a4tchad	5103.3	62 817
EF_j55_a4tchad	28 023.2	25 003
EF_j35_a4tchad	197 413.5	521
EF_j25_a4tchad	1 279 509.4	0
EF_j15_a4tchad	7 861 303.0	0

Table 5.3: Effective prescales and number of events per trigger category (exclusively normal stream).

Highest efficient Jet Trigger	Effective prescales	Number of Entries
EF_j220_a10tcem_delayed	1.0	15 988 104
EF_j180_a4tchad	202.1	152 612
EF_j145_a4tchad	594.5	71 435
EF_j110_a4tchad	2268.1	105 842
EF_j80_a4tchad	10 033.2	106 854
EF_j55_a4tchad	56 266.0	40 276
EF_j35_a4tchad	461 028.3	627
EF_j25_a4tchad	2 331 715.8	0
EF_j15_a4tchad	15 314 795.5	0

Table 5.4: Effective prescales per trigger category (delayed stream on).

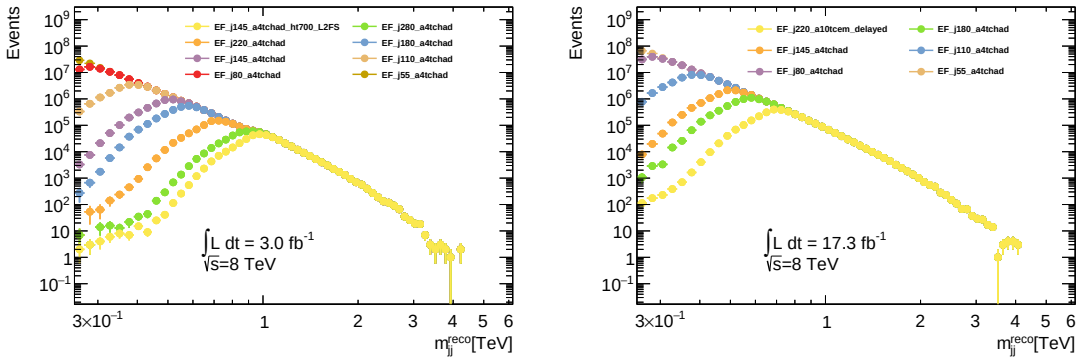

(a) Jet stream data. **(b)** Delayed stream data.

Figure 5.4: Combination of single jet triggers.

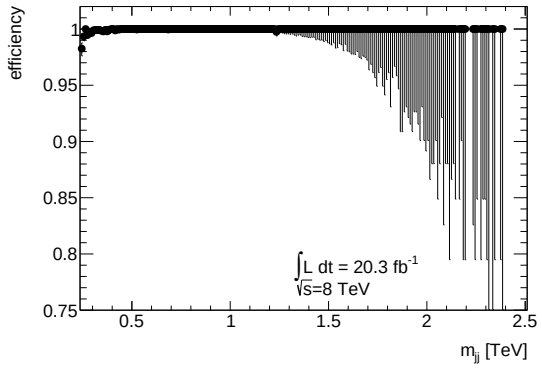

Figure 5.5: Efficiency of combined trigger selection as a function of reconstructed dijet mass.

Combination of Trigger Streams

The method shown in the preceding paragraph gives a full dijet mass spectrum, for each of the two trigger streams under consideration. To combine the two spectra, there are several possibilities. Naïvely adding the two spectra leads to a loss of sensitivity in some regions where largely different weights from the two streams occur. As the two spectra represent two independent measurements of the same distribution, they can be combined as a weighted sum of the cross sections in each bin:

$$\sigma_{avg} = \frac{\sigma_1 \cdot w_1 + \sigma_2 \cdot w_2}{w_1 + w_2} \tag{5.8}$$

Here the cross sections per stream are $\sigma_i = N_i/\mathcal{L}_i$, with the number of events N_i and the recorded luminosity $\mathcal{L}_i$. The weights are chosen according to the statistical power of the datasets used as $w_i = 1/(\Delta\sigma_i)^2 = \mathcal{L}_i^2/(\Delta N_i)^2$. Scaling this averaged cross section by the total luminosity gives the final number of entries per bin,

$$N_{total} = \sigma_{avg} \cdot (\mathcal{L}_1 + \mathcal{L}_2) \tag{5.9}$$

with the corresponding uncertainty:

$$\Delta N_{total} = \frac{1}{\sqrt{w_1 + w_2}} \cdot (\mathcal{L}_1 + \mathcal{L}_2) \tag{5.10}$$

This gives an uncertainty that is bigger than the corresponding Gaussian one, as expected from the effective statistics. For the bin around 800 GeV one obtains 1.8×10^6 events, with an uncertainty of $\Delta N = 1823$ events.

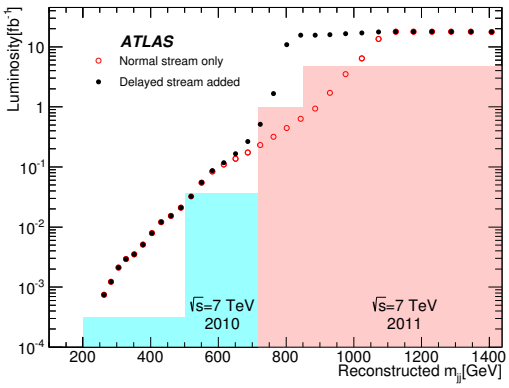

Figure 5.6: Effective integrated luminosity recorded with jet stream only and with delayed stream added [114].

The combination of triggers results in an efficiency in dijet mass, which is shown in Fig. 5.5. To obtain this trigger efficiency for the full spectrum, the trigger to transverse momentum association as obtained above is used. The denominator of the efficiency calculation contains events that pass a lower threshold trigger combination, where the same tag triggers are used as in the single jet method.

The impact of adding the delayed stream is shown in Fig. 5.6, which shows that the effective luminosity $\mathcal{L}_{\text{eff}} = \mathcal{L}/w$ does surpass the luminosities recorded a low dijet masses in 2010 and 2011 if the delayed stream is added.

EVENT SELECTION

The selection of events can be divided in three main parts:

EVENT QUALITY: These selection criteria guarantee that the quality of the recorded events is high. This includes that all parts of the detector were in good conditions and ready. In addition, an event is only considered when the jet with the highest transverse momentum (leading jet) and with the second to highest transverse momentum (subleading jet) are measured well.

KINEMATIC CUTS: This set of criteria is used to remove the bias from trigger turn on and to be not influenced by additional pileup contributions. For this events where the leading or subleading jet are below $p_T = 50\,\text{GeV}$ are rejected. Combined with one of the later cuts, this gives a smoothly falling spectrum only for dijet masses with $m_{jj} > 253\,\text{GeV}$, thus lower dijet mass events are rejected. Also only events where leading and subleading jet are in

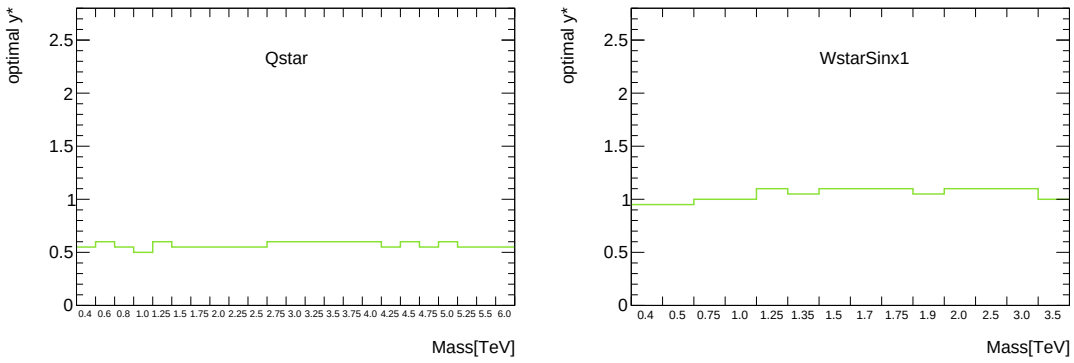

(a) Excited Quark **(b)** W^* ($\sin\theta = 1$)

Figure 5.7: Optimal $|y^*|$ cut for different pole masses.

the central region $|y| < 2.8$ of the detector, where the jet energy resolution is superior, are kept.

SENSITIVITY ENHANCEMENT: New Physics signals have a different rapidity distribution compared to Standard Model production (cf. Sec. 5.1). To increase the sensitivity to New Physics a cut on the absolute rapidity difference $|y^*|$ is employed. Only events with $|y^*| < 0.6$ are kept. This numerical value was found to be optimal by comparing the impact of this cut on the number of signal events s and background events b. The sensitivity was calculated as $\frac{s}{\sqrt{b}}$. The determination of the optimal $|y^*|$cut was performed using data and simulated signal events. The optimal value obtained from this approach is shown in Fig. 5.7(a) for excited quark, and in Fig. 5.7(b) for W^* ($\sin\theta = 1$). For all models and masses the optimal cut value is found to be approximately $|y^*| < 0.6$. Due to the different angular distribution of both variants of W^* the optimal cut for those models is $|y^*| < 1.0$, for simplicity a common cut value of $|y^*| < 0.6$ is used for all models. The optimal values for all models and masses can be found in Appx. C.3.

Apart from the experimental determination of the optimal cut value, one can also use a theoretical ansatz. The dependency of the cross-section on y^* is known for QCD and signal models up to leading order. By maximizing $\frac{s}{\sqrt{b}}$, one obtains, depending on the model, optimal cut values between 0.66 and 0.78. This rough estimation is only correct to first order, as the signal models use an approximate higher order simulation via parton showers that is accurate to leading order at matrix element level.

In the following the selection criteria are described in detail, assigned to the category explained above. The impact of these cuts is shown in Tab. 5.5 and Tab. 5.6. The numbers in these tables differ quite a bit between the normal stream and the delayed stream. The reason for this is the different shape of events before correcting for prescales. As the delayed stream recorded more

Selection criteria	N_{ev}	rel. remainder[%]
1 (before cuts)	871 647 227	100.00
2 (trigger check)	12 886 319	1.48
3 (after GRL)	9 918 952	1.14
4 (vertex check)	9 918 894	1.14
5 (calorimeter error cut)	9 863 909	1.13
6 (leading jets y cut)	9 422 143	1.08
7 (after ugly jet cut)	8 339 494	0.96
8 (after bad jet cut)	8 334 537	0.96
9 (after jet p_T cut)	7 610 460	0.87
10 (after y^* cut)	4 396 317	0.50
11 (after m_{jj} cut)	4 259 455	0.49

Table 5.5: Cuts applied on the full 2012 data sample (normal stream), showing N_{ev} and the cut efficiency.

Selection criteria	N_{ev}	rel. remainder[%]
1 (before cuts)	417 493 026	100.00
2 (trigger check)	33 967 850	8.14
3 (after GRL)	32 461 435	7.78
4 (vertex check)	32 461 223	7.78
5 (calorimeter error cut)	32 349 156	7.75
6 (leading jets y cut)	32 289 087	7.73
7 (after ugly jet cut)	28 580 208	6.85
8 (after bad jet cut)	28 563 192	6.84
9 (after jet p_T cut)	28 516 483	6.83
10 (after y^* cut)	16 014 278	3.84
11 (after m_{jj} cut)	16 013 126	3.84

Table 5.6: Cuts applied on the full 2012 data sample (delayed stream), showing N_{ev} and the cut efficiency.

events in the lower mass region , than the normal stream. Additionally the effect of the cuts on the debug stream is shown in Tab. 5.7. The debug stream records events for which the calculation in the Event Filter exceeded a timeout. Those events are written to disk and reconstructed later. The trigger decision is then recalculated. In this analysis only one event with $m_{jj} > 3\,\text{TeV}$ is added from the debug stream, which adds up in a bin with a total of 20 events.

The nomenclature in the following description is taken from the above mentioned tables.

1. All events recorded.
2. Keep events that fulfill the trigger combination explained in Sec. 5.2.

Event Quality:

3. Keep events that have been recorded, while the detector and accelerator were in good conditions. That is when the LHC provides stable and colliding beams, with the expected energy per beam. At the same time both ATLAS magnet systems and all subdetectors were ready for data taking [117]. Runs that fulfill these criteria are suitable for physics analysis and are listed in so-called *good runs lists* (GRL).
4. Keep events when the primary vertex has two or more tracks associated. A vertex is defined as the origin of reconstructed tracks. The vertex with the largest scalar sum of transverse momenta of the associated tracks, is called the primary vertex.
5. Keep events that are not affected by specific detector conditions. These contain events that have corrupted information from the tile calorimeter and incomplete events due to busy detector parts.

Kinematic Cuts:

6. Keep events where the leading and subleading jet are within $|y| < 2.8$.

Event Quality:

7. Keep events where leading and subleading jet are not flagged as ugly jets. A jet is called ugly, when the fraction of energy deposited in the scintillators between tile calorimeter barrel and end cap exceeds 50 %. Those jets are rejected, as the energy measurement in this gap is known to be inaccurate. In addition jets are called ugly if the BCH_CORR_CELL variable exceeds 50 %. This variable is an automatic compensation for the energy lost in dead calorimeter cells. If this correction is large, the total energy of a jet is also inaccurately measured.
8. Keep events where leading and subleading jet are not flagged as bad jets. Jets are called bad, when the energy deposit in the calorimeter associated to the jet is not originating from a real jet. Those deposits can originate from hardware problems, accelerator effects or cosmic radiation. A combination of several variables using the energy fraction in different regions of the calorimeters is used to identify those bad jets.

Kinematic Cuts:

9. Keep events where the leading and subleading jet transverse momentum exceeds 50 GeV. This eliminates the impact from additional pp collisions on the energy of the leading and subleading jet.

Sensitivity Enhancement:

10. Keep events where the rapidity difference between leading and subleading jet fulfills $|y^*|<0.6$. This increases the sensitivity to New Physics signals, by suppressing background from standard model processes.

Kinematic Cuts:

11. Keep events with an invariant dijet mass $m_{jj} > 253\,\text{GeV}$, to avoid a bias from the trigger selection.

Selection criteria	N_{ev}	rel. remainder[%]
1 (before cuts)	3124	100.00
2 (trigger check)	140	4.48
3 (after GRL)	57	1.82
4 (vertex check)	57	1.82
5 (calorimeter error cut)	53	1.70
6 (leading jets y cut)	53	1.70
7 (after ugly jet cut)	48	1.54
8 (after bad jet cut)	48	1.54
9 (after jet p_T cut)	48	1.54
10 (after y^* cut)	24	0.77
11 (after m_{jj} cut)	24	0.77

Table 5.7: Cuts applied on the full 2012 data sample (debug stream), showing N_{ev} and the cut efficiency.

Kinematic Distributions

This section summarizes the kinematic distribution of events used in this analysis. After applying the analysis cuts on data and on simulated events the following distributions are obtained. The simulated events are scaled to an luminosity that is equal to the one recorded in data of $\mathcal{L} = 18.4\,\text{fb}^{-1}$, which is the reduced luminosity not affected by the data availability problem. In Fig. 5.8 the pseudo-rapidity distribution for leading jet (left) and subleading jet (right) is shown. The black points shown represent events from data. Effects introduced by the detector acceptances and efficiencies are simulated in the MC sample labeled *with detector simulation*. For comparison a MC sample with (red line) and without (green line) these effects is shown in the

Figures. In the distribution of the pseudo-rapidities one can see that the effect of the detector simulation is only small. The largest differences can be seen when comparing data to simulation. The simulated number of events is approximately 130-140 % of the observed events in data. This can be explained by the α_s order of the simulation. The shown simulation uses only terms in leading order. The next-to-leading order effects manifest as soft radiation, which lowers the measured dijet mass. Thus more events fall below the selection cut on m_{jj} and are lost in this comparison. The effect is fairly flat in pseudo-rapidity, which gives a flat ratio, that is only shifted by a constant value.

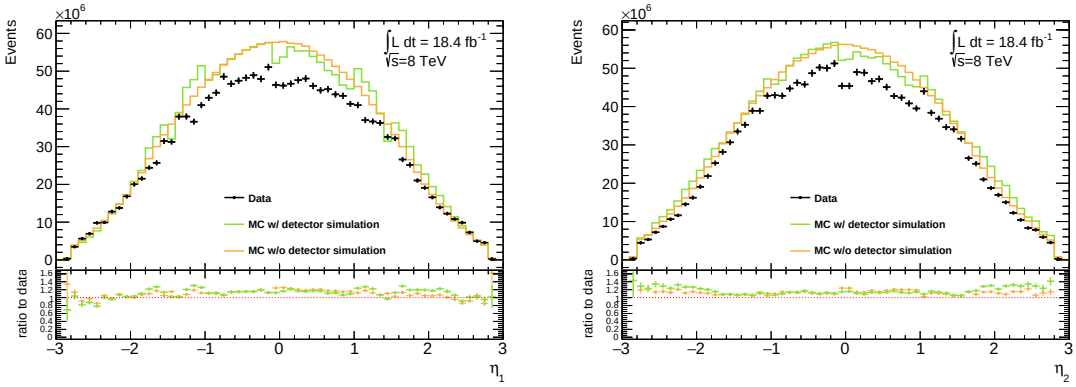

(a) Leading jet **(b)** Subleading jet

Figure 5.8: Distribution of Pseudo-rapidity η in data events and simulated events, with and without detector simulation.

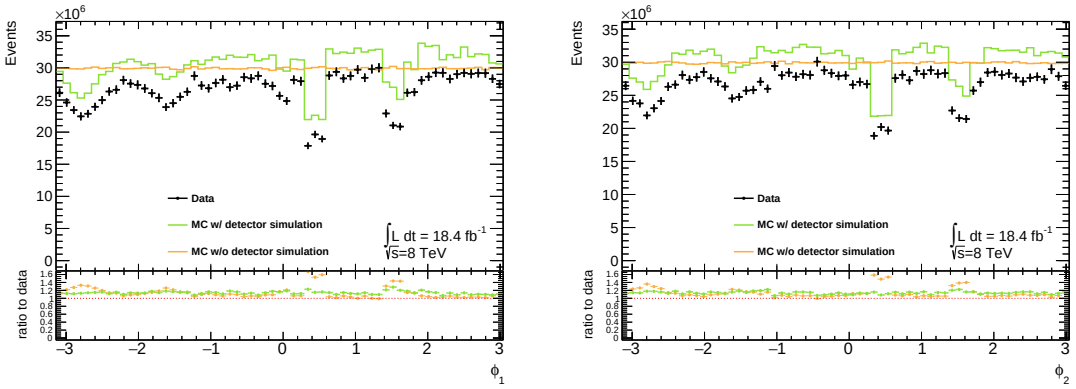

(a) Leading jet **(b)** Subleading jet

Figure 5.9: Distribution of azimuthal angle ϕ in data events and simulated events, with and without detector simulation.

The distribution of leading (left) and subleading (right) jet in ϕ is shown in Fig. 5.9. The same shift between data and simulation is observed as for the pseudo rapidities. In addition the data

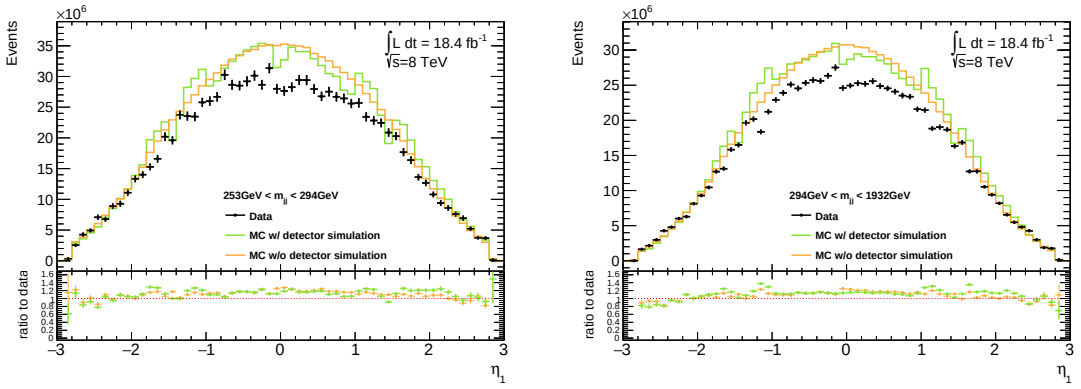

(a) $253\,\text{GeV} < m_{jj} < 294\,\text{GeV}$ **(b)** $294\,\text{GeV} < m_{jj} < 1932\,\text{GeV}$

Figure 5.10: Distribution of Pseudo-rapidity η of leading jet in data events and simulated events, with and without detector simulation.

distribution shows a structure; for some values of ϕ a low number of events is seen. This can be explained by tile calorimeter regions that have been non-operational for some fraction of time during data taking as explained in Sec. 4.3.2. The samples used here do not incorporate this effect as they have been produced prior to data taking. To obtain a reasonable description the effect of non-operational modules has been simulated by removing jets according to the position of the jet and the fraction of time, the corresponding module was inactive. The simulation of this effect was applied to all MC samples used in this thesis. As shown in Fig. 5.9 the shapes between data and MC simulation with detector effect are in agreement, modulo the remaining normalization disagreement.

Due to the strongly falling dijet mass distribution, the comparison of pseudo-rapidity η and azimuthal angle ϕ is dominated by the low mass events. An examination of different mass ranges is performed in these two variables. The rapidity of the leading jet for a dijet mass of $253\,\text{GeV} < m_{jj} < 294\,\text{GeV}$ is shown in Fig. 5.10(a). This low mass region dominates also Fig. 5.8(a), thus the agreement between simulated events and data events is similar. An intermediate mass range of $294\,\text{GeV} < m_{jj} < 1932\,\text{GeV}$ is shown in Fig. 5.10(b), here a similar level of agreement is found, with simulated data overestimating the central pseudo-rapidity $|\eta| < 1.0$ region by up to 20 %. In the highest dijet mass region with $1932\,\text{GeV} < m_{jj}$ shown in Fig. 5.11(a) the description of data events by the simulation is significantly improved. In the central pseudo-rapidity the discrepancy is always smaller than 15 %.

The same separation in dijet mass is also shown for the azimuthal angle ϕ for the lowest mass in Fig. 5.11(b), the intermediate range in Fig. 5.12(a) and the highest mass in Fig. 5.12(b). Here the agreement is independent of the dijet mass always within 20 % for the regions not affected by the non-functional tile calorimeter cells. In the non-functional regions the discrepancy is as large as 40 %.

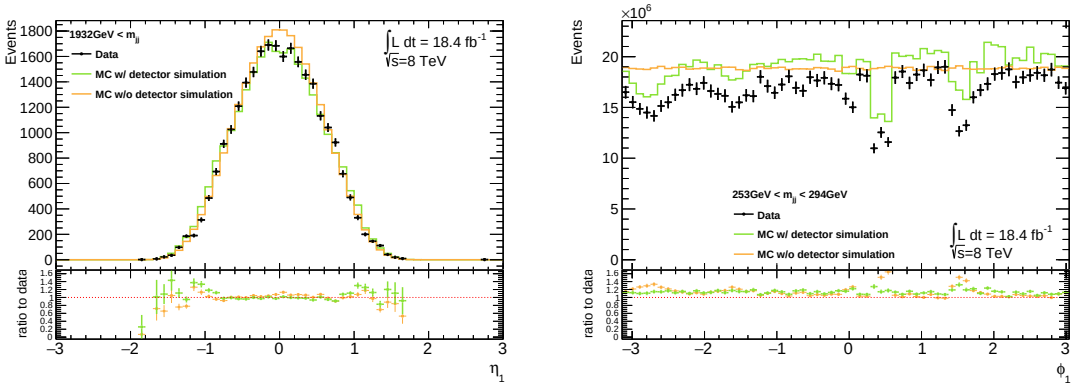

(a) $1932\,\mathrm{GeV} < m_{jj}$ (b) $253\,\mathrm{GeV} < m_{jj} < 294\,\mathrm{GeV}$

Figure 5.11: Distribution of Pseudo-rapidity η (left) and azimuthal angle ϕ (right) of leading jet in data events and simulated events, with and without detector simulation.

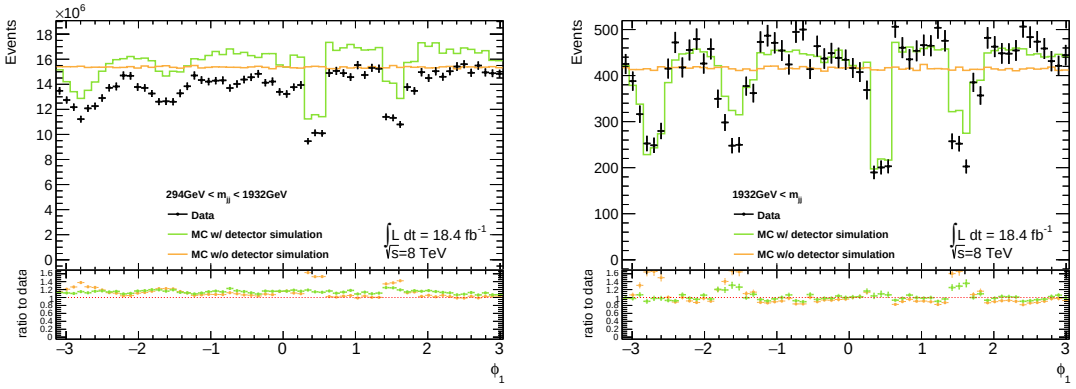

(a) $294\,\mathrm{GeV} < m_{jj} < 1932\,\mathrm{GeV}$ (b) $1932\,\mathrm{GeV} < m_{jj}$

Figure 5.12: Distribution of azimuthal angle ϕ in data events and simulated events, with and without detector simulation.

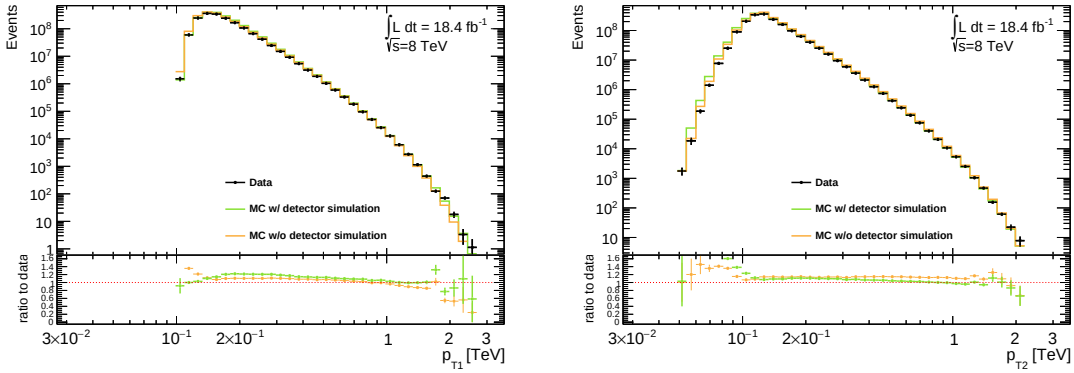

(a) Leading jet **(b)** Subleading jet

Figure 5.13: Distribution of transverse momentum p_T in data events and simulated events, with and without detector simulation.

In Fig. 5.13 the distribution of transverse momentum of leading (left) and subleading (right) jet is shown. There is as already discussed the difference between data and simulation due to the leading order approximation of MC. In addition there is a deviation from a flat ratio between data and simulation in the lowest and highest p_T regimes. In the highest p_T regime, the description of the PDFs can influence this distribution. For those particular values of x the knowledge of the PDFs is still poor, and the used PDF for the simulation has large uncertainties. For the lowest p_T region the influence of pileup can influence the spectrum. As the description of pileup is not optimal in simulated data, a discrepancy between data and simulation is not surprising.

Instabilities in the detector operation and hence a jet calibration that might change with time, can have an influence on the dijet mass spectrum. In Fig. 5.14 the dijet mass is shown as a function of the time of data recording. Here the run number is shown, which is a unique number that increases with time. Also the average dijet mass in black points is shown, with the red error bars calculated from the root mean square (RMS) of the mass distribution. The average and the RMS is stable with time.

The distribution used to search for New Physics in this analysis, the dijet mass, is shown in Fig. 5.15(a). Again a clear difference between simulation and data is seen. The comparison in the m_{jj} distribution shows a slope in the ratio between data and simulated events. The formerly mentioned higher order effects have the biggest impact in the lower mass regime. For increasing masses this effect decreases.

The effect of the cleaning selection criteria is shown in Fig. 5.15(b). For masses below roughly 1 TeV about 10 % of events are removed by the cleaning cuts, independent on the dijet mass. For masses above there is a clear correlation between dijet mass and events removed by the cleaning. As the beam background contribution is mainly at large pseudo-rapidities and high energy, the

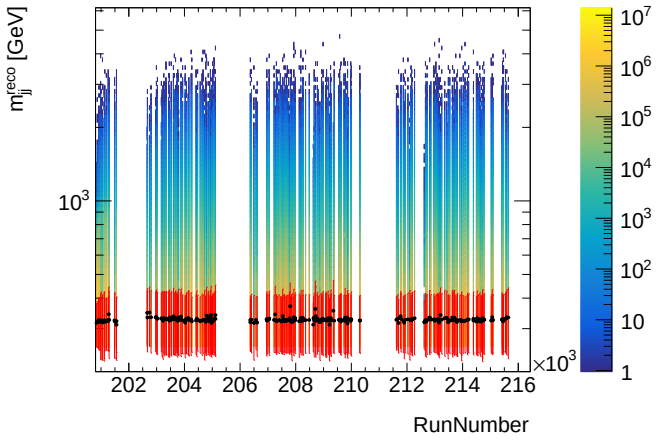

Figure 5.14: Stability of dijet mass over time (RunNumber). Colored area shows the number of events with a given dijet mass and RunNumber. The black dots show the average dijet mass per run, with the red line indicating the root mean square of the dijet mass distribution.

transverse momentum of fake jets will be high and thus the invariant dijet mass of these events is large.

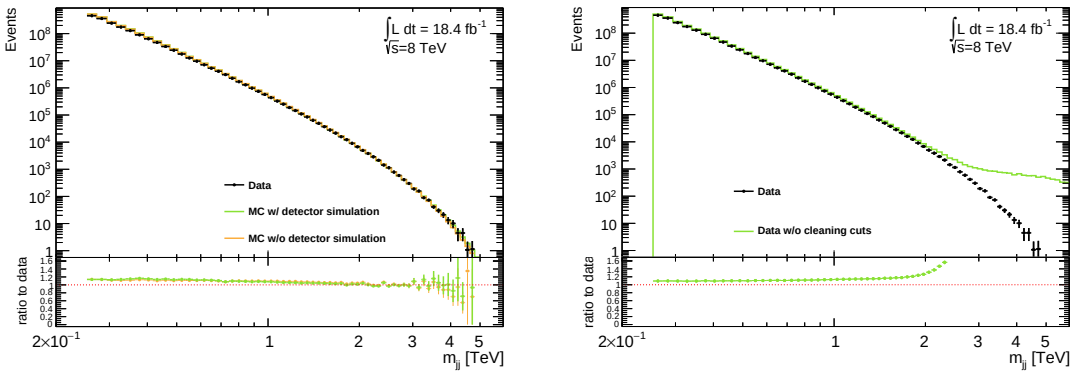

(a) Comparison with simulation

(b) Cleaning cuts

Figure 5.15: Distribution of invariant dijet mass m_{jj} in data events and simulated events, with and without detector simulation (left). Comparison of dijet mass with and without cleaning cuts applied (right). The uncertainties shown for data are of statistical nature only.

BACKGROUND ESTIMATION

To search for deviations of the measured spectrum to expectations, an estimation of the standard model background is mandatory. The most recent theory predictions give a spectrum known up to next-to-leading order in α_S. This is not sufficient to find small deviations in the data spectrum. Thus for this analysis a data-driven approach was used to extract a background expectation. In the history of dijet analyses, a large variety of semi-empirical functions has been used to estimate the background. For a detailed overview see [118]. With increasing range in m_{jj} and increasing integrated luminosity, the number of free parameters in the fit function did also increase.

The latest results covered a range of roughly 4 TeV in m_{jj} and consisted of up to $20\,\text{fb}^{-1}$ (see [119, 120]). Those results used the following four parameter function to estimate the background:

$$f(x) = p_1(1-x)^{p_2}x^{p_3+p_4\ln x} \tag{5.11}$$

Where p_i are free parameters of the fit and $x = m_{jj}/\sqrt{s}$, with the center of mass energy of $\sqrt{s} = 8\,\text{TeV}$. In the course of this analysis it was found, that if the mass range is extended to lower masses than 1 TeV, this four parameter function is not the optimal function to describe the full spectrum. This lead to the introduction of a fifth parameter in the fit function, that is then given as:

$$f(x) = p_1(1-x)^{p_2}x^{p_3+p_4\ln x+p_5\ln^2 x} \tag{5.12}$$

It was found that both functions gave a similar fit performance for a smaller dataset of approximately $5\,\text{fb}^{-1}$, while for increasing luminosity the five parameter function is able to fit to the data easier (see [114]).

Fitting the Spectrum

Fitting a function to a given spectrum always involves minimizing some functional, that describes the level of agreement between data points and the function to fit.

The most common fitting approach is the χ^2 minimization, which uses Pearson's χ^2 defined as follow (see [121]):

$$\chi^2(\vec{o},\vec{e}) = \sum_i \frac{(e_i - o_i)^2}{e_i} \tag{5.13}$$

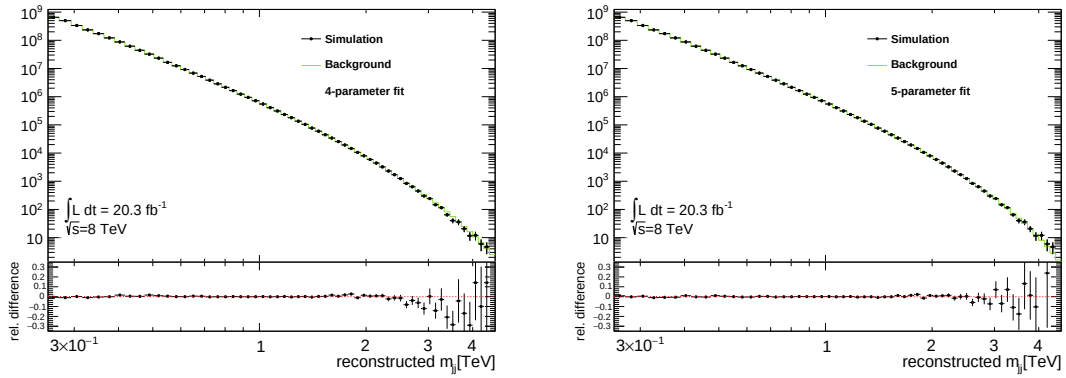

(a) 4 parameter function

(b) 5 parameter function

Figure 5.16: Functions fitted to MC (upper panel) and relative difference (lower panel).

Where o_i is the number of events observed in a given bin i and e_i the expectation of events in this bin. Each term in the sum is the squared difference between observed and expected events divided by the statistical uncertainty of the expectation. Here the relation for the statistical uncertainty $\Delta e = \sqrt{e}$ is used, which only holds for large number of events and thus Gaussian distributed variables. In the case of a large number of events, each summand gives the significance of the deviation between observed and expected events.

In this analysis the uncertainties are Gaussian in the regime below 3 TeV, where $\mathcal{O}(100)$ events are observed. For events with a larger m_{jj}, this approximation is not accurate. Thus for this spectrum a different functional has to be minimized.

The following functional, the so-called *log likelihood*, takes into account the Poisson nature of the process measured:

$$F(\vec{o}, \vec{e}) = -\sum_i \log\left(\text{PoissonI}(o_i, e_i)\right) \tag{5.14}$$

Here *PoissonI* is a function provided by *ROOT* [95], that calculates the value of the probability density function for a Poisson process with a given expectation value e_i for an integer number of measured events o_i.

To estimate the suitability of the four and five parameter fit functions, both options have been tested on simulated and real events. The dijet mass spectrum from simulated events is adjusted to represent the same statistical power as seen in data. To achieve this, the shape of the spectrum from simulation is distorted by drawing a random number from a Poisson distribution with the mean value from simulation and the same statistical power as observed in data.

The results of a fit to simulated events can be seen in Fig. 5.16(a) for the four parameter function and in Fig. 5.16(b) for the five parameter function. The corresponding fit quality in

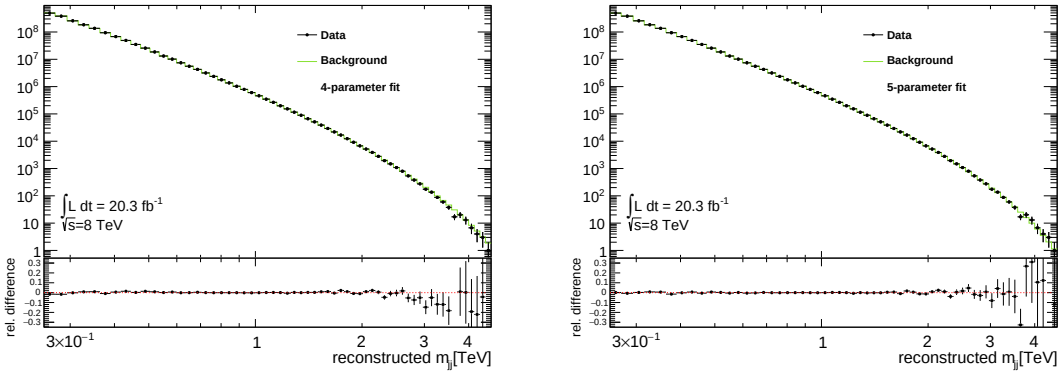

(a) 4 parameter function

(b) 5 parameter function

Figure 5.17: Functions fitted to data (upper panel) and relative difference (lower panel).

terms of reduced χ^2 is 1.47 for the four parameter function and 0.84 for the five parameter function. In the upper panel of the Figures simulated events are overlaid with the fit function. In the lower panel the relative difference between those two is shown. The agreement between fit and simulated events is always better than 10 %, for dijet masses below 3 TeV.

A similar agreement can be seen for the fit to data in Fig. 5.17(a) and Fig. 5.17(b). The final fit values p_i for the fit with the five parameter function to data are

$$\vec{p} = (7.25, 10.6, 3.00, -0.781, -0.0989) \tag{5.15}$$

with a statistical uncertainty on the parameters of less than 1 % each. For this fit a reduced χ^2 of 0.87 is obtained, while using 55 degrees of freedom.

For data and simulation the general conclusion is similar. In the high mass tail the four parameter function is not able to describe the dijet mass distribution well, and gives always more events than seen in data or simulation. The five parameter function is able to describe the spectrum from simulation or data over the full range in dijet mass for the full luminosity of $L = 20.3\,fb^{-1}$. The functional form is also not able to hide narrow resonances by adapting to its shape. Exemplary in Fig. 5.18 the injection of a generic 2 TeV resonance decaying in quark and anti-quark on top of background from data. The figure shows the significance of the discrepancy between data and background fit in terms of Gaussian standard deviations. With increasing cross-section of the injected signal a number of consecutive bins with an excess of events is seen. The significances for the fluctuations in data far from the injected signal are only weakly affected by this.

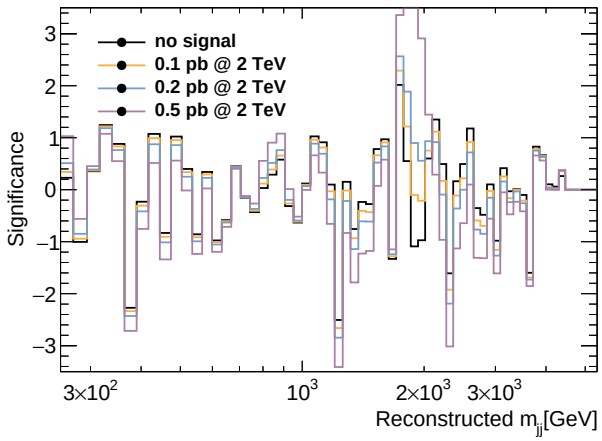

Figure 5.18: Significance of deviation between background from fit and data with different amount of signal imposed. The signal is a generic 2 TeV resonance decaying in quark and anti-quark.

As such the fit function is suited to describe the background while keeping sensitivity to resonance like features. A more detailed and quantitative comparison follows in the search phase section.

SEARCH FOR NEW PHYSICS

The method to search for New Physics in this analysis is divided in two parts. First deviations between observations and predictions are studied. If there are no significant deviations, limits on the scales or masses of the New Physics phenomena are set.

To search for deviations in the spectrum there are several possibilities. One can compare the overall agreement by defining a test statistic t, that compares two distributions. Common test statistics are the χ^2 statistics and the $\log L$ statistics, as defined in Eqn. 5.13 and Eqn. 5.14.

To make a qualitative statement about the agreement of data and expectations, the test statistics is calculated. To extract information on how likely it is to observe a disagreement as large as observed, pseudo experiments are used. Those are produced from data spectra, where in each bin a new bin content is drawn from a Poisson distribution with a mean equal to the expected entries from the fit. This assumes, that the fit result is the best estimate of the real number of events. For each of those pseudo experiments the test statistics is calculated. For a large

number of pseudo experiments the distribution $f(t)$ of the chosen test statistics is obtained. The probability or p-value for a test statistic t_0 as obtained in data is then:

$$p = \int_{t_0}^{\infty} f(t)dt \tag{5.16}$$

A p-value can be used to rule out the null hypothesis if $p < \alpha$. By construction this also gives the probability to falsely exclude the null hypothesis (or the Type I error) to be α. In the search phase the p-value is not used to exclude the null hypothesis or claim a discovery. If the p-value is very small, systematic uncertainties would have to be considered, before any discovery could be claimed. In this analysis the p-value is used to show that there is no sign of New Physics, before setting limits on model parameters.

The p-values calculated here can also be used to show if a function is able to fit to a spectrum reasonably. The comparison of the four and five parameter fits can be done in terms of p-values. In Fig. 5.19(a) and Fig. 5.19(b) the χ^2 test statistics for the four and five parameter functions is shown for simulated events. For illustration purposes instead of χ^2, one minus the exponential of χ^2 is shown. This allows for the same interpretation of the p-value, as the integral from the observed value to infinity, while also expecting a Gaussian distributed test statistics. The very low p-value of $p = 0.06$ for the four parameter function shows, that this function is not able to adequately describe the spectrum. In contrast, the five parameter function has a p-value of $p = 0.68$, which show that this function can be used to describe the spectrum.

The same trend can be seen for the $\log L$ statistics in Fig. 5.20(a) and Fig. 5.20(b).

This shows that the four parameter function cannot describe the data spectrum, while the five parameter function can. This could be due to the nature of the QCD spectrum, which cannot be described by this four parameter function. The same test statistics have been compared for a fit to data. In Fig. 5.21(a) and Fig. 5.21(b) the χ^2 test statistics for a fit to data is shown. In Fig. 5.22(a) and Fig. 5.22(b) the corresponding $\log L$ statistics is shown. Here the p-values show a similar trend as for the fit to simulated events, favoring the five parameter fit function. This shows that the four parameter function is not suitable to fit the QCD spectrum over a large range in m_{jj} with a very large number of events as in $20\,fb^{-1}$.

In the following analysis the four parameter function is thus omitted and only results obtained with the five parameter functions are used.

The presented test statistics are insensitive to shape differences and are thus not able to make a statement about resonances in data.

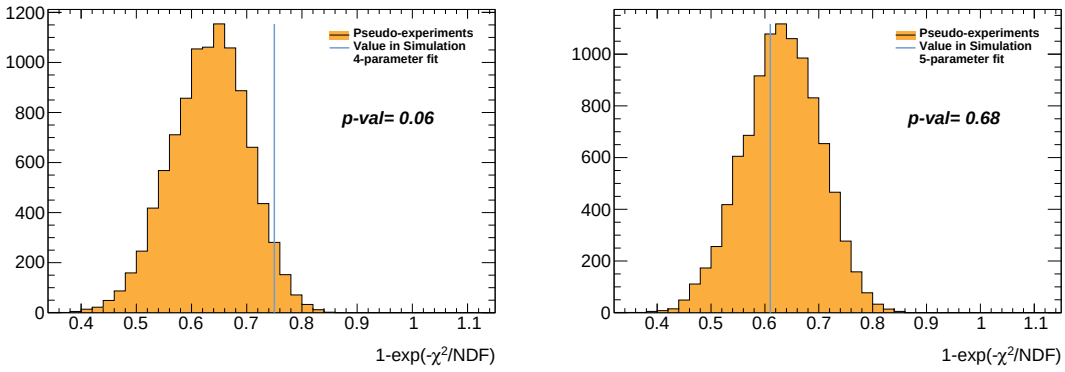

(a) Four parameter function **(b)** Five parameter function

Figure 5.19: Pearson's χ^2 statistics for a fit to MC.

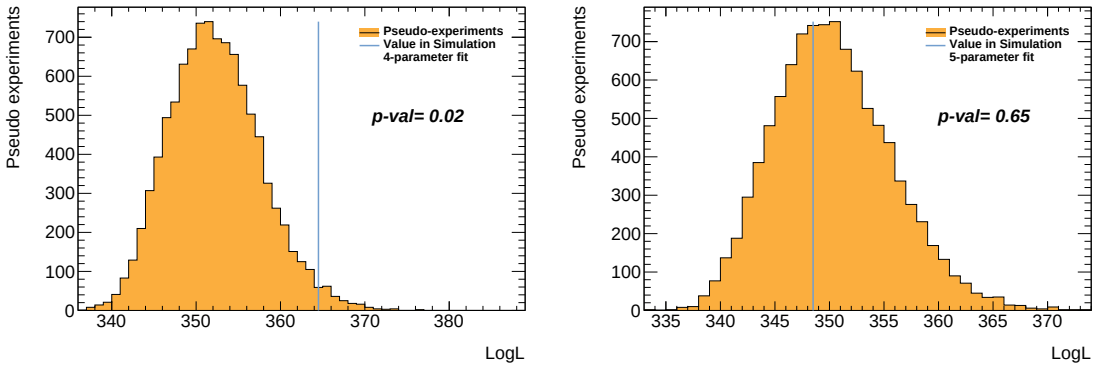

(a) Four parameter function **(b)** Five parameter function

Figure 5.20: Poisson log likelihood statistics for a fit to MC.

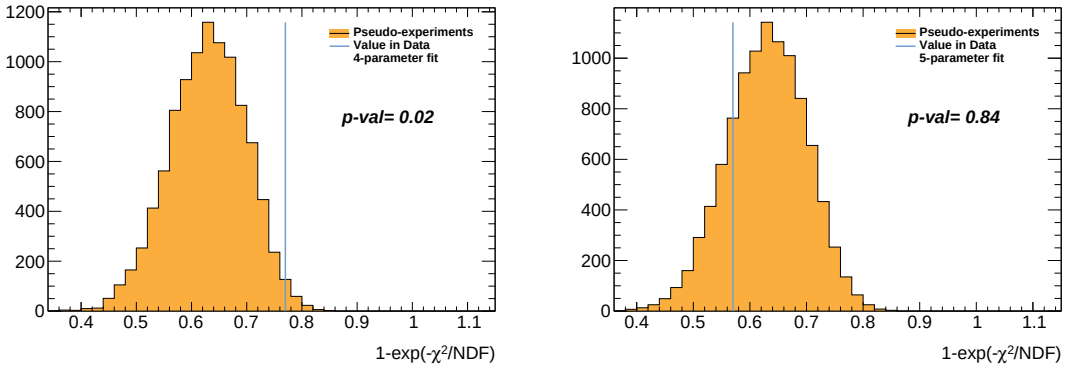

(a) Four parameter function **(b)** Five parameter function

Figure 5.21: Pearson's χ^2 statistics for a fit to data.

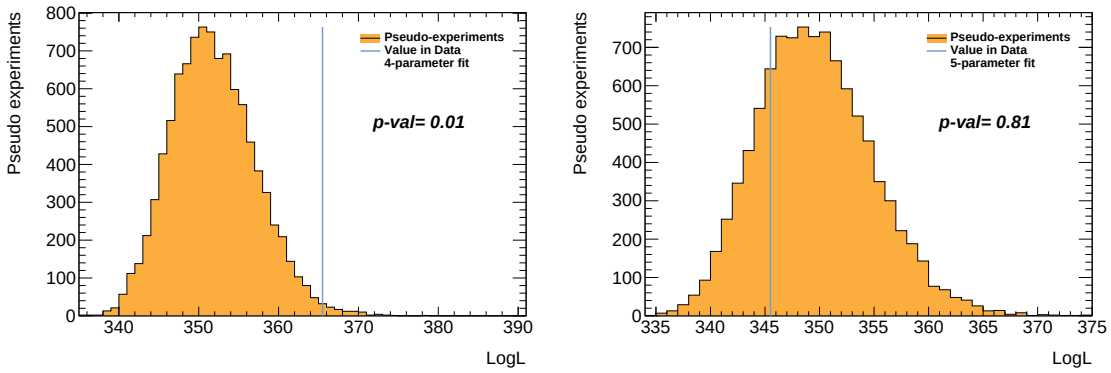

(a) Four parameter function

(b) Five parameter function

Figure 5.22: Poisson log likelihood statistics for a fit to data.

BumpHunter

The so-called BumpHunter algorithm is a hypertest that is able to find consecutive excesses or deficits comparing two distributions (see [122]). In this analysis the algorithm passes the following steps.

1. Choose interval i

2. In interval i calculate probability according to Poisson statistics to find a larger excess than seen between expectation and data, when d is the number of events in data and b is the number of expected events:

$$P(d,b) = \begin{cases} 1, & d \leqslant b \\ \sum_{n=d}^{\infty} \frac{b^n}{n!} e^{-b}, & d > b \end{cases}$$

   As this analysis searches for excesses only the case with less events observed than expected is ignored.

3. Repeat steps 1. and 2. until all possible intervals (position and size) are tested.

4. The test statistics is then:

$$t = -\log\left(\min_i \left(P_i(d,b)\right)\right)$$

   Where P_i are the probabilities obtained from step 2. for interval i.

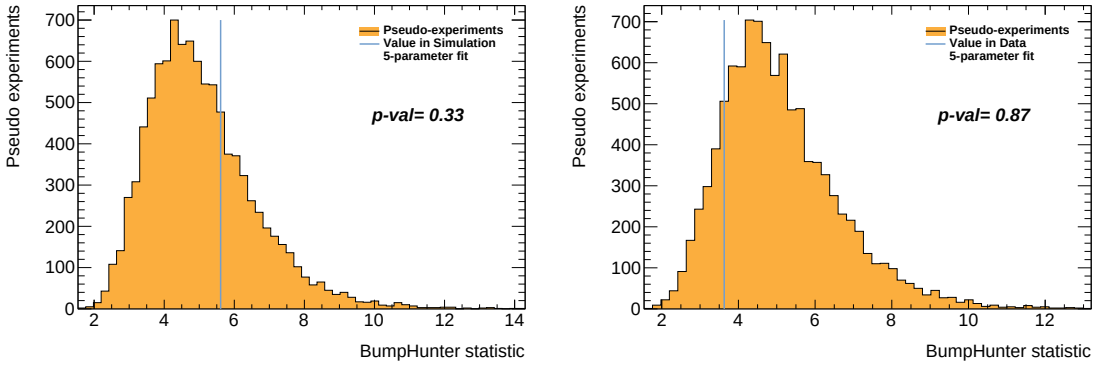

(a) Simulation **(b)** Data

Figure 5.23: BUMPHUNTER statistics.

The obtained test statistics t is then used to calculate a p-value as defined in Eqn. 5.16, by performing the same procedure for a set of pseudo experiments and finding the fraction of experiments that gives a larger test statistics than data. The p-value obtained is shown in Fig. 5.23.

The advantage of the BUMPHUNTER is that by construction the so-called *look elsewhere effect* (LEE) is avoided. The LEE [123] occurs in counting experiments with more than one bin or kinematic region. After observing a discrepancy in data one could construct a test statistics that calculates a p-value only in the discrepant interval. Like this the p-value will be very small, as the pseudo experiments will mainly fluctuate less extreme. This so-called *local p-value* is misleading. As in a large number of bins it is very likely to find a few extreme deviations. To obtain a realistic p-value, one has to have an unbiased view on the whole spectrum. The BUMPHUNTER takes this effect into account, by calculating the test statistics in every possible combination of adjacent bins. This gives an unbiased p-value estimate.

A visualization of the agreement between data and fit can be seen in Fig. 5.24. In the upper panel the data is shown together with the five parameter function fitted to data. Additionally an excited quark signal with three different masses is overlaid. The middle panel shows the relative difference between data and fit, with the same signals overlaid. In the third panel the significance of deviations is shown. Following [124], this panel shows positive significances if more data than background is observed, and negative significances vice-versa. The significance itself is calculated from the Poisson probability to find an excess that is at least as large as the observed one. This probability is then translated in a significance according to the Gaussian distribution.

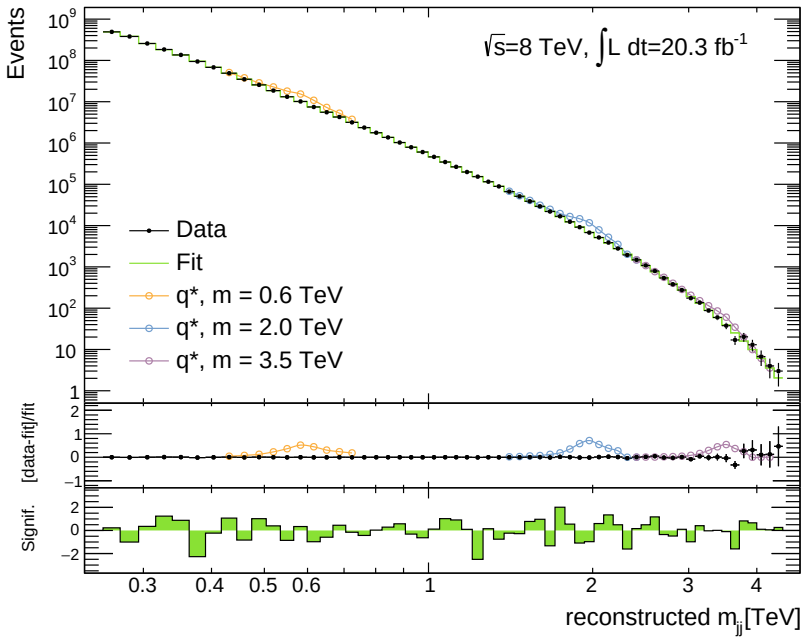

Figure 5.24: Dijet mass spectrum with excited quark signals overlaid (upper panel). Background from five parameter function fitted to data. Residuals of fit to data with signals overlaid (mid panel). Significance of deviations between data and fit (lower panel).

Limit Setting Procedure

No evidence for New Physics has been found. To give a quantitative statement involving different models of New Physics a limit setting procedure is followed. This leads to exclusion limits on cross section times acceptance and upper limits on masses or scales for New Physics. Commonly two approaches are used to set limits, the Frequentist and the Bayesian method. In this section the Bayesian method is used.

The Bayesian limit setting exploits the theorem of Bayes (see [125]), and tries to refine the existent knowledge by performing an experiment.

For this a posterior probability $P(\vec{\lambda}, \vec{\nu}, M|\vec{D})$ is calculated, that shows the knowledge obtained by a measurement, while taking into account prior knowledge about a process. This is the probability to observe the model parameters $\vec{\lambda}$, the nuisance parameters $\vec{\nu}$ (parameterizing the knowledge about the experiment from auxiliary measurements) and the model M given the data $\vec{D}$. This probability can be calculated by:

$$P(\vec{\lambda}, \vec{\nu}, M|\vec{D}) \sim f(\vec{D}|\vec{\lambda}, \vec{\nu}, M) P_0(\vec{\lambda}, \vec{\nu}, M) \tag{5.17}$$

Where $P_0(\vec{\lambda}, \vec{\nu}, M)$ is called the prior, which gives the probability distribution for the model parameters and nuisance parameters obtained from previous experiments. Usually auxiliary measurements, like the jet energy scale uncertainty are designed to give Gaussian distributed uncertainties, thus the prior probability for the nuisance parameters is chosen to be Gaussian. For the model parameters one could include the posterior probabilities from previous searches, instead in this analysis a flat prior for the signal strength is used, which reflects no prior knowledge of the signal strength or cross section.

To obtain a limit on the cross-section of a New Physics signal which is assumed to be present in data, the posterior distribution has to be marginalized. This means that the distribution should be only dependent on the signal strength, and thus one integrates out all remaining parameters. This gives $P(\lambda|\vec{D}, M)$, where λ is the signal strength for a signal in model M. To obtain an 95 % upper limit on the cross section one integrates this remaining posterior distribution:

$$0.95 = \int_0^{\lambda_{\text{upper}}} P(\lambda|\vec{D}, M)\, d\lambda \tag{5.18}$$

This equation is then solved for λ_{upper}, which is the desired upper limit.

In this thesis the Bayesian Analysis Toolkit (BAT) was used (see [126]), which implements the limit setting. To calculate the marginalized function efficiently, a Markov-Chain Monte-Carlo approach is used.

Systematic Uncertainties

In the limit setting various sources of systematic uncertainties are incorporated. Uncertainties due to the energy scale, the fit function, the luminosity, the beam energy and PDF effects are taken into account. Other sources have been studied and found to be negligible.

Jet Energy Scale Uncertainty

The main experimental source of uncertainties is the Jet Energy Scale (JES). For a detailed description see Sec. 4.5. A large number of statistical independent components of the JES uncertainty are provided by the ATLAS performance groups. Those are 56 components from the in-situ methods and 8 components from the η-intercalibration and pileup. It was found, that for most parts of the dijet mass spectrum, there is a negligible impact in the limit between using the full set of uncertainty components and using the sum of all components in quadrature. To reduce the computing time of the limits, a reduced set of 22 components with small residual correlations is used only in the mass region where an impact was seen. For dijet masses above 1 TeV only one component was used, which is the sum of all components in quadrature.

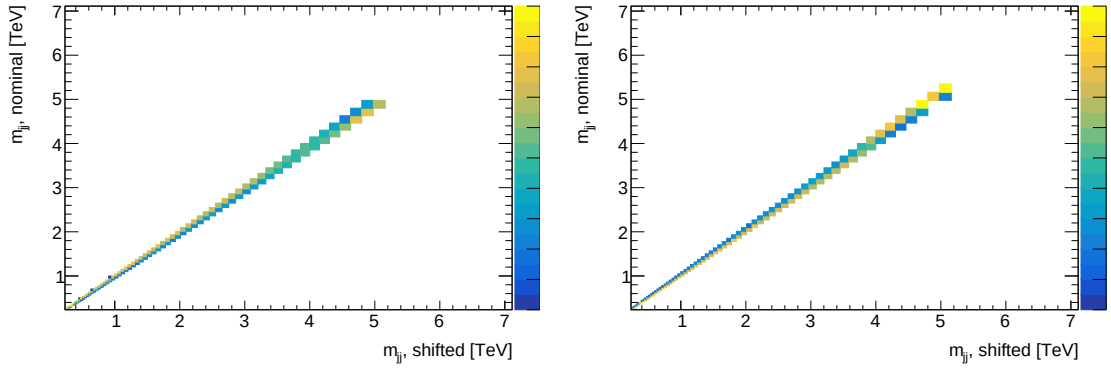

(a) Shift by -1 σ **(b)** Shift by +1 σ

Figure 5.25: Transfer matrices corresponding to the total JES uncertainty for an excited quark with $m = 4000\,\text{GeV}$.

For practical reasons this uncertainty is propagated by transfer matrices. Matrices have been prepared for 13 variations between -3 and +3 σ, for each of the 22 uncertainty component, for each of the total 109 mass points, that have been used to set limits. This gives a total of 31174 matrices. This makes it possible, to shift input signal shapes by an arbitrary combination of different systematic components, as needed by BAT. One example for such a matrix can be seen in Fig. 5.25, which shows the impact of the -1 σ (left) and +1 σ (right) shift of the total JES uncertainty for an excited quark with $m = 4000\,\text{GeV}$.

Fit Uncertainty

As the parameters in the fit function used are highly correlated, it is not possible to use the covariance matrix to estimate an uncertainty of the fit. Alternatively an approach exploiting pseudo experiments is used. The nominal data spectrum is modified by drawing bin-by-bin Poisson variations of the number of events. The function is then fitted to the new spectrum. This procedure is repeated $\mathcal{O}(100)$ times. The spread in terms of root mean square (RMS) of estimated bin contents from the fits is then used as an uncertainty of the fit as shown in Fig. 5.26. The uncertainty is smaller than 1 % for masses below 1.5 TeV and increases up to 30 % for the last bin in data with events available.

Luminosity Uncertainty

The uncertainty from the determination of the luminosity is estimated to 2.8 % [98]. This uncertainty is applied as an overall normalization on the signal templates.

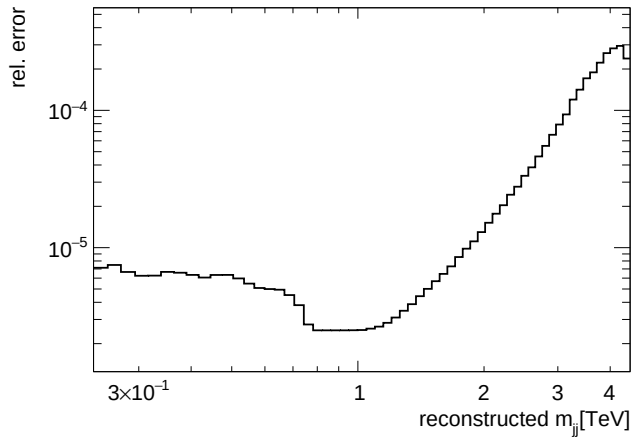

Figure 5.26: Fit uncertainty in data.

Beam Energy Uncertainty

During the proton lead collision runs in early 2013 it was found that the proton beam energy was not exactly 4 TeV (see [127]). This special run was then used to determine the correct proton energy and to estimate an uncertainty on the energy. The measured energy per proton beam was found to be:

$$E = 3988 \pm 5(\text{stat}) \pm 26(\text{syst})\,\text{GeV} \tag{5.19}$$

To estimate the influence on the limit setting, the templates for New Physics samples, which have been produced with an proton beam energy of 4 TeV, have been reweighted. The uncertainty was estimated by evaluating the parton density function at different Bjorken-x values according to different beam energies. The result of this procedure is shown in Fig. 5.27 for a QBH signal with m=5 TeV. The main impact of this change in center of mass energy can be seen in the highest dijet masses.

PDF Uncertainties

For the model dependent limit setting signal samples using different *Parton Density Functions* (PDF) are produced. The uncertainty from choosing a particular PDF (inter-PDF) and from the uncertainty components provided by each PDF group (intra-PDF) have to be taken into account. In this analysis the recommendations from the PDF4LHC group [128] have been used. The envelope covering both inter and intra-PDF effects is used as the total uncertainty from the PDF choice.

For the PDF choice three different PDFs have been used:

CT10: Uses a symmetric Hessian approach, and provides Eigenvectors.

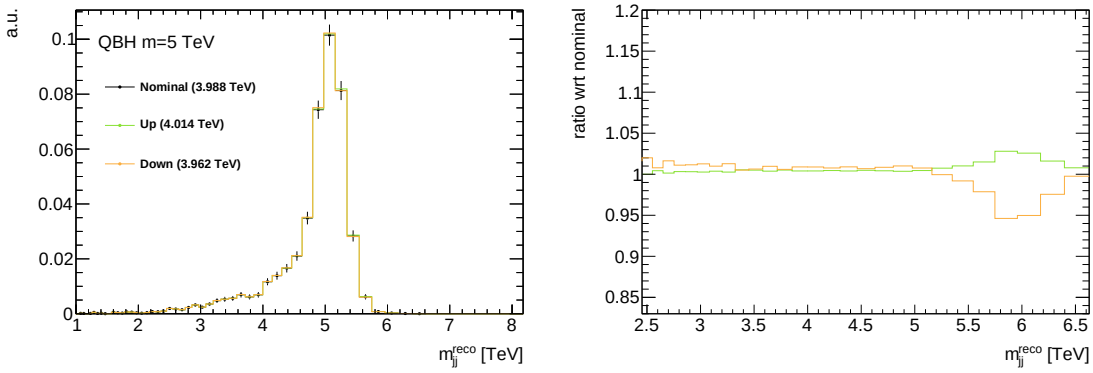

(a) Nominal, up and down variations

(b) Relative difference.

Figure 5.27: Impact of beam energy shift on a QBH signal with m=5000 GeV. Nominal beam energy is compared with 3.988 TeV and 4.014 TeV.

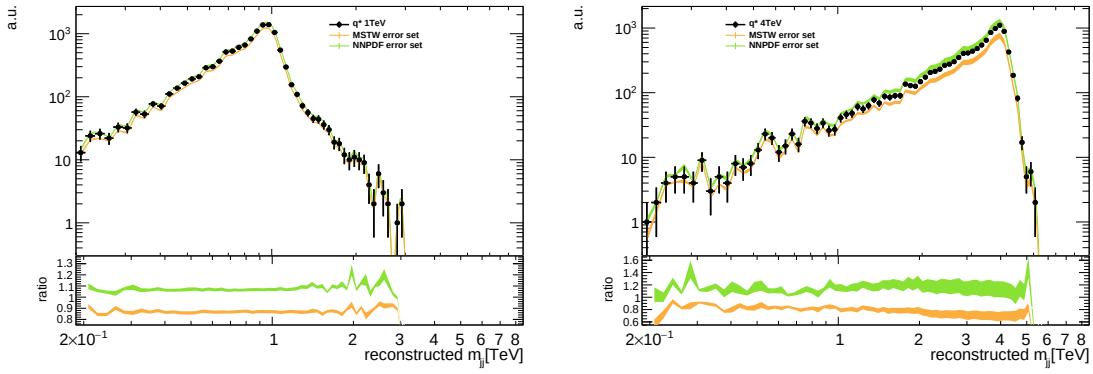

(a) m=1 TeV

(b) m=4 TeV

Figure 5.28: Impact of PDF uncertainty on excited quark signal.

MSTW: Uses an asymmetric Hessian approach, and provides Eigenvectors.

NNPDF: Provides an ensemble of PDFs, standard deviation is used as systematic uncertainty.

To examine the impact of different PDF choices, the signal samples have been reweighted according to the ratio of the parton density evaluated at the PDF of interest and the parton density for the nominal PDF. The obtained systematic uncertainty can be seen in Fig. 5.28 for an excited quark at m=1000 GeV and m=4000 GeV. An analysis of all used signal samples showed, that the choice of PDF has an impact on the normalization, but does not influence the shape of the signal. Thus the uncertainty is applied as an overall normalization changing factor.

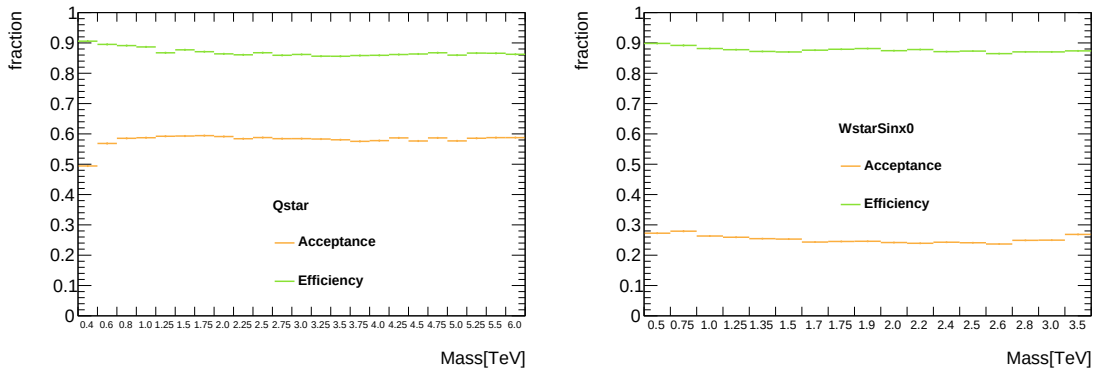

(a) Excited quark **(b)** W^* ($\sin\theta = 0$)

Figure 5.29: Acceptance and efficiency for different pole masses. Statistical uncertainties are shown.

Model-Specific Limits

To set a limit on parameters of a specific model, simulated events according to this model are used. As the effect of non-operational calorimeter regions was not simulated, the inefficiency was emulated similar to the procedure used for the QCD simulation. The impact of non-operational regions is measured as an efficiency and shown for different masses of q^* in Fig. 5.29(a). This efficiency is similar for different models. The number of events remaining after all other selections are applied divided by the total number of events is called acceptance and is also shown for different masses of q^* in Fig. 5.29(a) The acceptance is fairly independent on the pole mass of the New Physics particle at about 58 %, if it is well above the lower dijet mass cut of $m_{jj} > 253\,\text{GeV}$, The acceptance and efficiency vary between models depending on their shape and distribution especially in rapidity. Models like W^* with a large fraction of events outside the rapidity difference $|y^*| < 0.6$ show much smaller acceptances of about 25 % as shown in Fig. 5.29(b). The rapidity difference $|y^*|$ for different models is shown in Fig. 5.30. All models except the W^* model show a similar behavior. The largest number of events is found in the small rapidity difference region. For larger rapidity differences, the number of events decreases. The W^* model shows additionally a low number of events at zero rapidity difference, with the maximum of events around $|y^*| = 0.8$

The dijet mass shape for different models is shown in Fig. 5.31(a) for a pole mass of 1 TeV, in Fig. 5.31(b) for 2 TeV and in Fig. 5.32 for 3 TeV. The signal shape depends crucially on the final state partons. For the color octet with two gluons in the final state, the signal peak is very broad starting from the lowest masses. For high masses this final state becomes a broad resonance, without a clear peak. Contrary the W' final state contains two quarks, which can be reconstructed as a narrow resonance from the low masses, up to the highest ones. The resonances consisting of one quark and gluon show a behavior which is in between these two

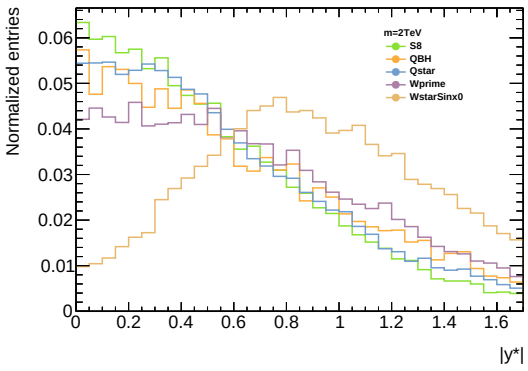

Figure 5.30: Overlay of absolute rapidity difference for signal samples at $m = 2\,\text{TeV}$.

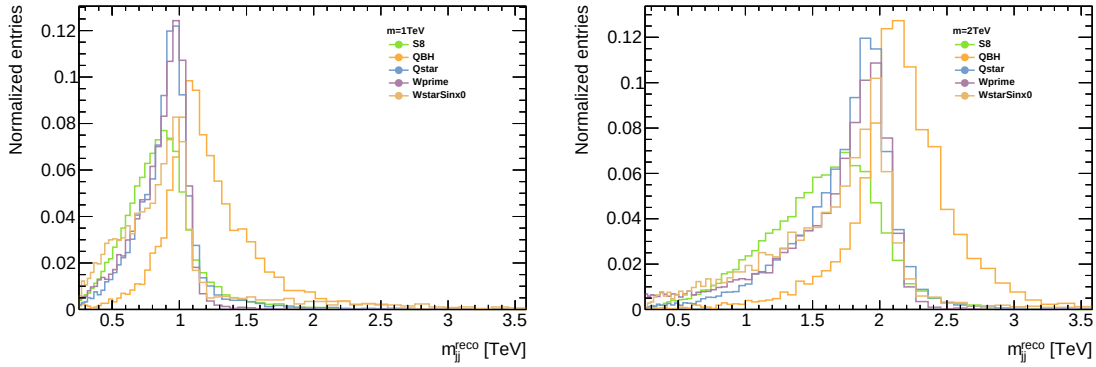

(a) $m = 1\,\text{TeV}$ **(b)** $m = 2\,\text{TeV}$

Figure 5.31: Overlay of signal samples at fixed pole mass.

extremes. Another particular case is the quantum black holes model. Due to the nature of this process the resonance shape is not influenced by PDF effects, hence the resonance peaks at the pole mass, and the shape is narrow for all masses.

The results of the limit setting for specific models are shown in this section. In Fig. 5.33(a) the 95 % CL upper limit on the cross section times acceptance for the excited quark model is shown, for different masses of the hypothetical particle. The dots show the observed limit, which uses the obtained data from the experiment as observed spectrum. This can be compared to the expected limit in dotted line. The expectation is obtained by declaring the background estimation as the observation, hence as a representation of the data. This procedure is repeated 500 times, with a varied background estimation according to a Poisson distribution with the mean value equal to the original background estimation. Those 500 expected limit values form a distribution, which is used to extract symmetric intervals around the median containing 95 %

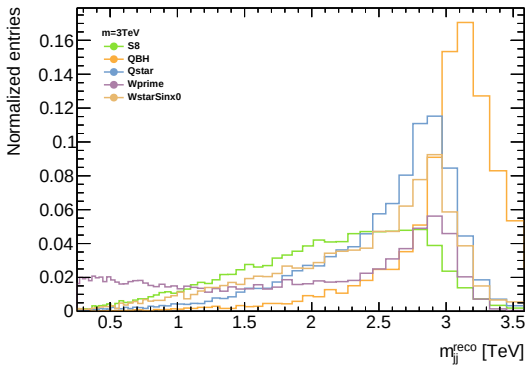

Figure 5.32: Overlay of signal samples at $m = 3\,\text{TeV}$.

(equivalent to 2-σ in a normal distribution) and 68 % (1-σ) of values. The obtained median is shown as the dotted line, while the error band is obtained from the 1 and 2-σ values.

To obtain a limit on the mass of a hypothetical particle, a specific model (especially a coupling strength to quarks/gluons) implementation has to be used. A specific model predicts cross sections dependent on the mass of the particle. When such a model is simulated and all kinematic cuts are applied similar to the data cuts, then an acceptance is obtained, and one can calculate σ x A for the model. This is shown as the orange line in the figures. The crossing point between the expected (observed) upper limit lines and the theory line shows the expected (observed) mass limit. All masses for which the theory line is above the upper limit are thus excluded with 95 % credibility.

The limits for the color octet scalar model are shown in Fig. 5.33(b). Fig. 5.34(a) shows the limit for W′. In Fig. 5.34(b) and Fig. 5.35(a) limits for Quantum Black Holes generated with the QBH generator and the BlackMax generator are shown. Limits for the W* model are shown in Fig. 5.35(b) and Fig. 5.36 for $\sin\theta = 0$ and $\sin\theta = 1$. All mass limits are summarized in Tab. 5.8.

	q*	BlackMax	S8	W* ($\sin\theta = 1$)	W* ($\sin\theta = 0$)	W′	QBH
expected [TeV]	3.90	5.67	2.74	1.66	1.98	2.37	5.75
observed [TeV]	3.96	5.67	2.68	1.59	1.71	2.17	5.75

Table 5.8: Expected and observed mass limits at 95 % CL. For W* ($\sin\theta = 0$) a region between 1.86 TeV and 1.98 TeV is also excluded in the observed limit.

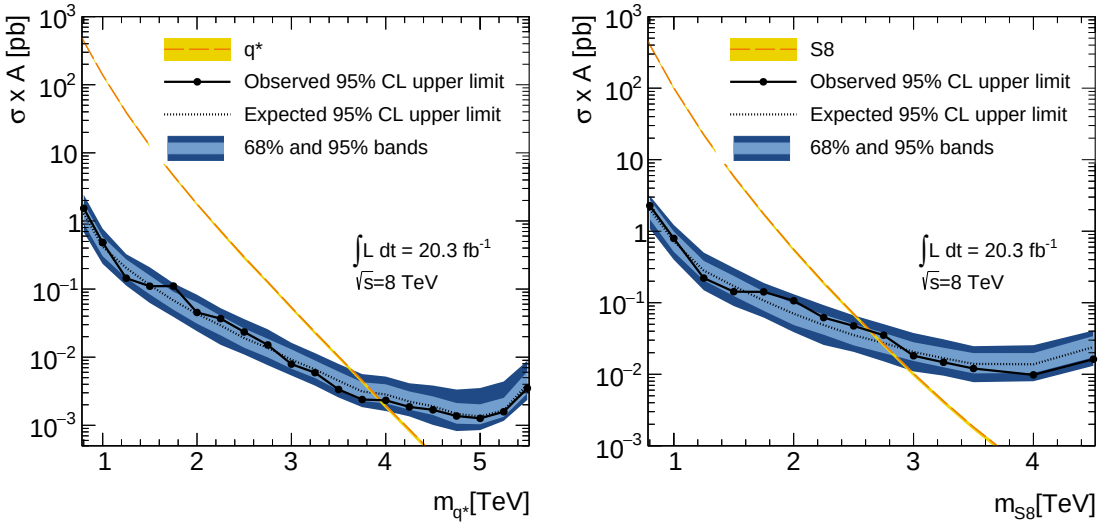

(a) Limits on Excited Quark.

(b) Limits on Color Octet.

Figure 5.33: 95 % CL upper limits for Excited Quark and Color Octet models.

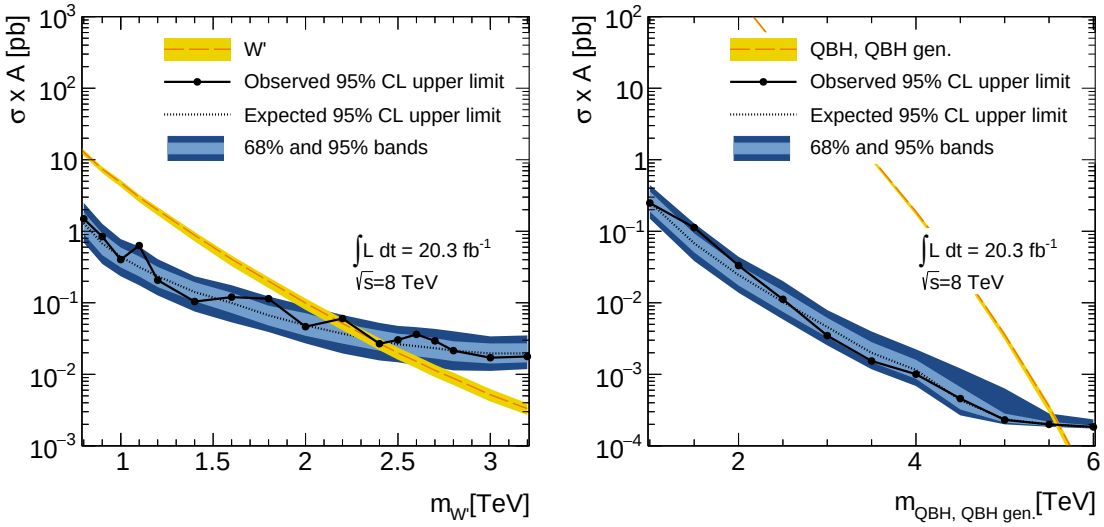

(a) Limits on W′.

(b) Limits on QBH Quantum Black holes.

Figure 5.34: 95 % CL upper limits for W′ and QBH models.

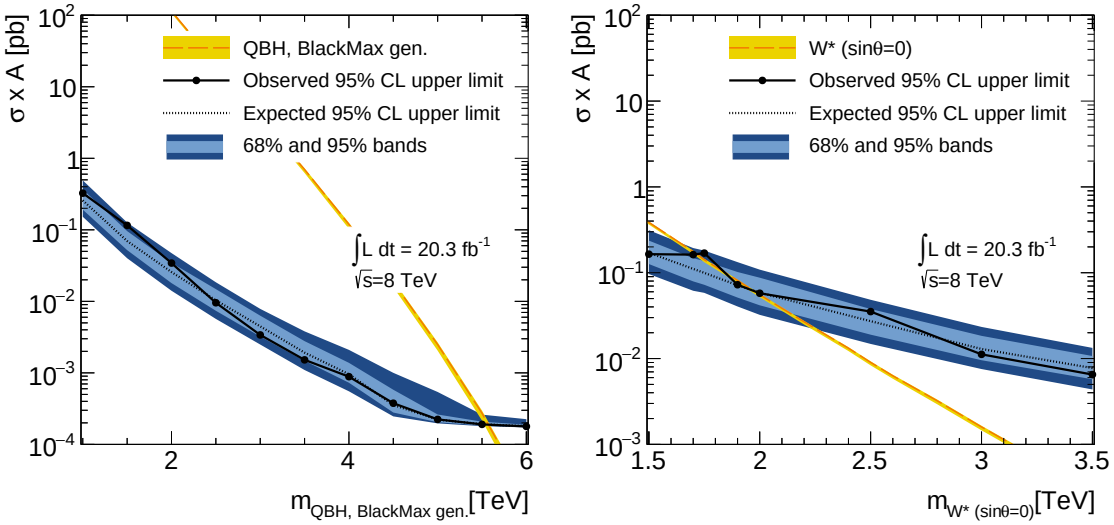

(a) Limits on BlackMax Quantum Black holes.

(b) Limits on W* with $\sin\theta = 0$.

Figure 5.35: 95 % CL upper limits for BlackMax and W* models.

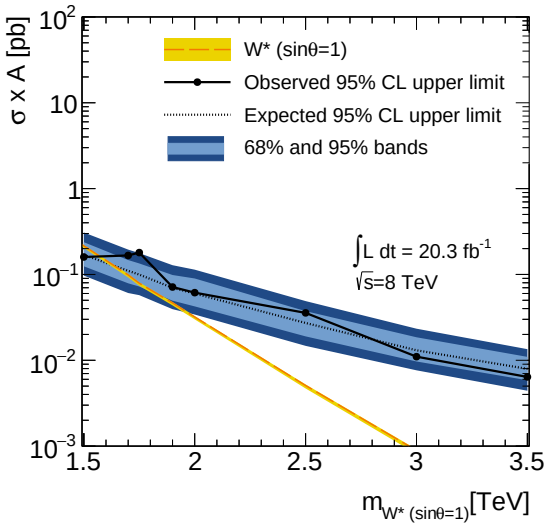

Figure 5.36: 95 % CL upper limits for W* model with $\sin\theta = 1$.

Model-Independent Limits

The limits given in the last section are only valid for the specific models shown. As many different models that have not been tested here show similar features in data, a more model-independent way to set limits is explored. In the following chapter two different types of limits are set, that can be used to obtain a limit on any arbitrary model that gives a resonance like feature in the m_{jj} spectrum. In addition a method is used, that makes it possible to interpret the obtained limits also as limits on the coupling strength, which allows for easier comparison to limits from other experiment with different center of mass energies and different colliding partons.

Gaussian Limits

The simplest possibility to obtain a less model-dependent limit, is by calculating a limit using a Gaussian shaped signal. This is a valid approximation to most signals, as many signals have a Gaussian core. For a signal with a negligible width, one expects a Gaussian signal with a width given by the detector resolution.

As such an analytical signal does not give individual events, some of the formerly used systematic uncertainties are not meaningful. The uncertainty on the PDF choice was omitted, as any information on Bjorken-x values is also not available and not important here. The uncertainty on the beam energy was removed for the same reason.

The uncertainty on the jet energy scale cannot be applied as for the model-dependent limit setting. As the jet energy scale can influence the position of the peak, this has an impact on the limits obtained. Instead of the more involved method of several jet energy scale components, only the relative impact on the position of the mass peak has been examined. It was found that for the range of models used in this analysis, the mean of a signal shifts by up to 0.6 % in m_{jj}. This value was used as an systematic uncertainty for the Gaussian shaped signals.

As the obtained limit depends on the chosen width of the Gaussian, several reasonable widths have been probed. For a resonance width at parton level that is much smaller than the detector resolution, one expects a Gaussian signal with width equal to the detector resolution. Thus the smallest width considered is the detector resolution. In addition larger relative widths of $\frac{\sigma_G}{m_G} = 0.07$, 0.10 and 0.15 have been probed. The resulting 95 % CL limit on $\sigma \times A \times BR$ is shown in Fig. 5.37. All four widths shown give a comparable limit. The limit for the detector resolution shows the largest local variations compared to the larger widths. This can be explained by the ability of a narrow signal to be aligned with fluctuations in data. If such a small signal is probed in a region with a local deficit, a large amount of signal events can be injected without changing the likelihood too much. This gives a stronger limit than the same mass signal with larger width. For the case of a local excess this behavior leads to the opposite effect. If the small width signal is present in the same bins as the excess, then only a small amount of events can be injected

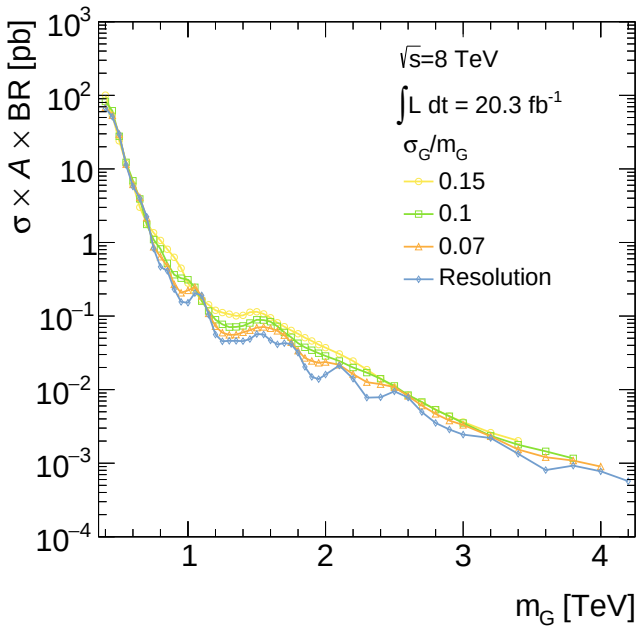

Figure 5.37: 95 % CL upper limits for Gaussian signal shapes.

before the likelihood changes too much. This leads to a weaker limit than obtained for the corresponding larger width signal.

Comparing the limit obtained from the Gaussian signal approach with a limit from a specific model shows that the Gaussian limit gives an conservative estimate underestimating the model dependent limits by up to a factor of 10. This discrepancy is due to the approximation of the signal shape as a Gaussian, while omitting long tails from PDF suppression and parton showering. To overcome these shortcomings a more involved signal model is developed.

Breit-Wigner Type Signals

The method in the former section requires to perform several steps after generating events for a model to study. In this section an approach is shown, for which one only needs to know about the intrinsic width of the resonance and the type of outgoing parton.

This signal type uses the same systematic uncertainties as already discussed in the case of Gaussian shaped signals. The only difference is the generation of the signal. The Breit-Wigner generation follow these steps:

1. Generate initial Breit-Wigner shape according to $f(x, M, \gamma) = \frac{1}{2\pi} \frac{\gamma}{(x-M)^2+\gamma^2/4}$, with M the mass and γ the width of the resonance.

2. Convolute Breit-Wigner with the PDF according to final state partons (gg,qq,qg or $q\bar{q}$). That is the product of the single PDFs.

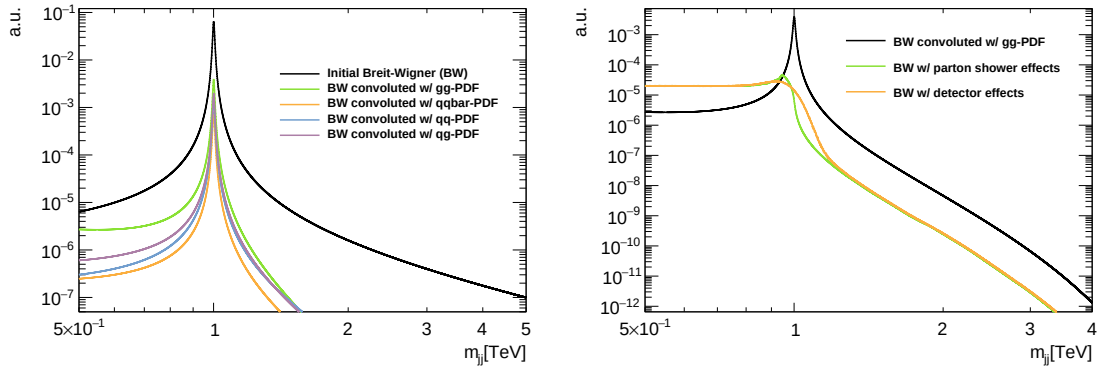

(a) Impact of convolution with different PDFs.

(b) Impact of convolution with parton shower and detector effects on gg-convoluted Breit-Wigner

Figure 5.38: Breit-Wigner signal template at different stages.

3. Convolute the former result with the resolution additionally introduced by the parton showering. This has been calculated from HERWIG. A cross check with PYTHIA gave less conservative limits.

4. Convolute with detector resolution.

Those steps are illustrated in Fig. 5.38. In Fig. 5.38(a) one can clearly see how different PDFs distort the shape of the initial Breit-Wigner. The gg-PDF for example, gives an enhanced low mass tail, compared to the other PDF combinations. The effect of parton showering and detector resolution is shown in Fig. 5.38(b). The parton shower shifts the peak to lower masses, while also enhancing the low mass tail. The additional detector resolution effect smears out remaining kinks in the signal, while changing the shape only slightly.

The obtained signal sample is then used as an input to the limit setting. The resulting 95 % CL limits on $\sigma \times A \times BR$ for a gg resonance and relative widths $\Gamma_{BW}/m_{BW} = 0.005$, 0.01, 0.03 and 0.05 are shown in Fig. 5.39(a). Fig. 5.39(b) shows the corresponding plot for a $q\bar{q}$ resonance. And finally for qg (left) and qq (right) resonance the limits are shown in Fig. 5.40.

One of the choices in the list of steps introduces a model-dependence in this procedure. In a first step where the Breit-Wigner is chosen, several choices are available. The choice in this paper was to use the non-relativistic version of the Breit-Wigner. In PYTHIA and HERWIG the relativistic version is used, which in addition to being relativistic, also takes into account a mass-dependence of the width. For a comparison of the different options see [129]. In PYTHIA the chosen mass is even more sophisticated. There a sum of a relativistic Breit-Wigner with mass dependence, a $1/\hat{s}$ term and a $1/\hat{s}^2$ term are used. All of these terms have coefficients that are model-dependent. The choice in this analysis to use a non-relativistic Breit-Wigner is thus not optimal, as this introduces a non-physical behavior in the low mass region (see [71] Chapter 7.3). Nevertheless this choice was made to have a signal that is as model-independent as possible.

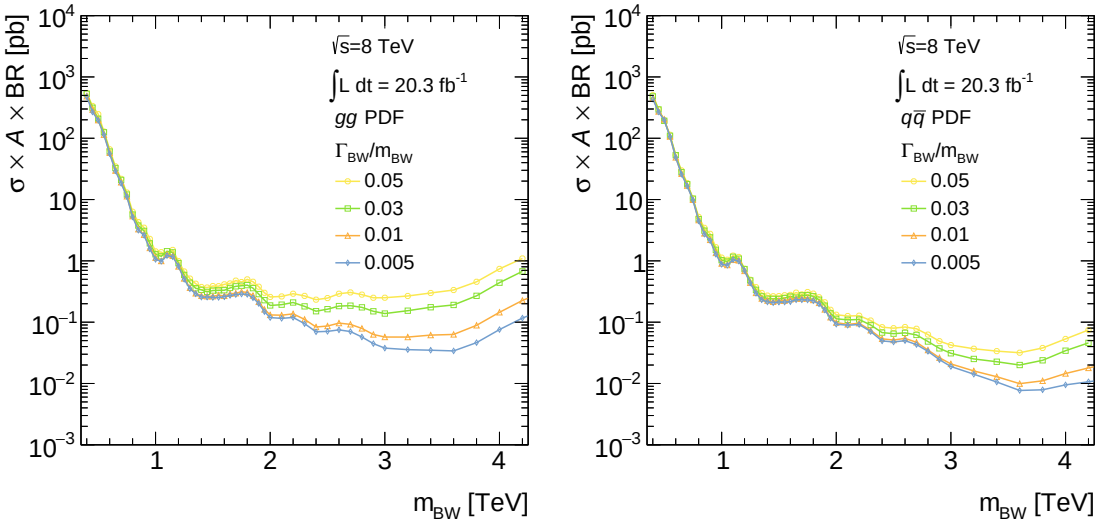

(a) Limits on gg.

(b) Limits on qqbar.

Figure 5.39: 95 % CL upper limits for generic Breit-Wigner for gg and qqbar initial state.

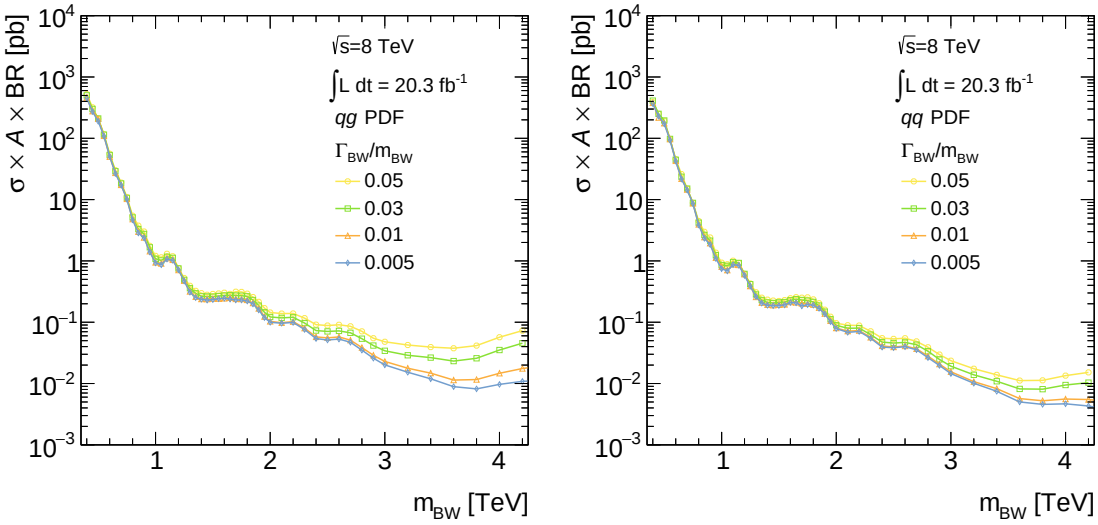

(a) Limits on qg.

(b) Limits on qq.

Figure 5.40: 95 % CL upper limits for generic Breit-Wigner for qg and qq initial state.

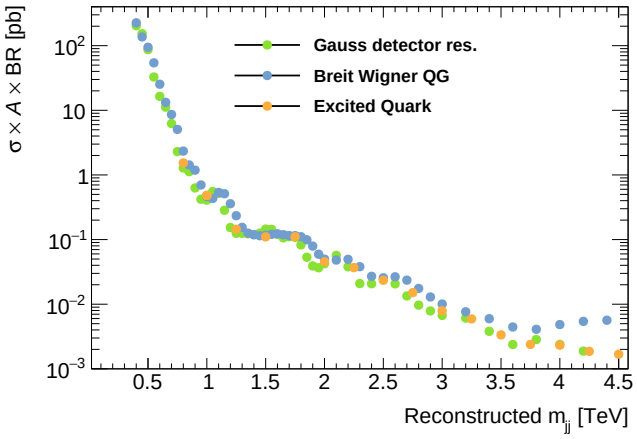

Figure 5.41: 95 % CL upper limits for Excited quark, Gaussian shaped and Breit-Wigner shaped signals. For the Gaussian signals a relative width similar to the detector resolution is assumed, while for the Breit-Wigner type a relative width of $\Gamma_{BW}/m_{BW} = 0.005$ is used.

The resulting limits can be compared to the ones obtained from Gaussian shaped signals, and the ones from a specific model. In Fig. 5.41 the limits for an excited quark are compared to limits from a Gaussian with a relative width comparable to the detector resolution and a Breit-Wigner decaying in quark and gluon with a relative width of $\Gamma_{BW}/m_{BW} = 0.005$. The limits for both model-independent signal shapes are comparable to the one from the excited quark model. For the Gaussian shaped signal the agreement to the limit from the excited quark model is always better than 25 %. For the Breit-Wigner type signal the discrepancy to the excited quark limit is smaller than 25 % for masses up to 3.2 TeV, while for higher masses this discrepancy rises up to a factor of three.

Limits in Coupling-Mass Plane

After decades of resonance searches a large amount of limit plots comparable to the ones shown in this thesis have been produced. A direct comparison between those limits is problematic for several reasons. A change in the center of mass energy changes production cross sections and hence the resulting limit curve. Also different types of experiments like fixed target or proton-antiproton setups give limits which are not easy to compare. One possible way to circumvent this is to set limits in a two dimensional plane in coupling strength versus mass of a resonance [115]. Setting a limit on the coupling strength also motivates the search in lower mass regions, that have been excluded already for the nominal coupling, as shown in this analysis.

To extract a limit on the coupling strength the following steps are performed:

1. Generate Z′ events with the coupling constant lowered to 20 %. Calculate $\sigma_{20} \times Br \times A$ for those events, where σ_{20} is the cross-section for the Z′ with 20 % coupling strength.

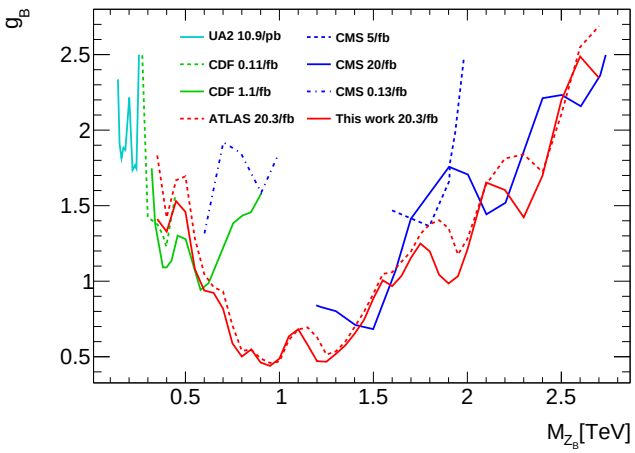

Figure 5.42: 95 % CL upper limits on coupling g_B. Results from UA2 are recorded in $p\bar{p}$ at $\sqrt{s} = 0.63\,\text{TeV}$, CDF uses also $p\bar{p}$ at $\sqrt{s} = 1.8\,\text{TeV}$ ($0.11\,\text{fb}^{-1}$) and $\sqrt{s} = 1.96\,\text{TeV}$. The results from ATLAS and CMS are obtained from pp collisions at $\sqrt{s} = 7\,\text{TeV}$ for CMS ($0.13\,\text{fb}^{-1}$, $5\,\text{fb}^{-1}$) and $\sqrt{s} = 8\,\text{TeV}$ for CMS ($20\,\text{fb}^{-1}$), ATLAS ($20.3\,\text{fb}^{-1}$) and this work.

2. Use limits for Gaussian type signals to extract a limit for Z′ according to mass and width.

3. Calculate limit on the coupling constant according to:

$$g_{\text{max}} = 0.2\sqrt{\frac{(\sigma \cdot \text{Br} \cdot A)_{\text{limit}}}{\sigma_{20} \cdot \text{Br} \cdot A}} \tag{5.20}$$

The result of this is shown in Fig. 5.42, compared to dijet resonance searches from several other experiments. The analysis in this work is able to set a limit on the coupling strength over a large range of masses. For most parts of this range the limit is the most stringent one observed so far. An important gap below 1 TeV could be closed, where a coupling strength of the order of one was still not excluded. This region was usually omitted, as the spectrum recorded by unprescaled triggers usually started around 1 TeV in LHC searches.

In the low mass region the limits are dominated by $p\bar{p}$ results from UA2 [130], the first run of CDF [131] and parts of the second run of CDF [132]. The limit from UA2 is the only limit that covers a range below 300 GeV and is thus dominating in this region. Between 300 GeV and 500 GeV the limit from CDFs first are exclusive, while between 500 GeV and 600 GeV the limits from CDFs second run dominate over this works result.

In the intermediate region limits are set by two $\sqrt{s} = 7\,\text{TeV}$ analysis by CMS [133], one with a novel technique for low mass searches with $\mathcal{L} = 0.13\,\text{fb}^{-1}$, circumventing prescale effects and a regular analysis with $\mathcal{L} = 5.0\,\text{fb}^{-1}$. The corresponding result from ATLAS [134] gives a similar limit and is thus omitted for simplification of the plot. The special result from CMS used only a very small data set and is thus superseded by this works limit. The high mass result from CMS

used about one quarter of the luminosity used in this work, thus it also gives a less stringent limit.

In the high mass region the limits are dominated by the $\sqrt{s} = 8\,\text{TeV}$ results from CMS [135] and ATLAS [114]. Above 1500 GeV the results from ATLAS, CMS and this work give comparable limits with local differences due to statistical fluctuations. With only some small local exceptions this works limits are the most stringent ones over the mass range of 600 GeV to 2500 GeV.

Comparison of Limits with Previous Results

	q^*	BlackMax	S8	W^* ($\sin\theta = 1$)	W^* ($\sin\theta = 0$)	W'	QBH
CMS	3.5	-	2.5	-	-	1.9	5.8
ATLAS	4.09	5.75	2.72	1.75	1.66	2.45	5.82
This work	3.96	5.67	2.68	1.59	1.71	2.17	5.75

Table 5.9: Observed mass limits at 95 % CL in TeV. for CMS [119], ATLAS [114] and this work. The CMS exclusion for W′ can also exclude a region between 2.0 TeV and 2.2 TeV. The ATLAS exclusion of W^* ($\sin\theta = 0$) can also exclude a region between 1.86 TeV and 1.98 TeV.

In the past a large number of experiments performed searches for resonances decaying in two jets. Starting with the UA1 experiment at the Super Proton Synchrotron (SPS), which published their first dijet search in 1986 [136], up to the most recent results in 2012 by the CMS and ATLAS experiments at the LHC (see [119] and [114]) over 15 experimental publications have dealt with dijet resonances. These results have been obtained at SPS, Tevatron and LHC at different center of mass energies ranging from 546 GeV up to 8 TeV. Some of these results used data from proton-anti-proton collisions, while others used proton-proton data. Depending on center of mass energy and luminosity different ranges in dijet mass have been probed, and different mass scales for new phenomena have been excluded. For example a W′ with unity couplings has been excluded from 100 GeV up to 2.45 TeV. For variable couplings of a Z′ the results of this analysis and former ones, is discussed in Sec. 5.5.5. In the plane of coupling vs. mass for almost all masses above 500 GeV the presented analysis supersedes all previous results.

A comparison of observed 95 % CL upper limits on the mass scale for different models is shown in Tab. 5.9 for the most recent results from ATLAS, CMS and the analysis presented in this thesis. The same comparison for the expected mass limits, which is a proxy for the performance of a detector and the understanding of the systematic uncertainties is shown in Tab. 5.10. The results show comparable numbers for the different models. The differences between the ATLAS publication and this analysis is mainly a different JES systematics. In this analysis an uncertainty was used, that is significantly lower than the one used in the ATLAS publication. This leads to weaker limits, as only smaller amounts of signal events can be added to the spectrum, within the systematic uncertainties.

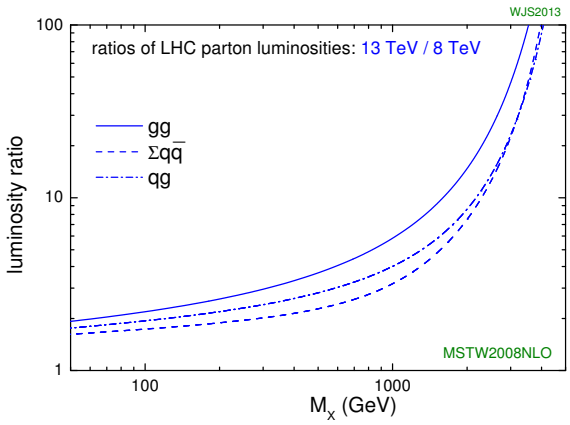

Figure 5.43: Ratio of parton luminosities between $\sqrt{s} = 13\,\text{TeV}$ and $8\,\text{TeV}$ for different parton flavors [137].

In comparison to the CMS result, for almost all quoted models, a stronger limit was calculated. For the excited quark model an observed limit of $3.96\,\text{TeV}$ was found in this thesis, while the CMS result gives a lower limit of $3.5\,\text{TeV}$.

Apart from these small differences in the final limit all dijet analysis performed so far did not find a persistent hint to resonances from New Physics phenomena.

	q^*	BlackMax	S8	W^* ($\sin\theta = 1$)	W^* ($\sin\theta = 0$)	W'	QBH
CMS	3.7	-	2.5	-	-	2.2	-
ATLAS	3.98	5.62	2.80	1.66	1.95	2.51	5.66
This work	3.90	5.67	2.74	1.66	1.98	2.37	5.75

Table 5.10: Expected mass limits at 95 % CL in TeV for CMS [119], ATLAS [114] and this work.

Outlook on Future Results

From early 2015 on the LHC started its second run with an increased center of mass energy of $\sqrt{s} = 13\,\text{TeV}$, which is close to the design value of $14\,\text{TeV}$ and a shorter distance between bunches of $25\,\text{ns}$, which is the ultimate value obtainable within the LHC. The increased center of mass energy changes the production cross-section of the QCD background and the signal differently, depending on the parton flavors. The ratio of the effective luminosities for these productions is shown in Fig. 5.43. For a resonance at $2\,\text{TeV}$ produced from quark and gluon the increase in center of mass energy leads to an increased production cross-section of a factor of approximately 10.

The models that can surpass the limits found in this work first, are those that are not affected by PDF suppression, as the Quantum Black Hole models. Other models will need a larger amount of luminosity to supersede these limits.

The first results from 2015 data have been published for a luminosity of $\mathcal{L} = 40\,\mathrm{pb}^{-1}$ by CMS [138] and $\mathcal{L} = 80\,\mathrm{pb}^{-1}$ by ATLAS [139]. The analysis from CMS sets a 95% C.L. expected (observed) upper limit on the mass of an Excited Quark at 2.9 TeV (2.7 TeV), which is still one TeV less than presented in this work. The ATLAS result sets observed limits for the mass of Quantum Black Holes produced with the QBH generator at 6.8 TeV and BlackMax at 6.5 TeV, with similar expected limits. These limits are already exceeding the limits from this work by more than one TeV.

6 CONCLUSIONS AND OUTLOOK

The Standard Model (SM) of particle physics has served as a predictive fundamental theory for almost 40 years until the last undiscovered particle, the Higgs boson, has been observed in 2012. The theory is extremely successful in describing nature. Until now there is no experimental evidence for a failure of the SM. Nevertheless phenomena like gravity cannot be described within the SM. Apart from this, several open questions are remaining which can be answered by new theories. These theories contain the SM as a low energy approximation of a more fundamental theory. By expanding the SM new particles might appear. A search for these particles can narrow down the available phase space for these theories.

In 2012 the Large Hadron Collider (LHC) at the European Organization for Nuclear Research (CERN) close to Geneva collided protons at another all-time record center of mass energy of $\sqrt{s} = 8\,\text{TeV}$. Due to the enormous number of proton-proton interactions and the fast repetition rate the recorded luminosity also reached a new maximum. This extends the range of observable resonance masses up to several TeV.

In this thesis the search for New Physics in the invariant dijet mass has been presented. The data used contained an integrated luminosity of $\mathcal{L} = 20.3\,\text{fb}^{-1}$ recorded with the ATLAS detector at $\sqrt{s} = 8\,\text{TeV}$. To probe a large range in dijet mass, the spectrum was combined from events recorded by 12 different jet triggers. This extended the spectrum to span an invariant dijet mass from 253 TeV up to 4.1 TeV. The combination of events has been compared to a leading order Monte Carlo prediction. Within 40 % accuracy the simulation is able to describe the features of the kinematical distributions from data. As this level of agreement is not accurate enough for a search for resonances in the spectrum, a different approach to estimate the background was followed. By fitting a functional form to the invariant mass spectrum from data, an estimation of the background contribution was found. This fit would have excluded regions for which the discrepancy between data and fit were to large. In the data examined here such an exclusion was not necessary, as a reasonable agreement between functional form and data was found. The final procedure to find resonance-like structures in data used the BumpHunter algorithm to compare the data with the background estimation, while taking the look-elsewhere effect into account. The algorithm did not find any significant discrepancies. Thus a Bayesian limit setting approach was performed.

For seven different models of New Physics 95 % C.L. limits have been set on cross-section times acceptance and by comparing to theoretical cross-sections also on the mass of these particles. Observed (expected) lower limits on the mass of an excited quark model could be set to 3.96 TeV

(3.90 TeV). For a scalar octet particle the observed (expected) lower limits are found to be 2.68 TeV (2.74 TeV). The observed (expected) lower limits for a heavy partner of the W boson have been set to 1.71 TeV (1.98 TeV). Two Monte Carlo generators have been examined which generate signals of Quantum Black Holes. The observed (expected) lower limits for black holes produced by the QBH generator have been computed to be 5.75 TeV (5.75 TeV). For the BlackMax generator observed and expected limits are at 5.67 TeV. For the model of the chiral W^* two values of the angle θ have been compared. For $\sin\theta = 1$ the observed (expected) lower limits are 1.59 TeV (1.66 TeV), while for $\sin\theta = 0$ limits of 1.71 TeV (1.98 TeV) were found. These limits are improving the knowledge from previous results, by extending the excluded masses by up to 1 TeV.

In addition to calculating limits on the mass of a specific model, a more model-independent limit was computed. By setting limits on a signal shape that follows a Gaussian distribution, limits could be provided that are usable by theorists to find a limit for their favorite model which predicts a resonance-like feature in the dijet spectrum. Limits on the cross-section times acceptance for Gaussian signals with a relative width of 7 %, 10 % and 15 % are provided, in addition to a minimal relative width that is expected for a narrow resonance smeared by the detector resolution. A second type of model independent limits is calculated by generating a signal shape according to a Breit-Wigner distribution which is modified by effects of parton densities, parton showering and detector resolution. This type of limit gives the possibility to extract a cross-section times acceptance limit for a model, by only knowing the final state partons and the intrinsic width or lifetime of the resonance.

To compare the performance of past and future colliders a last category of limits was also examined. By calculating the limit for a hypothetical Z′ boson with a lowered coupling, a 95 % C.L. lower limit on the coupling of a Z′ to quarks can be calculated. This limit can now be compared to results from other colliders, where also other types of particles are collided. This technique made it possible to find phase space regions which have not been excluded so far. One of these regions could then be excluded by this work, by exploiting the combination of triggers. Furthermore it was possible to improve almost all former coupling limits starting from 500 GeV.

In 2015 the LHC started a second run at $\sqrt{s} = 13$ TeV. As this new record energy needs further optimizations and understanding of the accelerator and detector hardware, a slowly increasing instantaneous luminosity of proton-proton collisions was used. Thus the total integrated luminosity was about a factor of 5 smaller than the one used in this thesis. The increased center of mass energy extends the range of resonance masses that can be examined with this smaller amount of luminosity to approximately 7 TeV. At the time of writing the first results from the ATLAS and CMS collaborations were published, which surpassed the range of high mass resonances examined in this paper. Both collaborations did not analyze the spectrum at low masses, thus the result in this work is still the most stringent limit in the region between 500 GeV and 1.2 TeV. For the future different techniques can be used to exploit the low mass region with high luminosity, by exploiting pair-production of resonances, associated production with an initial state radiation or more sophisticated techniques exploiting the trigger hardware.

A SELECTION CRITERIA FOR JET CLEANING

	Looser	*Loose*
1	($f_{HEC} > 0.5$ and $\lvert f_Q^{HEC}\rvert > 0.5$ and $\langle Q\rangle > 0.8$) or $\lvert E_{neg}\rvert > 60\,\text{GeV}$	*Looser* or ($f_{HEC} > 0.5$ and $\lvert f_Q^{HEC}\rvert > 0.5$)
2	($f_{EM} > 0.95$ and $f_Q^{LAr} > 0.8$ and $\langle Q\rangle > 0.8$ and $\lvert\eta\rvert < 2.8$)	*Looser* or ($f_{EM} > 0.95$ and $f_Q^{LAr} > 0.8$ and $\lvert\eta\rvert < 2.8$)
3	($f_{max} > 0.99$ and $\lvert\eta\rvert < 2$) or ($f_{EM} < 0.05$ and $f_{ch} < 0.05$ and $\lvert\eta\rvert < 2$) or ($f_{EM} < 0.05$ and $\lvert\eta\rvert \geqslant 2$)	*Looser* or $\lvert t_{jet}\rvert > 25\,\text{ns}$

Table A.1: Selection criteria for *Looser* and *Loose* cleaning in categories HEC spikes (1), Coherent EM noise (2) and non-collision background (3) from [105].

	Medium	*Tight*
1	*Loose* or $f_{HEC} > 1 - \lvert f_Q^{HEC}\rvert$	*Medium*
2	*Loose* or ($f_{EM} > 0.9$ and $f_Q^{LAr} > 0.8$ and $\lvert\eta\rvert < 2.8$)	*Medium* or $f_Q^{LAr} > 0.95$ or ($f_{EM} > 0.98$ and $f_Q^{LAr} > 0.05$)
3	($f_{max} > 0.99$ and $\lvert\eta\rvert < 2$) *Loose* or $\lvert t_{jet}\rvert > 10\,\text{ns}$ ($f_{EM} < 0.05$ and $f_{ch} < 0.1$ and $\lvert\eta\rvert < 2$) ($f_{EM} > 0.95$ and $f_{ch} < 0.05$ and $\lvert\eta\rvert < 2$)	*Looser* or *Medium* or ($f_{EM} < 0.1$ and $f_{ch} < 0.2$ and $\lvert\eta\rvert < 2.5$) or ($f_{EM} > 0.9$ and $f_{ch} < 0.1$ and $\lvert\eta\rvert < 2.5$) or ($f_{ch} < 0.01$ and $\lvert\eta\rvert < 2.5$) or ($f_{EM} < 0.1$ and $\lvert\eta\rvert \geqslant 2.5$)

Table A.2: Selection criteria for *medium* and *tight* cleaning in categories HEC spikes (1), Coherent EM noise (2) and non-collision background (3) from [105].

B SINGLE JET TRIGGER EFFICIENCIES

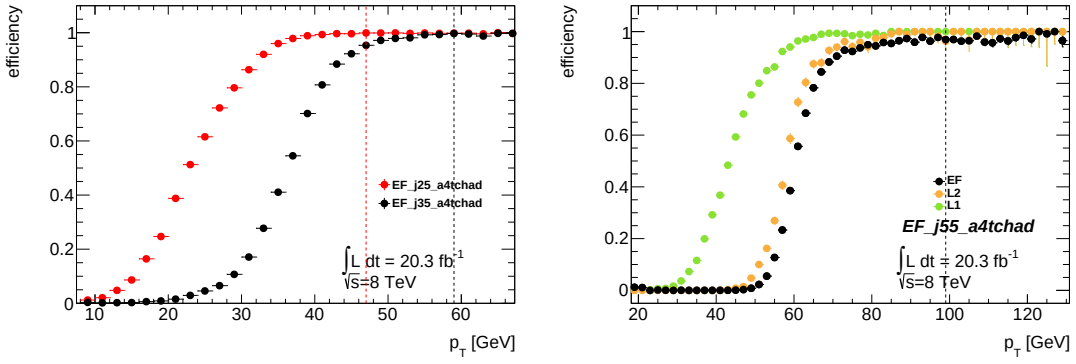

(a) Efficiency for j25 and j35

(b) Efficiency for j55

Figure B.1: Single jet trigger efficiencies for j25, j35 and j55.

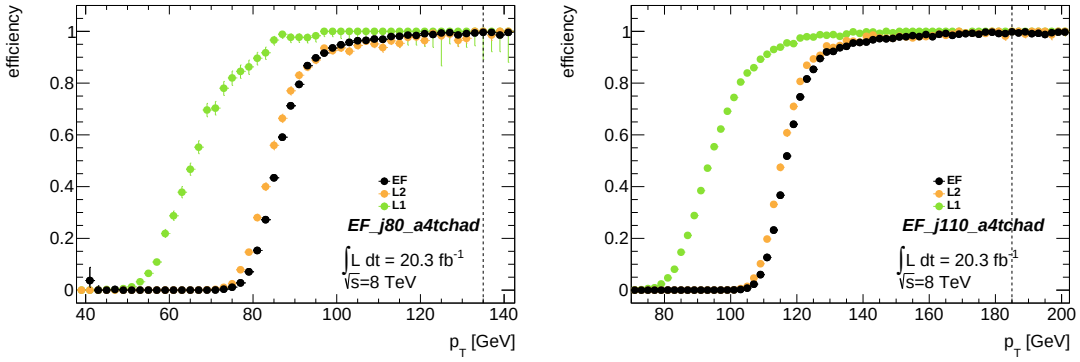

(a) Efficiency for j80

(b) Efficiency for j110

Figure B.2: Single jet trigger efficiencies for j80 and j110.

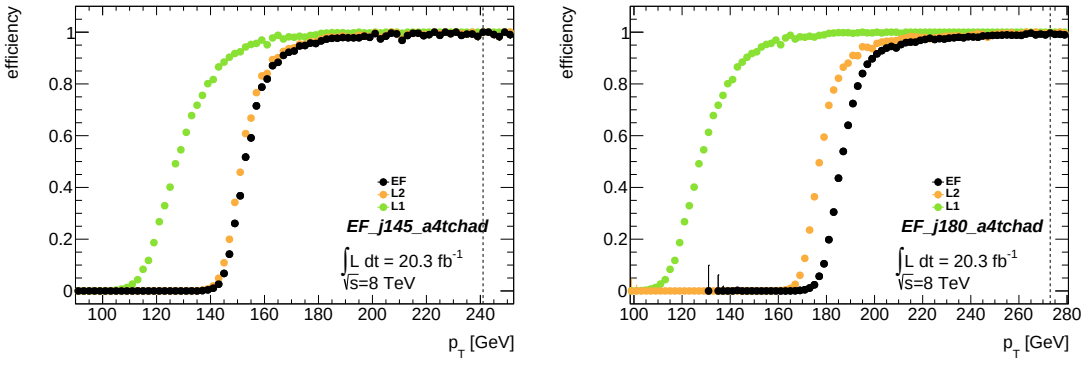

(a) Efficiency for j145 **(b)** Efficiency for j180

Figure B.3: Single jet trigger efficiencies for j145 and j180.

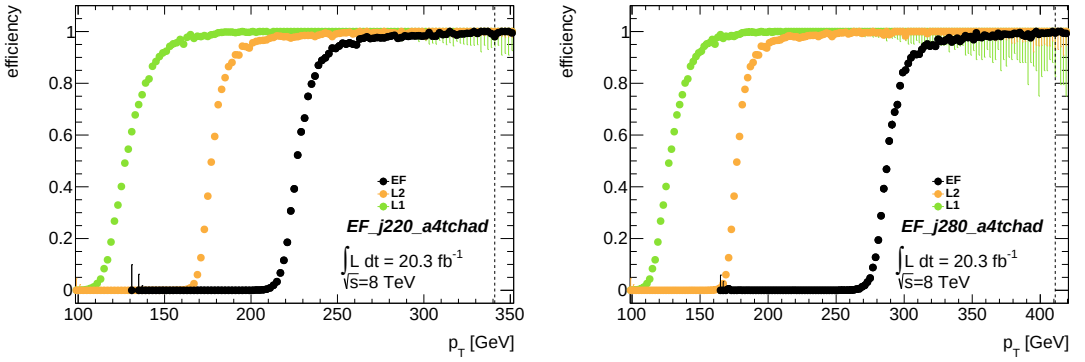

(a) Efficiency for j220 **(b)** Efficiency for j280

Figure B.4: Single jet trigger efficiencies for j220 and j280.

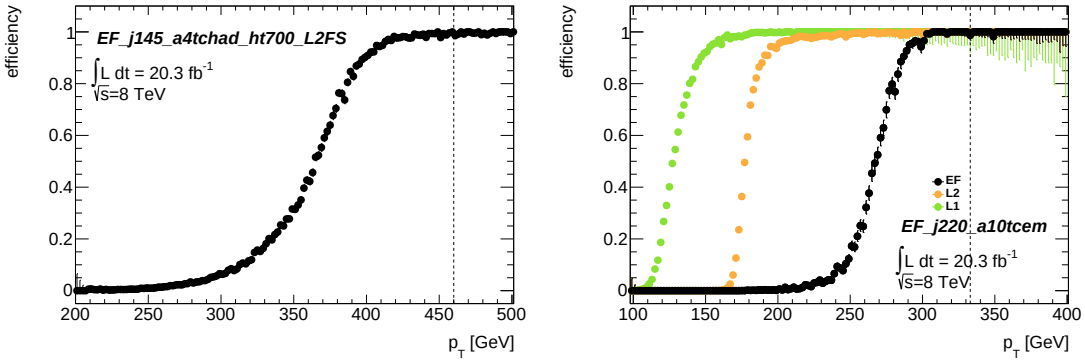

(a) Efficiency for j145_ht700 **(b)** Efficiency for delayed stream j220_a10tcem

Figure B.5: Jet trigger efficiencies for j145_ht700 and j220_a10tcem.

C | NEW PHYSICS SIGNALS

SIGNAL SHAPES

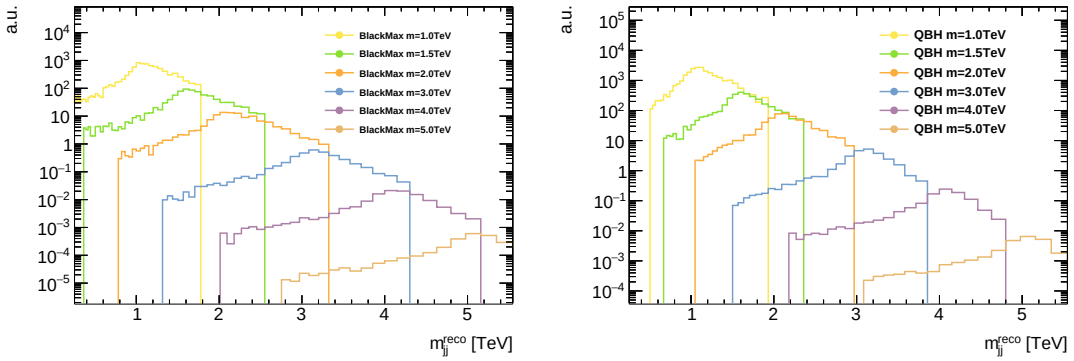

(a) Quantum Black Holes BlackMax **(b)** Quantum Black Holes QBH

Figure C.1: Signal templates for Quantum Black Holes for all masses used.

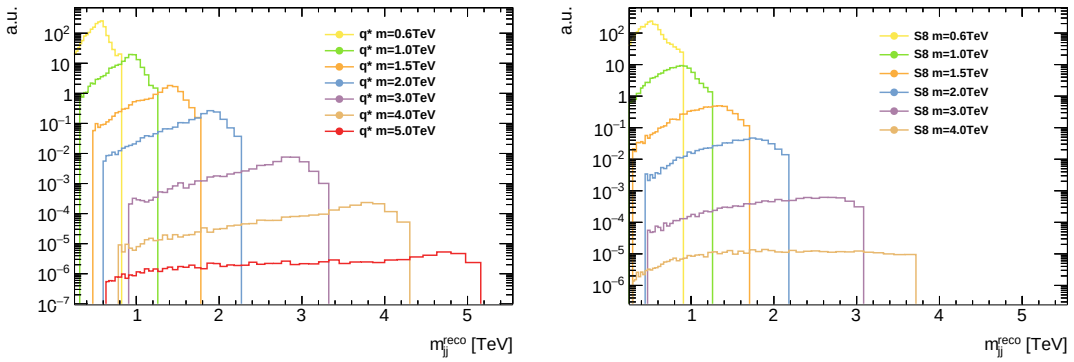

(a) Excited quarks **(b)** Color Scalar Octet

Figure C.2: Signal templates for Excited Quark and Color Scalar Octet for all masses used.

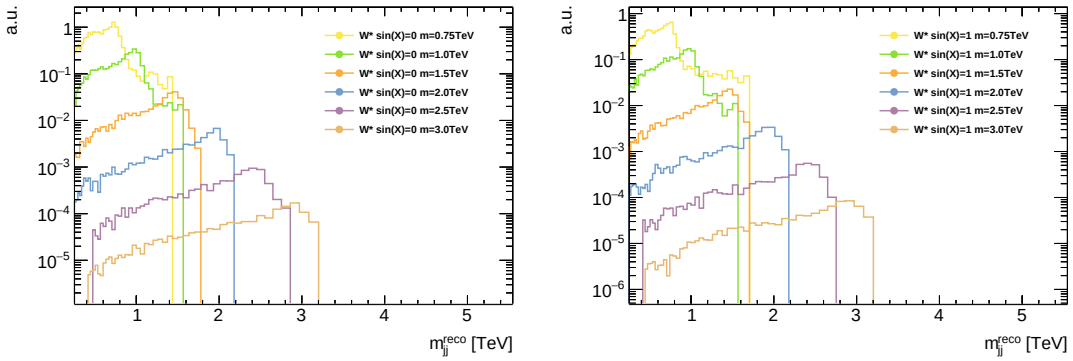

(a) W^* ($\sin\theta = 0$) **(b)** W^* ($\sin\theta = 1$)

Figure C.3: Signal templates for W^* for all masses used.

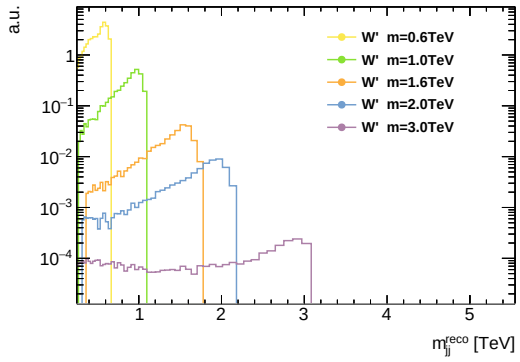

Figure C.4: W' signal templates for all masses used.

ACCEPTANCES AND EFFICIENCIES

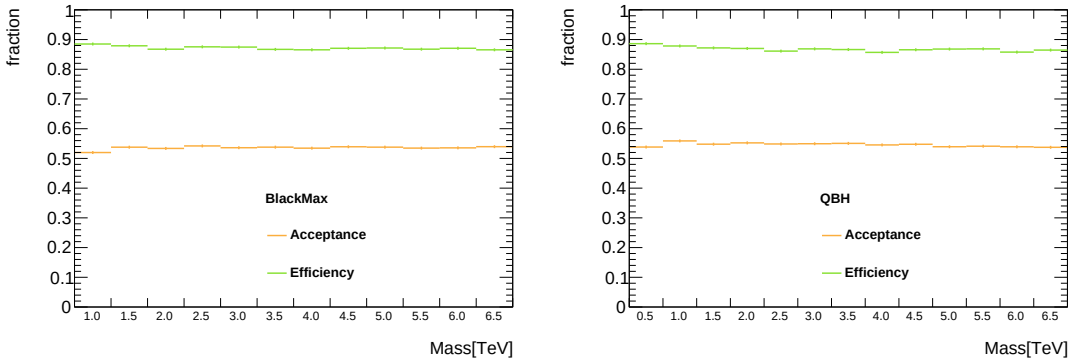

(a) Quantum Black Holes BlackMax **(b)** Quantum Black Holes QBH

Figure C.5: Acceptance and efficiency for Quantum Black Holes for different pole masses. Statistical uncertainties are shown.

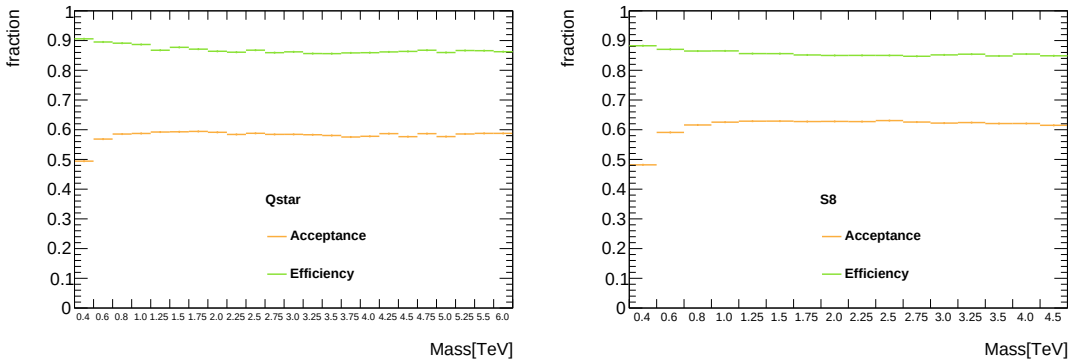

(a) Excited quarks **(b)** Color Scalar Octet

Figure C.6: Acceptance and efficiency for Excited Quark and Color Scalar Octet for different pole masses. Statistical uncertainties are shown.

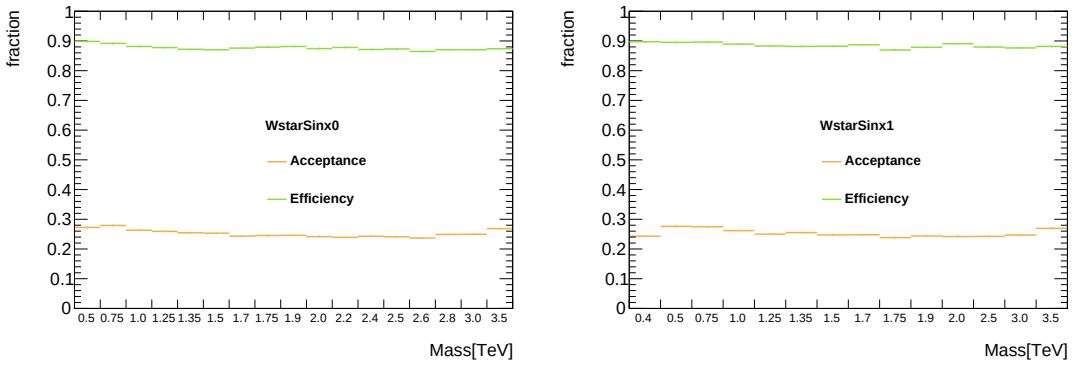

(a) W^* $(\sin\theta = 0)$ **(b)** W^* $(\sin\theta = 1)$

Figure C.7: Acceptance and efficiency for W^* for different pole masses. Statistical uncertainties are shown.

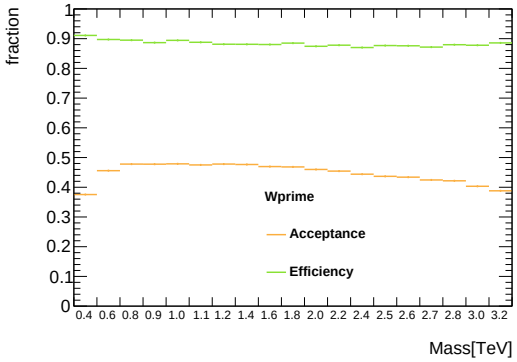

Figure C.8: Acceptance and efficiency for W' for different pole masses. Statistical uncertainties are shown.

OPTIMAL RAPIDITY DIFFERENCE CUT

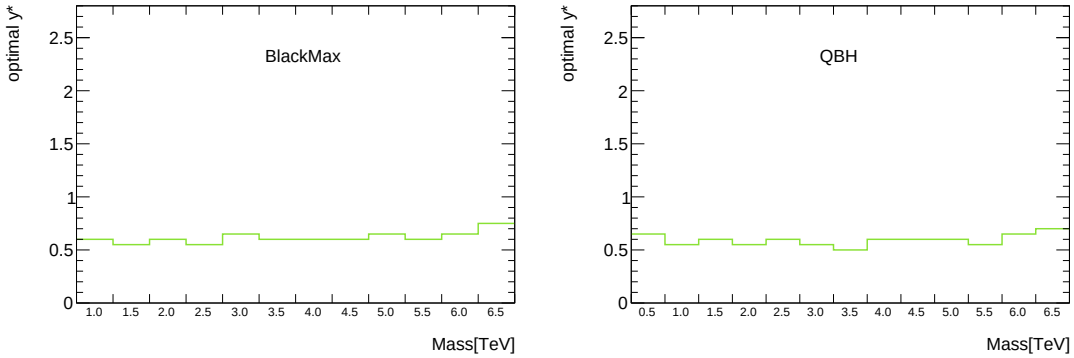

(a) Quantum Black Holes BlackMax **(b)** Quantum Black Holes QBH

Figure C.9: Optimal $|y^*|$ cut for Quantum Black Holes for different pole masses.

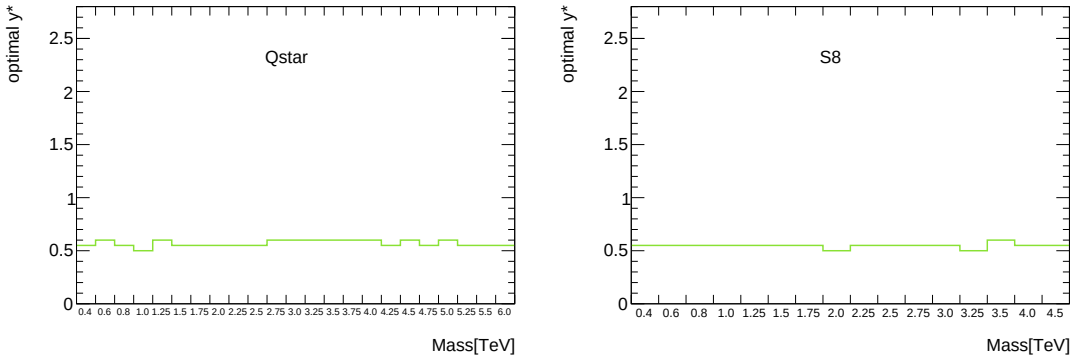

(a) Excited quarks **(b)** Color Scalar Octet

Figure C.10: Optimal $|y^*|$ cut for Excited Quark and Color Scalar Octet for different pole masses.

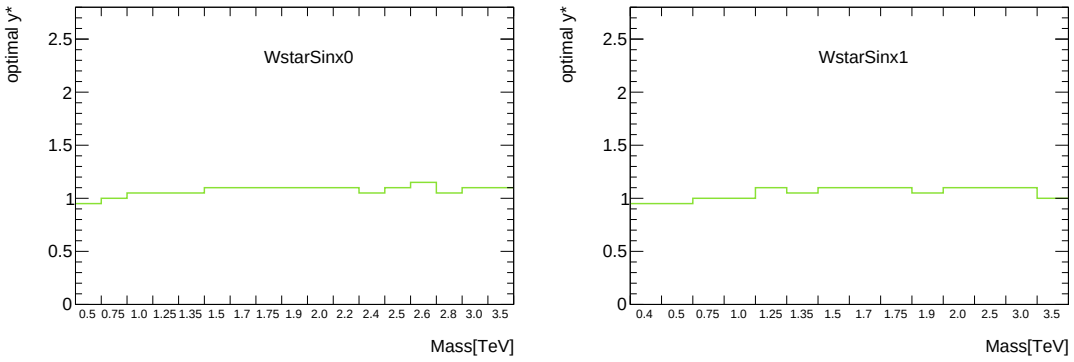

(a) W^* ($\sin\theta = 0$) **(b)** W^* ($\sin\theta = 1$)

Figure C.11: Optimal $|y^*|$ cut for W^* for different pole masses.

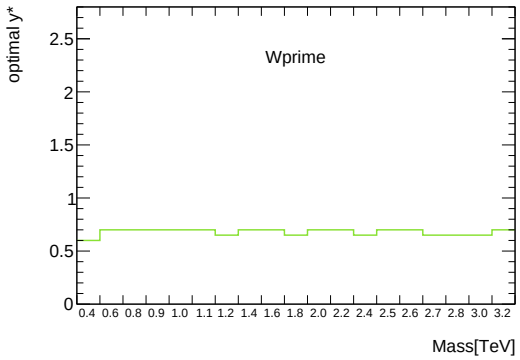

Figure C.12: Optimal $|y^*|$ cut for W' for different pole masses.

BIBLIOGRAPHY

[1] Isaac Newton. *Opticks: or, a treatise of the reflexions, refractions, inflexions and colours of light. Also two treatises of the species and magnitude of curvilinear figures.* 1704.

[2] Christiaan Huygens. *Traité de la lumiere : ou sont expliquee les causes de ce qui luy arrive dans la reflexion, and dans la refraction, et particulierement dans l'entrange refraction du cristal d'Islande ; avec un discours de la cause de la pesanteu, par. C.H.D.Z.* 1690.

[3] Henri Becquerel. "Sur les radiations émises par phosphorescence." In: *Comptes Rendus* 122 (1896), pp. 420–421.

[4] A. Einstein. "Über einen die Erzeugung und Verwandlung des Lichtes betreffenden heuristischen Gesichtspunkt." In: *Annalen der Physik* 322.6 (1905), pp. 132–148. ISSN: 1521-3889. DOI: 10.1002/andp.19053220607.

[5] D. Mendelejeff. "On the Relationship of Properties of the Elements to their Atomic Weights." In: *Zeitschrift für Chemie* 12 (1869), pp. 405–406.

[6] J.J. Thomson. "Cathode rays." In: *Philosophical Magazine* 44 (1897), p. 293.

[7] H. Geiger and E. Marsden. "On a Diffuse Reflection of the Formula-Particles." In: *Proceedings of the Royal Society A: Mathematical, Physical and Engineering Sciences* 82.557 (July 1909), 495–500. ISSN: 1471-2946. DOI: 10.1098/rspa.1909.0054.

[8] E Rutherford. "The Scattering of α and β Particles by Matter and the Structure of the Atom." In: *Philosophical Magazine. Series* 6.21 (1911).

[9] N. Bohr. "I. On the constitution of atoms and molecules." In: *Philosophical Magazine Series 6* 26.151 (July 1913), 1–25. ISSN: 1941-5990. DOI: 10.1080/14786441308634955.

[10] N. Bohr. "LXXIII. On the constitution of atoms and molecules." In: *Philosophical Magazine Series 6* 26.155 (Nov. 1913), 857–875. ISSN: 1941-5990. DOI: 10.1080/14786441308635031.

[11] N. Bohr. "XXXVII. On the constitution of atoms and molecules." In: *Philosophical Magazine Series 6* 26.153 (Sept. 1913), 476–502. ISSN: 1941-5990. DOI: 10.1080/14786441308634993.

[12] J. Chadwick. "Possible Existence of a Neutron." In: *Nature* 129.3252 (Feb. 1932), 312–312. ISSN: 0028-0836. DOI: 10.1038/129312a0.

[13] Carl D. Anderson. "The Positive Electron." In: *Physical Review* 43.6 (Mar. 1933), 491–494. ISSN: 0031-899X. DOI: 10.1103/physrev.43.491.

[14] C. M. G. Lattes et al. "Processes Involving Charged Mesons." In: *Nature* 159 (May 1947), pp. 694–697. DOI: 10.1038/159694a0.

[15] Eugene Gardner and C. M. G. Lattes. "Production of Mesons by the 184-Inch Berkeley Cyclotron." In: *Science* 107.2776 (1948), pp. 270–271. DOI: 10.1126/science.107.2776.270.

[16] J. Iliopoulos. "Progress in Gauge Theories." In: *High energy physics. Proceedings, 17th International Conference, ICHEP 1974, London, England, July 01-July 10, 1974*. 1974, pp. III.89–116. URL: http://inspirehep.net/record/3000/files/c74-07-01-p089.pdf.

[17] M. Gell-Mann. "A schematic model of baryons and mesons." In: *Physics Letters* 8.3 (Feb. 1964), 214–215. ISSN: 0031-9163. DOI: 10.1016/s0031-9163(64)92001-3.

[18] G Zweig. "An SU_3 model for strong interaction symmetry and its breaking; Version 2." In: CERN-TH-412 (Feb. 1964). Version 1 is CERN preprint 8182/TH.401, Jan. 17, 1964, 80 p. URL: https://cds.cern.ch/record/570209.

[19] O. W. Greenberg. "Spin and Unitary-Spin Independence in a Paraquark Model of Baryons and Mesons." In: *Phys. Rev. Lett.* 13 (20 Nov. 1964), pp. 598–602. DOI: 10.1103/PhysRevLett.13.598.

[20] M. Y. Han and Y. Nambu. "Three-Triplet Model with Double SU(3) Symmetry." In: *Physical Review* 139.4B (Aug. 1965), B1006–B1010. ISSN: 0031-899X. DOI: 10.1103/physrev.139.b1006.

[21] Steven Weinberg. "A Model of Leptons." In: *Physical Review Letters* 19.21 (Nov. 1967), 1264–1266. ISSN: 0031-9007. DOI: 10.1103/physrevlett.19.1264.

[22] H. Fritzsch, Murray Gell-Mann, and H. Leutwyler. "Advantages of the Color Octet Gluon Picture." In: *Phys. Lett.* B47 (1973), pp. 365–368. DOI: 10.1016/0370-2693(73)90625-4.

[23] Georges Aad et al. "Observation of a new particle in the search for the Standard Model Higgs boson with the ATLAS detector at the LHC." In: *Phys. Lett.* B716 (2013), pp. 1–29. DOI: 10.1016/j.physletb.2012.08.020. arXiv: 1207.7214 [hep-ex].

[24] Serguei Chatrchyan et al. "Observation of a new boson at a mass of 125 GeV with the CMS experiment at the LHC." In: *Phys. Lett.* B716 (2013), pp. 30–61. DOI: 10.1016/j.physletb.2012.08.021. arXiv: 1207.7235 [hep-ex].

[25] Wikimedia Commons. *Standard Model of Elementary Particles modified version*. File:Standard Model of Elementary Particles modified version.svg. 2015. URL: https://commons.wikimedia.org/wiki/File:Standard_Model_of_Elementary_Particles_modified_version.svg (visited on 11.09.2015).

[26] Ch. Kraus et al. "Final results from phase II of the Mainz neutrino mass search in tritium beta decay." In: *Eur. Phys. J.* C40 (2005), pp. 447–468. DOI: 10.1140/epjc/s2005-02139-7. arXiv: hep-ex/0412056 [hep-ex].

[27] Steven Weinberg. *The Quantum theory of fields. Vol. 1: Foundations*. Cambridge University Press, 2005. ISBN: 9780521670531, 9780511252044.

[28] Vladimir A. Miransky. "Dynamical symmetry breaking and tight bound states in quantum field theory." In: *Phys. Lett.* B248 (1990), pp. 151–155. DOI: 10.1016/0370-2693(90)90030-A.

[29] M. Markevitch et al. "Direct Constraints on the Dark Matter Self-Interaction Cross Section from the Merging Galaxy Cluster 1E 0657–56." In: *The Astrophysical Journal* 606.2 (May 2004), pp. 819–824. ISSN: 1538-4357. DOI: 10.1086/383178.

[30] Douglas Clowe, Anthony Gonzalez, and Maxim Markevitch. "Weak-Lensing Mass Reconstruction of the Interacting Cluster 1E 0657–558: Direct Evidence for the Existence of Dark Matter." In: *The Astrophysical Journal* 604.2 (Apr. 2004), pp. 596–603. ISSN: 1538-4357. DOI: 10.1086/381970.

[31] P. A. R. Ade et al. "Planck 2013 results. XVI. Cosmological parameters." In: *Astron. Astrophys.* 571 (2014), A16. DOI: 10.1051/0004-6361/201321591. arXiv: 1303.5076 [astro-ph.CO].

[32] P. A. R. Ade et al. "Planck 2015 results. XIII. Cosmological parameters." In: (2015). arXiv: 1502.01589 [astro-ph.CO].

[33] U. Baur, I. Hinchliffe, and D. Zeppenfeld. "Excited Quark Production at Hadron Colliders." In: *Int. J. Mod. Phys. A* 2 (1987), p. 1285. DOI: 10.1142/S0217751X87000661.

[34] U. Baur, M. Spira, and P. M. Zerwas. "Excited-Quark and -Lepton Production at Hadron Colliders." In: *Phys. Rev. D* 42 (1990), p. 815. DOI: 10.1103/PhysRevD.42.815.

[35] Paul H. Frampton and Sheldon L. Glashow. "Chiral Color: An alternative to the standard model." In: *Phys. Lett. B* (1987), p. 157. DOI: 10.1016/0370-2693(87)90859-8.

[36] Paul H. Frampton and Sheldon L. Glashow. "Unifiable Chiral Color with Natural GIM Mechanism." In: *Phys. Rev. Lett.* 58 (1987), p. 2168. DOI: 10.1103/PhysRevLett.58.2168.

[37] Jonathan Bagger, Carl Schmidt, and Stephen King. "Axigluon Production in Hadronic Collisions." In: *Phys. Rev. D* 37 (1988), p. 1188. DOI: 10.1103/PhysRevD.37.1188.

[38] Tao Han, Ian Lewis, and Zhen Liu. "Colored Resonant Signals at the LHC: Largest Rate and Simplest Topology." In: *J. High Energy Phys.* 12 (2010), p. 085. DOI: 10.1007/JHEP12(2010)085. arXiv: 1010.4309 [hep-ph].

[39] Howard Georgi, Elizabeth E. Jenkins, and Elizabeth H. Simmons. "The un-unified standard model." In: *Nucl. Phys. B* 331 (1990), pp. 541–555. DOI: 10.1016/0550-3213(90)90083-P.

[40] Christophe Grojean, Ennio Salvioni, and Riccardo Torre. "A weakly constrained W' at the early LHC." In: *J. High Energy Phys.* 1107 (2011), p. 002. DOI: 10.1007/JHEP07(2011)002. arXiv: 1103.2761 [hep-ph].

[41] Mirjam Cvetic and Jogesh C. Pati. "N = 1 supergravity within the minimal left-right symmetric model." In: *Phys. Lett. B* 135 (1984), pp. 57–62. DOI: 10.1016/0370-2693(84)90453-2.

[42] Yukihiro Mimura and S. Nandi. "Orbifold breaking of left-right gauge symmetry." In: *Phys. Lett. B* 538 (2002), pp. 406–414. DOI: 10.1016/S0370-2693(02)02000-2. arXiv: hep-ph/0203126 [hep-ph].

[43] G. Altarelli, B. Mele, and M. Ruiz-Altaba. "Searching for new heavy vector bosons in $p\bar{p}$ colliders." In: *Z. Phys. C* 45 (1989), pp. 109–121. DOI: 10.1007/BF01556677.

[44] G. Altarelli, B. Mele, and M. Ruiz-Altaba. "Erratum: Searching for new heavy vector bosons in $p\bar{p}$ colliders." In: *Z. Phys. C* 47 (1990), p. 676. DOI: 10.1007/BF01552335.

[45] Serguei Chatrchyan et al. "Search for a W' boson decaying to a muon and a neutrino in pp collisions at $\sqrt{s} = 7$ TeV." In: *Phys. Lett.* B701 (2011), pp. 160–179. DOI: 10.1016/j.physletb.2011.05.048. arXiv: 1103.0030 [hep-ex].

[46] ATLAS Collaboration. "Search for a heavy gauge boson decaying to a charged lepton and a neutrino in 1 fb^{-1} of pp collisions at $\sqrt{s} = 7$ TeV using the ATLAS detector." In: *Phys. Lett. B* 705 (2011), pp. 28–46. DOI: 10.1016/j.physletb.2011.09.093. arXiv: 1108.1316 [hep-ex].

[47] M.V. Chizhov, V.A. Bednyakov, and J.A. Budagov. "A Unique Signal of Excited Bosons in Dijet Data from pp Collisions." In: *Phys. Atom. Nucl.* 75 (1 2012), p. 90. DOI: 10.1134/s1063778812010061.

[48] M.V. Chizhov and G. Dvali. "Origin and phenomenology of weak-doublet spin-1 bosons." In: *Phys. Lett. B* 703 (2011), p. 593. DOI: 10.1016/j.physletb.2011.08.056.

[49] M.V. Chizhov. "A Reference Model for Anomolously Interacting Bosons." In: *Phys. Part. Nucl. Lett.* 8 (2011), pp. 512–516. DOI: 10.1134/S1547477111060045. arXiv: 1005.4287 [hep-ph].

[50] M.V. Chizhov, V.A. Bednyakov, and J.A. Budagov. "On resonance search in dijet events at the LHC." In: (2011). arXiv: 1106.4161 [hep-ph].

[51] Luis A. Anchordoqui et al. "Inelastic black hole production and large extra dimensions." In: *Phys. Lett. B* 594 (2004), p. 363. DOI: 10.1016/j.physletb.2004.05.051. arXiv: hep-ph/0311365 [hep-ph].

[52] Patrick Meade and Lisa Randall. "Black Holes and Quantum Gravity at the LHC." In: *J. High Energy Phys.* 0805 (2008), p. 003. DOI: 10.1088/1126-6708/2008/05/003. arXiv: 0708.3017 [hep-ph].

[53] Xavier Calmet, Wei Gong, and Stephen D.H. Hsu. "Colorful quantum black holes at the LHC." In: *Phys. Lett. B* 668 (2008), pp. 20–23. DOI: 10.1016/j.physletb.2008.08.011. arXiv: 0806.4605 [hep-ph].

[54] Douglas M. Gingrich. "Quantum black holes with charge, colour, and spin at the LHC." In: *J. Phys. G* 37 (2010), p. 105008. DOI: 10.1088/0954-3899/37/10/105008. arXiv: 0912.0826 [hep-ph].

[55] Nima Arkani-Hamed, Savas Dimopoulos, and G.R. Dvali. "The Hierarchy problem and new dimensions at a millimeter." In: *Phys. Lett.* B429 (1998), pp. 263–272. DOI: 10.1016/S0370-2693(98)00466-3. arXiv: hep-ph/9803315 [hep-ph].

[56] Nima Arkani-Hamed, Savas Dimopoulos, and G.R. Dvali. "Phenomenology, astrophysics and cosmology of theories with submillimeter dimensions and TeV scale quantum gravity." In: *Phys. Rev. D* 59 (1999), p. 086004. DOI: 10.1103/PhysRevD.59.086004. arXiv: hep-ph/9807344 [hep-ph].

[57] John M. Campbell, J. W. Huston, and W. J. Stirling. "Hard Interactions of Quarks and Gluons: A Primer for LHC Physics." In: *Rept. Prog. Phys.* 70 (2007), p. 89. DOI: 10.1088/0034-4885/70/1/R02. arXiv: hep-ph/0611148 [hep-ph].

[58] John C. Collins, Davison E. Soper, and George F. Sterman. "Factorization for Short Distance Hadron - Hadron Scattering." In: *Nucl. Phys.* B261 (1985), p. 104. DOI: 10.1016/0550-3213(85)90565-6.

[59] Yuri L. Dokshitzer. "Calculation of the Structure Functions for Deep Inelastic Scattering and e+ e- Annihilation by Perturbation Theory in Quantum Chromodynamics." In: *Sov. Phys. JETP* 46 (1977). [Zh. Eksp. Teor. Fiz.73,1216(1977)], pp. 641–653.

[60] V. N. Gribov and L. N. Lipatov. "e+ e- pair annihilation and deep inelastic e p scattering in perturbation theory." In: *Sov. J. Nucl. Phys.* 15 (1972). [Yad. Fiz.15,1218(1972)], pp. 675–684.

[61] Guido Altarelli and G. Parisi. "Asymptotic Freedom in Parton Language." In: *Nucl. Phys.* B126 (1977), p. 298. DOI: 10.1016/0550-3213(77)90384-4.

[62] Pavel M. Nadolsky et al. "New parton distributions for collider physics." In: *Phys. Rev. D* 82 (2010), p. 074024. arXiv: 1007.2241 [hep-ph].

[63] A. D. Martin et al. "Parton distributions for the LHC." In: *Eur. Phys. J.* C63 (2009), pp. 189–285. DOI: 10.1140/epjc/s10052-009-1072-5. arXiv: 0901.0002 [hep-ph].

[64] Richard D. Ball et al. "Parton distributions with LHC data." In: *Nucl. Phys.* B867 (2013), pp. 244–289. DOI: 10.1016/j.nuclphysb.2012.10.003. arXiv: 1207.1303 [hep-ph].

[65] F. D. Aaron et al. "Combined measurement and QCD analysis of the inclusive e ± p scattering cross sections at HERA." In: *J. High Energ. Phys.* 2010.1 (Jan. 2010). ISSN: 1029-8479. DOI: 10.1007/jhep01(2010)109.

[66] Frank Siegert. "Monte-Carlo event generation for the LHC." PhD thesis. Durham U. URL: http://inspirehep.net/record/1296465/files/374132240_thesis.pdf.

[67] Andy Buckley et al. "General-purpose event generators for LHC physics." In: *Phys. Rept.* 504 (2011), pp. 145–233. DOI: 10.1016/j.physrep.2011.03.005. arXiv: 1101.2599 [hep-ph].

[68] Aude Gehrmann-De Ridder, Thomas Gehrmann, and E.W. Nigel Glover. "Antenna subtraction at NNLO." In: *J. High Energy Phys.* 2005.09 (Sept. 2005), 056–056. ISSN: 1029-8479. DOI: 10.1088/1126-6708/2005/09/056.

[69] Stefan Weinzierl. "Next-to-Next-to-Leading Order Corrections to Three-Jet Observables in Electron-Positron Annihilation." In: *Physical Review Letters* 101.16 (Oct. 2008). ISSN: 1079-7114. DOI: 10.1103/physrevlett.101.162001.

[70] Stefano Frixione and Massimiliano Grazzini. "Subtraction at NNLO." In: *J. High Energy Phys.* 2005.06 (June 2005), 010–010. ISSN: 1029-8479. DOI: 10.1088/1126-6708/2005/06/010.

[71] Torbjorn Sjostrand, Stephen Mrenna, and Peter Z. Skands. "PYTHIA 6.4 Physics and Manual." In: *J. High Energy Phys.* 05 (2006), p. 026. DOI: 10.1088/1126-6708/2006/05/026. arXiv: 0603.175 [hep-ph].

[72] G. Marchesini et al. "HERWIG: A Monte Carlo event generator for simulating hadron emission reactions with interfering gluons. Version 5.1 - April 1991." In: *Computer Physics Communications* 67 (1992), pp. 465–508. DOI: 10.1016/0010-4655(92)90055-4.

[73] Oliver Sim Brüning et al. *LHC Design Report*. Geneva: CERN, 2004. URL: https://cds.cern.ch/record/782076.

[74] *LEP design report*. Geneva: CERN, 1984. URL: https://cds.cern.ch/record/102083.

[75] S. Chatrchyan et al. "The CMS experiment at the CERN LHC." In: *JINST* 3 (2008), S08004. DOI: 10.1088/1748-0221/3/08/S08004.

[76] A. Augusto Alves Jr. et al. "The LHCb Detector at the LHC." In: *JINST* 3 (2008), S08005. DOI: 10.1088/1748-0221/3/08/S08005.

[77] K. Aamodt et al. "The ALICE experiment at the CERN LHC." In: *JINST* 3 (2008), S08002. DOI: 10.1088/1748-0221/3/08/S08002.

[78] O. Adriani et al. "The LHCf detector at the CERN Large Hadron Collider." In: *JINST* 3 (2008), S08006. DOI: 10.1088/1748-0221/3/08/S08006.

[79] G. Anelli et al. "The TOTEM experiment at the CERN Large Hadron Collider." In: *JINST* 3 (2008), S08007. DOI: 10.1088/1748-0221/3/08/S08007.

[80] James Pinfold et al. *Technical Design Report of the MoEDAL Experiment*. Tech. rep. CERN-LHCC-2009-006. MoEDAL-TDR-001. Geneva: CERN, June 2009. URL: https://cds.cern.ch/record/1181486.

[81] ATLAS Collaboration. "The ATLAS Experiment at the CERN Large Hadron Collider." In: *JINST* 3 (2008), S08003. DOI: 10.1088/1748-0221/3/08/S08003.

[82] Konrad Kleinknecht. *Detectors for particle radiation*. Cambridge University Press, 1998. ISBN: 9780521648547. DOI: 10.2277/0521648548.

[83] ATLAS Collaboration. *ATLAS calorimeter performance: Technical Design Report*. Technical Design Report ATLAS. Geneva: CERN, 1996. URL: https://cds.cern.ch/record/331059.

[84] K. A. Olive et al. "Review of Particle Physics." In: *Chin. Phys.* C38 (2014), p. 090001. DOI: 10.1088/1674-1137/38/9/090001.

[85] ATLAS Collaboration. *ATLAS inner detector: Technical Design Report, 1*. Technical Design Report ATLAS. Geneva: CERN, 1997. URL: https://cds.cern.ch/record/331063.

[86] S Haywood et al. *ATLAS inner detector: Technical Design Report, 2*. Technical Design Report ATLAS. Geneva: CERN, 1997. URL: https://cds.cern.ch/record/331064.

[87] ATLAS Collaboration. *ATLAS tile calorimeter: Technical Design Report*. Technical Design Report ATLAS. Geneva: CERN, 1996. URL: https://cds.cern.ch/record/331062.

[88] ATLAS Collaboration. *ATLAS liquid-argon calorimeter: Technical Design Report*. Technical Design Report ATLAS. Geneva: CERN, 1996. URL: https://cds.cern.ch/record/331061.

[89] ATLAS Collaboration. *ATLAS muon spectrometer: Technical Design Report*. Technical Design Report ATLAS. Geneva: CERN, 1997. URL: https://cds.cern.ch/record/331068.

[90] ATLAS Collaboration. "Performance of the ATLAS Trigger System in 2010." In: *Eur. Phys. J. C* 72 (2012), p. 1849. DOI: 10.1140/epjc/s10052-011-1849-1. arXiv: 1110.1530 [hep-ex].

[91] J G Panduro Vazquez. *The ATLAS Data Acquisition System: from Run 1 to Run 2*. Tech. rep. ATL-DAQ-PROC-2014-035. Geneva: CERN, Oct. 2014. URL: https://cds.cern.ch/record/1954156.

[92] ATLAS Collaboration. *Trigger Operation Public Results*. 2012. URL: https://twiki.cern.ch/twiki/bin/view/AtlasPublic/TriggerOperationPublicResults (visited on 26.08.2015).

[93] ATLAS Collaboration. *ATLAS Computing: technical design report*. Technical Design Report ATLAS. Geneva: CERN, 2005. URL: https://cds.cern.ch/record/837738.

[94] D Costanzo, I Hinchliffe, and S Menke. *Analysis Model Forum Report*. Tech. rep. ATL-GEN-INT-2008-001. ATL-COM-GEN-2008-001. Geneva: CERN, Jan. 2008. URL: https://cds.cern.ch/record/1081342.

[95] R. Brun and F. Rademakers. "ROOT: An object oriented data analysis framework." In: *Nucl. Instrum. Meth.* A389 (1997), pp. 81–86. DOI: 10.1016/S0168-9002(97)00048-X.

[96] P. Grafström and W. Kozanecki. "Luminosity determination at proton colliders." In: *Prog. Part. Nucl. Phys.* 81 (2015), pp. 97–148. DOI: 10.1016/j.ppnp.2014.11.002.

[97] S van der Meer. *Calibration of the effective beam height in the ISR*. Tech. rep. CERN-ISR-PO-68-31. ISR-PO-68-31. Geneva: CERN, 1968. URL: https://cds.cern.ch/record/296752.

[98] ATLAS Collaboration. "Improved luminosity determination in pp collisions at $\sqrt{s}$ = 7 TeV using the ATLAS detector at the LHC." In: *Eur. Phys. J. C* 73 (2013), p. 2518. DOI: 10.1140/epjc/s10052-013-2518-3. arXiv: 1302.4393 [hep-ex].

[99] I. Dolenc. "The ATLAS Beam Condition and Beam Loss Monitors." In: *Astroparticle, particle and space physics, detectors and medical physics applications. Proceedings, 11th International Conference on Advanced Technology and Particle Physics, ICATPP 11, Como, Italy, October 5-9, 2009*. 2009. DOI: 10.1142/9789814307529_0073.

[100] Mauro Villa. "The luminosity monitor of the ATLAS experiment." In: *Proceedings, 2009 IEEE Nuclear Science Symposium and Medical Imaging Conference (NSS/MIC 2009)*. 2009, pp. 1028–1033. DOI: 10.1109/NSSMIC.2009.5402438.

[101] ATLAS Collaboration. *LuminosityPublicResults*. 2012. URL: https://twiki.cern.ch/twiki/bin/view/AtlasPublic/LuminosityPublicResults (visited on 26.08.2015).

[102] W Lampl et al. "Calorimeter clustering algorithms, description and performance." In: *Report No. ATL-LARG-PUB-2008-002*, ATL-LARG-PUB-2008-002 (2010). URL: http://cdsweb.cern.ch/record/1099735.

[103] Matteo Cacciari, Gavin P. Salam, and Gregory Soyez. "The anti-k_t jet clustering algorithm." In: *J. High Energy Phys.* 04 (2008), p. 063. DOI: 10.1088/1126-6708/2008/04/063. arXiv: 0802.1189 [hep-ph].

[104] Matteo Cacciari, Gavin P. Salam, and Gregory Soyez. "The Catchment Area of Jets." In: *J. High Energy Phys.* 0804 (2008), p. 005. DOI: 10.1088/1126-6708/2008/04/005. arXiv: 0802.1188 [hep-ph].

[105] ATLAS Collaboration. "Characterisation and mitigation of beam-induced backgrounds observed in the ATLAS detector during the 2011 proton-proton run." In: *JINST* 8 (2013), P07004. DOI: 10.1088/1748-0221/8/07/P07004. arXiv: 1303.0223 [hep-ex].

[106] ATLAS Collaboration. "Jet energy measurement and its systematic uncertainty in proton-proton collisions at $\sqrt{s}$ = 7 TeV with the ATLAS detector." In: *Eur.Phys.J.* C75.1 (2015), p. 17. DOI: 10.1140/epjc/s10052-014-3190-y. arXiv: 1406.0076 [hep-ex].

[107] ATLAS Collaboration. *Pile-up subtraction and suppression for jets in ATLAS*. Tech. rep. http://cdsweb.cern.ch/record/1570994. Geneva: CERN, 2013.

[108] ATLAS Collaboration. *Jet global sequential corrections with the ATLAS detector in proton-proton collisions at $\sqrt{s}$ = 8 TeV*. Tech. rep. CERN, Mar. 2015. URL: https://cds.cern.ch/record/2001682.

[109] ATLAS Collaboration. *Tagging and suppression of pileup jets with the ATLAS detector*. Tech. rep. ATLAS-CONF-2014-018. Geneva: CERN, 2014. URL: http://cds.cern.ch/record/1700870.

[110] ATLAS Collaboration. "Jet energy measurement with the ATLAS detector in proton-proton collisions at $\sqrt{s} = 7$ TeV." In: *Eur. Phys. J.* C73.3 (2013), p. 2304. DOI: 10.1140/epjc/s10052-013-2304-2. arXiv: 1112.6426 [hep-ex].

[111] Georges Aad et al. "Electron reconstruction and identification efficiency measurements with the ATLAS detector using the 2011 LHC proton-proton collision data." In: *Eur. Phys. J.* C74.7 (2014), p. 2941. DOI: 10.1140/epjc/s10052-014-2941-0. arXiv: 1404.2240 [hep-ex].

[112] ATLAS Collaboration. *Data-driven determination of the energy scale and resolution of jets reconstructed in the ATLAS calorimeters using dijet and multijet events at* $\sqrt{s} = 8$ *TeV*. Tech. rep. ATLAS-CONF-2015-017. Geneva: CERN, Apr. 2015. URL: https://cds.cern.ch/record/2008678.

[113] ATLAS Collaboration. *Jet Etmiss Approved 2013 JES Uncertainty*. 2013. URL: https://twiki.cern.ch/twiki/bin/view/AtlasPublic/JetEtmissApproved2013JESUncertainty (visited on 21.07.2015).

[114] ATLAS Collaboration. "Search for new phenomena in the dijet mass distribution using $p - p$ collision data at $\sqrt{s} = 8$ TeV with the ATLAS detector." In: *Phys.Rev.* D91.5 (2015), p. 052007. DOI: 10.1103/PhysRevD.91.052007. arXiv: 1407.1376 [hep-ex].

[115] Bogdan A. Dobrescu and Felix Yu. "Coupling-mass mapping of dijet peak searches." In: *Phys. Rev. D* 88 (3 Aug. 2013), p. 035021. DOI: 10.1103/PhysRevD.88.035021.

[116] Victor Lendermann et al. "Combining Triggers in HEP data analysis." In: *Nucl. Instr. Meth. Phys. Res. A* 604.3 (2009), pp. 707–718. ISSN: 0168-9002. DOI: 10.1016/j.nima.2009.03.173. arXiv: 0901.4118 [hep-ph].

[117] M Baak et al. *Data Quality Status Flags and Good Run Lists for Physics Analysis in ATLAS*. Tech. rep. ATL-COM-GEN-2009-015. Geneva: CERN, Mar. 2009. URL: https://cds.cern.ch/record/1168026.

[118] Robert M. Harris and Konstantinos Kousouris. "Searches for Dijet Resonances at Hadron Colliders." In: *International Journal of Modern Physics* A26 (2011), pp. 5005–5055. DOI: 10.1142/S0217751X11054905. arXiv: 1110.5302 [hep-ex].

[119] Vardan Khachatryan et al. "Search for resonances and quantum black holes using dijet mass spectra in proton-proton collisions at $\sqrt{s} = 8$ TeV." In: *Phys. Rev.* D91.5 (2015), p. 052009. DOI: 10.1103/PhysRevD.91.052009. arXiv: 1501.04198 [hep-ex].

[120] ATLAS Collaboration. *Search for New Phenomena in the Dijet Mass Distribution updated using 13.0* fb^{-1} *of* pp *Collisions at* $\sqrt{s} = 8$ *TeV collected by the ATLAS Detector*. Tech. rep. Geneva: CERN, 2012. URL: http://cds.cern.ch/record/1493487.

[121] Karl Pearson F.R.S. "X. On the criterion that a given system of deviations from the probable in the case of a correlated system of variables is such that it can be reasonably supposed to have arisen from random sampling." In: *Philosophical Magazine Series 5* 50.302 (1900), 157–175. DOI: 10.1080/14786440009463897.

[122] Georgios Choudalakis. "On hypothesis testing, trials factor, hypertests and the BumpHunter." In: (2011). arXiv: 1101.0390 [physics.data-an].

[123] E. Gross and O. Vitells. "Trial factors for the look elsewhere effect in high energy physics." In: *Eur. Phys. J.* C70 (2010), p. 525. DOI: 10.1140/epjc/s10052-010-1470-8. arXiv: 1005.1891 [physics.data-an].

[124] G. Choudalakis and D. Casadei. "Plotting the differences between data and expectation." In: *European Physical Journal Plus* 127, 25 (Feb. 2012), p. 25. DOI: 10.1140/epjp/i2012-12025-y. arXiv: 1111.2062 [physics.data-an].

[125] Mr. Bayes and Mr. Price. "An Essay towards Solving a Problem in the Doctrine of Chances. By the Late Rev. Mr. Bayes, F. R. S. Communicated by Mr. Price, in a Letter to John Canton, A. M. F. R. S." In: *Philosophical Transactions* 53 (1763), pp. 370–418. DOI: 10.1098/rstl.1763.0053.

[126] Allen Caldwell, Daniel Kollár, and Kevin Kröninger. "BAT – The Bayesian analysis toolkit." In: *Computer Physics Communications* 180.11 (2009), pp. 2197–2209. ISSN: 0010-4655. DOI: 10.1016/j.cpc.2009.06.026.

[127] J Wenninger. "Energy Calibration of the LHC Beams at 4 TeV." In: *Report No. CERN-ATS-2013-040*, (2013). http://cdsweb.cern.ch/record/1546734.

[128] Michiel Botje et al. "The PDF4LHC Working Group Interim Recommendations." In: (2011). arXiv: 1101.0538 [hep-ph].

[129] Gupta A. and Kotwal A. "Comparisons of HERWIG and PYTHIA as Inclusive W Generators." In: *Report No.Do-3195* (1997). URL: http://inspirehep.net/record/1198869/.

[130] J. Alitti et al. "A Search for new intermediate vector mesons and excited quarks decaying to two jets at the CERN $\bar{p}p$ collider." In: *Nucl. Phys.* B400 (1993), pp. 3–24. DOI: 10.1016/0550-3213(93)90395-6.

[131] F. Abe et al. "Search for new particles decaying to dijets at CDF." In: *Phys. Rev.* D55 (1997), pp. 5263–5268. DOI: 10.1103/PhysRevD.55.R5263. arXiv: hep-ex/9702004 [hep-ex].

[132] T. Aaltonen et al. "Search for new particles decaying into dijets in proton-antiproton collisions at $\sqrt{s} = 1.96$ TeV." In: *Phys. Rev. D* 79 (2009), p. 112002. DOI: 10.1103/PhysRevD.79.112002. arXiv: 0812.4036 [hep-ex].

[133] Serguei Chatrchyan et al. "Search for narrow resonances and quantum black holes in inclusive and b-tagged dijet mass spectra from pp collisions at $\sqrt{s} = 7$ TeV." In: *JHEP* 01 (2013), p. 013. DOI: 10.1007/JHEP01(2013)013. arXiv: 1210.2387 [hep-ex].

[134] ATLAS Collaboration. "ATLAS search for new phenomena in dijet mass and angular distributions using pp collisions at $\sqrt{s} = 7$ TeV." In: *J. High Energy Phys.* 2013.01 (2013), p. 029. DOI: 10.1007/JHEP01(2013)029. arXiv: 1210.1718 [hep-ex].

[135] CMS Collaboration. *Search for Narrow Resonances using the Dijet Mass Spectrum with 19.6 fb^{-1} of pp Collisions at $\sqrt{s} = 8$ TeV*. Tech. rep. CMS-PAS-EXO-12-059. Geneva: CERN, 2013. URL: http://cds.cern.ch/record/1519066.

[136] G. Arnison et al. "Measurement of the Inclusive Jet Cross-Section at the CERN p anti-p Collider." In: *Phys. Lett.* B172 (1986), p. 461. DOI: 10.1016/0370-2693(86)90290-X.

[137] W.J Stirling. private communication. 6 Oct. 2015.

[138] CMS Collaboration. *Search for Narrow Resonances using the Dijet Mass Spectrum with 40pb^{-1} of pp Collisions at $\sqrt{s} = 13$ TeV*. Tech. rep. CMS-PAS-EXO-15-001. Geneva: CERN, 2015. URL: https://cds.cern.ch/record/2048099.

[139] ATLAS Collaboration. *Search for New Phenomena in Dijet Mass and Angular Distributions with the ATLAS Detector at $\sqrt{s} = 13$ TeV*. Tech. rep. ATLAS-CONF-2015-042. Geneva: CERN, Aug. 2015. URL: http://cds.cern.ch/record/2048113.

LIST OF FIGURES

LIST OF TABLES

ACKNOWLEDGEMENTS

Aus Datenschutzgründen sind personenbezogene Daten aus der elektronischen Version gelöscht.